EXPERIMENTAL INVESTIGATION OF NEUROSURGICAL ROTARY ULTRASONIC BONE GRINDING

A Thesis submitted in fulfillment of the requirement for the award of the degree of

DOCTOR OF PHILOSOPHY

IN

MECHANICAL ENGINEERING

Submitted by

ATUL BABBAR

Roll No. 901708009

Under the supervision of

Dr. Vivek Jain
Associate Professor

Dr. Dheeraj Gupta
Associate Professor

Department of Mechanical Engineering,
Thapar Institute of Engineering & Technology, Patiala-147004, INDIA
(Deemed to be University)

January 2021

CONTENTS

CERTIFICATE

I, **Atul Babbar**, Roll no. 901708009, hereby declared that the thesis entitled **"Experimental Investigation of Neurosurgical Rotary Ultrasonic Bone Grinding"** submitted to the Department of Mechanical Engineering at Thapar Institute of Engineering & Technology, Patiala, Punjab (India) is an authenticated record of my own work for the award of the degree "Doctor of Philosophy" under the supervision of Dr. Vivek Jain and Dr. Dheeraj Gupta. This report has not been submitted to any other institute for the award of any other degree.

12/01/21

Atul Babbar

Roll no. 901708009

Patiala

Date: 12/01/21

This is certifying that the above statement by the candidate is correct to the best of our knowledge

Verified by:

12/01/21

Dr. Vivek Jain
(Supervisor)
Associate Professor
Department of Mechanical Engineering
Thapar Institute of Engineering & Technology
Patiala-147004, (Punjab), India

12/01/2021

Dr. Dheeraj Gupta
(Supervisor)
Associate Professor
Department of Mechanical Engineering
Thapar Institute of Engineering & Technology
Patiala-147004, (Punjab), India

ETHICAL CLEARANCE CERTIFICATE

INSTITUTIONAL ETHICS COMMITTEE (IEC)
Department of Biotechnology

THAPAR INSTITUTE
OF ENGINEERING & TECHNOLOGY
(Deemed-to-be-University u/s 3 of the UGC Act, 1956)
Thapar Technology Campus,
Bhadson Road, Patiala - 147 004 (Punjab) India
Phone : +91-175-2393021
Email : registrar@thapar.edu
URL : www.thapar.edu

Review Letter number IEC/TIET/DBT/09/02/18
Dated: 27.09.2018

The Institutional ethics committee of Thapar Institute of Engineering & Technology, Patiala, in its Sixth (06) meeting held on 27.09.2018, in the office of Head, Department of Biotechnology, reviewed and discussed the project submitted by Dr. Vivek Jain and Dr. Dheeraj Gupta as PI's from Department of Mechanical Engineering .

TIET/DBT/IEC/09/02/18: Design and Development of a novel neurosurgical bone grinding process to minimize thermal necrosis

The members reviewed the following documents and raised queries which were satisfactorily answered by Dr. Jain and Dr. Gupta

a) Proposal & Protocol

b) Available Safety Information

c) Cell line/ Genetic material storage and discard procedure

It is understood that the study would be conducted under the PI's direction strictly as per the submitted protocol. In case of any deviation from the approved methods, the study documents will have to be resubmitted to ethics committee for re-approval.

Members	**Signature**
Dr. Manoj Baranwal (Member)	
Dr. Siddharth Sharma (Member)	
Dr. Vikas Handa (Member)	
Dr. Sanjai Saxena (Member Secretary)	

The present approval is for 01 year only; the investigators are advised to take a re-approval after one year. 06 Monthly compliance report is a must for seeking re-approval.

Signature
Prof. Moushumi Ghosh
Chairman, Institutional Ethics Committee

ACKNOWLEDGEMENT

First and the foremost, I wish to thank my supervisors **Dr. Vivek Jain** and **Dr. Dheeraj Gupta** for his valuable support and guidance. I am sincerely gratitude to him for judging my potential and providing me an interesting topic according to my capability. I am thankful for his positive suggestions, and meticulous guidance that helped me to improve my talent to write scientific research papers and carries out the new research. His patience and motivation enhanced me up to achieve in my goal. I feel really honored to have worked under his mentorship throughout my entire Ph.D. work.

I thank the doctoral committee members **Dr. T.P. Singh** (Chairman, Board of Studies), **Dr. Mandeep Singh**, **Dr. Anant Kumar Singh** and **Dr. Ratnesh Kumar** for the feedback and reviews that were given on my research proposal and progress monitoring presentations. Their guidance was beneficial for me to improve my research work. I am also thankful to **Dr. Tarun Nanda**, our Ph.D. coordinator for his approachability and keeping me informed with all the relevant communication throughout E-mails.

I would like to express my special thanks of gratitude to **Dr Deepak Agrawal** and his team at **All India Institute of Medical Science (AIIMS), New Delhi** for their timely guidance and abetting me facilities by providing details of neurosurgical bone grinding operation and special visits to Out-Patient Department (OPD) to carefully examine the whole bone grinding operation.

From the core of my heart, I dedicated my thesis to my beloved parents **Mr. Ajay Babbar** (Father) and **Mrs. Seema Babbar** (Mother) and complete family members for their constant encouragement, love and blessing.

I thank to "**Almighty God and Guru**" for giving me the strength and patience for successfully completing my goal.

Atul babbar

ABSTRACT

Neurosurgical bone grinding is a procedure in which a part of the bone is removed using mechanical grinding process and then the passage is created to reach the tumor's locations within the brain and spine; thus, treating abnormal accumulation of the mass causing cancer. A miniature grinding burr is inserted in the nostril along with the endoscope to remove the skull bone with abrasion action. Now, when grinding burr comes in contact with the surface of bone then the bone is removed in the form of microchips and leads to the increment in the temperature at the grinding site. This rise in temperature has adverse effects on soft and hard tissues since a lot of critical nerve branches surrounds the skull bone. These nerve branches include temporal branch, zygomatic branch, cervical branch, facial nerves, posterior auricular branch, greater petrosal nerves etc. These nerves are responsible for the important functioning of human body organs. Blood coagulation, optic nerve damage, thermogenesis and osteonecrosis are other associated concerns of temperature rise. Therefore, it becomes vital to limit the temperature to safe levels to avoid any king of thermal trauma during osteotomy. Hence, the research endeavor of the present work is paying attention and introduces some strategies to minimize the temperature produced during the bone grinding.

In present research work, a new strategy of using rotary ultrasonic bone grinding has been introduced and further explored for different response characteristics. A spherical diamond burr has been used for the experimentation and porcine bone is used as the workpiece material. Different input parameters rotational speed, feed rate, and frequency has been investigated at three states in terms of change in temperature and thermal biological damage. The systematic investigation has been carried out to determine the effect of varying process parameters on the osteonecrosis at the cut surface. During the investigation, it has been observed that selected process parameters has significant effects on the temperature rise during bone grinding. It has been revealed that temperature increases as the rotational speed, feed rate, and ultrasonic frequency is increased. Statistical analysis revealed that feed rate (45.43%) has the highest contribution towards temperature rise during grinding followed by ultrasonic frequency (23.87%), and rotational speed (12.85%). For comparative analysis, conventional bone grinding experiments have also been carried out at the parametric sets causing maximum and minimum temperature during bone grinding. Furthermore, viable lacunas (filled osteocytes), non-viable lacunas (empty lacunas), necrosed tissues, and haversian canal was found during histological examination. The histograms revealed that rotary ultrasonic bone grinding possessed greater viability of cells and reduced temperature

compared with conventional bone grinding. Optimized set of machining parameters to avoid osteonecrosis and thermal trauma found to be rotational speed = 35,000 rpm, feed rate = 20 mm/min, and ultrasonic frequency = 20 kHz.

Since the neurosurgeons uses conventional bone grinding, therefore, the cutting forces developed during the CBG for different sets of parametric combinations have been measured. It has been observed that the increased forces caused crack initiation and propagation on the surface of bone which affects the bone's regeneration ability and post-operatively healing time.

Later, different shapes of the grinding burrs have also been investigated based upon the consultation with neurosurgeons. Since the saline irrigation is continuously used during the bone grinding therefore, burr loading and burr wear is a concern for the neurosurgeons. It is expected that burr loading and burr wear affects the cutting ability of the abrasives and friction at burr-bone interface which eventually affects the temperature produced during bone grinding. To address this concern, quantification analysis has been made for different shape of the grinding burrs. It is revealed that convex shape burr caused minimum burr loading and wear during bone grinding.

The important concern of the neurosurgeons for determining the thermal tissue injury and depth of thermogenesis and osteonecrosis has been addressed by using the hybrid thermal dose model and simulation. The maximum depth of thermogenesis (4.26 mm, beneath the grinding slot) and osteonecrosis (1.28 mm) found for rotational speed of 55000 rpm, feed rate of 60 mm/min, and ultrasonic frequency of 40 kHz. Subsequently, the optimum parameters for bone grinding have been suggested using hybrid thermal dose model which will result in no thermal tissue injury considering the exposure temperature and exposure time simultaneously for bone grinding.

LIST OF FIGURES

LIST OF TABLES

LIST OF ABBREVIATIONS/ACRONYMS/SYMBOLS

CBG	Conventional Bone Grinding
CD	Conventional Drilling
EDS	Energy Dispersive Spectroscopy
RUNG	Rotary Ultrasonic Neurosurgical Grinding
SEM	Surface Electron Microscopy
UAD	Ultrasonic Assisted Drilling
USM	Ultrasonic Machining
E_a	Arrhenius activation energy (J/mol)
T	Actual exposure temperature (℃)
T_{break}	breaking point temperature (℃)
CEM 43℃	Cumulative number of equivalent minutes at 43 ℃
ΔT	Change in temperature (℃)
A	Pre-exponential factor (s^{-1}) or Arrhenius constant
K	Rate constant
σ	Standard deviation
Ω	Tissue damage function
τ	Time (seconds)
R	Universal gas constant (J/mol/k)

CHAPTER 1: INTRODUCTION

1.1 HUMAN BONE

Bone is a lightweight and hard-connecting tissue consists of honeycomb-like structure which provides enough rigidity and flexibility for movement of the different body parts. The main function of the bone is to protect other vital organs responsible for a living. Besides, it produces red blood cells (RBCs) and white blood cells (WBCs) and stores important minerals required for the functioning of the body. The medullar cavity of the bone is occupied by the red/yellow marrow whose primary function is to generate blood cells. From birth to early adolescence, the colour of the marrow is red and as we grow old the colour changes to yellow. Red marrow contains hematopoietic stem cells which further developed into RBCs, WBCs, and platelets while yellow marrow contains fat cells. Some other tissues like endosteum, periosteum, vessels, cartilage, and nerves are also found in the bone. Bone is anisotropic and heterogenetic and consists of cortical (compact or lamellar) and cancellous part at the macroscale [1]. The cortical tissues of the bone refer to the utmost hard and dense part composed of osteons and interstitial organs [2]. The cortical part of the bone accounts for almost 80 wt% of the human body which provides vital rigidity and strength against impact loads and bending moments [3]. However, remaining 20 wt% accounts for trabecular bone which is also known as cancellous bone [4]. The cortical part stores and release vital vitamins and minerals and provides the white solid appearance to the bone [5]. Furthermore, cortical bone consists of numerous osteons and each osteon has layers of osteocytes and osteoblasts surrounding the Haversian canal. The outer layer of cortical bone wrapped with the periosteum and inner with endosteum and it acts as a separation between cortical and cancellous bone. The cancellous part refers to a rod-like tissues, lightweight porous bone structure and is positioned within the boundary of cortical bone which is

prolonged in a three-dimensional plane. Cancellous bone is a porous structure whose S/V (surface to volume) ratio is higher than cortical bone due to its less density. It is very light and highly flexible due to the network of the rod and plate-like elements. The highly vascular nature of cancellous bone makes it fit for the haematopoiesis (production of RBCs, WBCs, and platelets).

At the microscopic level, compact bone consists of osteons. Further, each osteon has a cylindrical structure which consists of Haversian canal, lamellae, lacunae, and canaliculi. Haversian canal is a central tube which includes nerves and blood vessels. Lamellae ("little plates") are strong matrix concentric rings formed from mineral salts such as calcium, phosphate, and collagen fibres. The hardness to the bone's structure is imparted by minerals whereas collagen fibres provide strength to the bone. The small spaces between the lamellae in which bone cells (also called as "osteocytes") are present, known as Lacunae. Further, these lacunae are connected by minute channels known as canaliculi which are primarily responsible for the transport of nutrient to and waste products away from the osteocytes. The structure of the compact and cancellous bone is depicted in Figure 1.1. The important constituents of the bone's formation have been discussed as follows.

Osteoblasts: Osteoblasts are single nucleate cells which contribute in the formation of the bone. Its primary function is to manufacture hormones and formation of osteoid (i.e., protein mixture) which then gets hardened thereby, leading to formation of the bones. These cells are found near the surface of the bone.

Osteoclasts: These are multinucleated large cells which leads to the bone resorption. These are found on the surface of the bone and are also known as "destructor" of bones. These are

responsible for dissolving the collagens with acids thereby, demineralize the surrounding bone. The osteoclasts and osteoblasts both are key parts responsible for the remodelling of the bone.

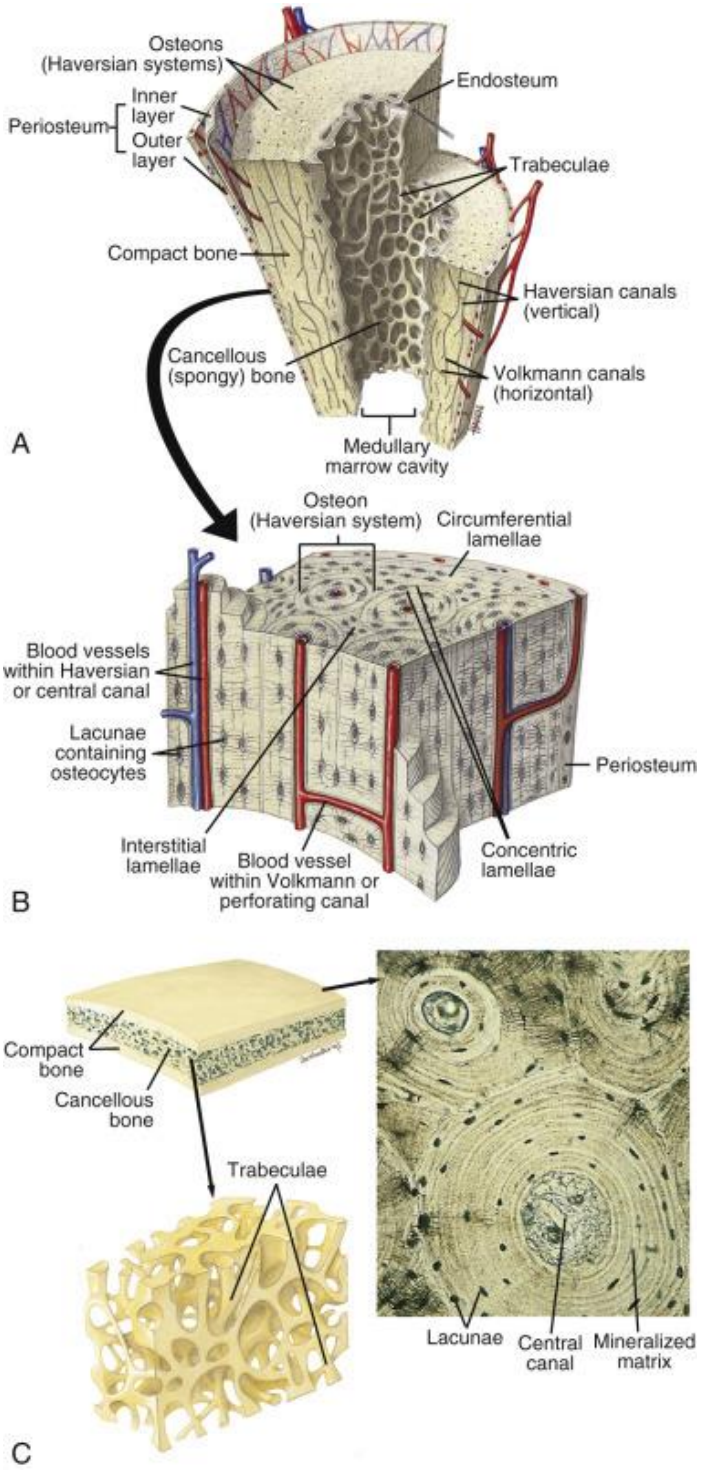

Figure 1.1: Structure of compact and trabecular bone: A- Bone section illustrating compact and cancellous part of the bone; B- Compact bone (magnified view); C- Flat bone section [6].

Bone lining cells (BLCs): These are multinucleate flattened cells that line bone. BLCs have a common lineage with cells responsible for the bone's formation i.e. osteogenic cells. These cells also work as the barrier for certain types of ions.

Osteocytes: These are mature osteoblasts which encased within the bone matrix (or calcified matrix) which they produce. On the completion of the bone's formation, some of the mature osteoblasts transformed into the osteocytes (trapped in a calcified matrix and becomes quiescent), lining (gets flatten) cells, and apoptotic (cellular suicide) osteoblasts. Most of the osteoblasts die owing to the cellular apoptosis. The osteocytes reside within the body of the lacuna and are connected to the adjacent osteocytes and Haversian canals thorough canaliculi. Furthermore, the lacunar–canalicular network of osteocytes in terms of the concentric arrangements around the Haversian canal termed as osteons. The presence of the mineral phase confers stiffness, the collagen provides toughness, strength comes from the combination of the mineral and collagen phases. The thermo-mechanical properties of the human bone have been shown in Table 1.1

Table 1.1: Properties of the human bone [7–15].

Property	**Unit**	**Human Bone**
Young's modulus	GPa	18.6 ± 3.5
Ultimate stress	MPa	132 ± 12.8
Tensile strength	MPa	124 ± 1.1
Compressive strength	MPa	170 ± 4.3
Thermal conductivity	W/mK	0.68 ± 0.01
Density	kg/m^3	1800-2000
Poisson's ratio	–	0.4
Emissivity	–	0.96 ± 0.01

Specific heat	J/KgK	1140 – 2370

1.2 BONE GRIDING: PROCESS, COMPLICATIONS, AND CONSEQUENCES

Brain cancer primarily occurs due to abnormal cell proliferation and accumulation of mass which results in the bone's formation. Bone grinding is a procedure in which a part of the bone is removed and then the passage is created to reach the tumor's locations within the brain and spine [16]. In this way, abnormal accumulation of the mass causing cancer is treated. During surgery, the patient is given general anaesthesia and scalp is anaesthetized by injecting a local anaesthetic along the course of lesser and greater occipital, supraorbital and auricular nerves. The computer navigation and stereotaxis are utilized to pinpoint the size of the bony structure. Subsequently, its precise location is identified then craniotomy is performed and the bone flap took out. Other applications of bone grinding include ossification of posterior longitudinal ligament (OPLL) surgery, trigeminal neuralgia surgery, bone decompression surgery, craniomaxillofacial surgery, and expanded endonasal approach (EEA) [17,18]. Nowadays, tumor present at the bottom part of the skull bone and near the nostril are treated with expanded endonasal approach (EEA) [19]. The invention of the EEA approach has completely revolutionized the treatment of benign and cancerous tumors which were earlier impossible to treat without the removal of a major part of the bone. A miniature grinding burr is inserted in the nostril along with the endoscope to remove the skull bone via abrasion action [20]. Furthermore, an endoscope is equipped with a lens and light which assist the neurosurgeons to perform minimally invasive surgery. The light provides the necessary illumination at the grinding site whereas lens projects the magnified view of the grinding site over the computer monitor. Owing to the abrasion during bone grinding, cutting

forces and heat comes into the picture and plays a significant role in whole grinding operation. These effects cause increase in the cutting forces, temperature rise, microcracks, and quality of bone around the grinding site. So, the quantification of the cutting forces and temperature becomes necessary to perform bone grinding efficiently with minimal disturbance to the surrounding tissues and bone. The rise in temperature during bone grinding has adverse effects on soft and hard tissues since a lot of critical nerve branches surrounds the skull bone. These nerve branches include temporal branch, zygomatic branch, cervical branch, facial nerves, posterior auricular branch, greater petrosal nerves etc [21–25]. These nerves are responsible for the important functioning of human body organs. Blood coagulation, visual impairment, optic nerve damage, loss of facial muscle control, thermogenesis and osteonecrosis are other associated concerns of temperature rise [9,26–28]. Therefore, it becomes vital to limit the temperature to safe levels to avoid any kind of thermal trauma during osteotomy.

The neurosurgeons generally use a diamond-impregnated abrasive burr instead of a drill bit during bone grinding [29]. The key benefit of using burr is that it enables the surgeons to feel some resistive force amid grinding hard tissues (bone). Besides, diamond burr assists in meticulousness control and minimum thermal trauma during osteotomy. The diamond is a very hard stiff and strong version of carbon and a very little is released during grinding in terms of abrasive wear. However, graphite is also pure carbon but the bonds between the layers are very weak and it can be used as a dry lubricant. Graphite on a drill would be a total disaster (unless dry lubrication is needed). The in-vivo bone grinding operation has been shown in Figure 1.2.

Figure 1.2(a), (b), and (c) exemplifies the computed tomography (CT) and magnetic resonance images (MRI) of a brain tumor. A high-speed neurosurgical bone grinding machine has been shown in Figure 1.2(d) and (e), whereas Figure 1.2(f) shows the spherical diamond-impregnated

abrasive burr (4 mm diameter). Currently, a normal saline flood irrigation is used in the surgical theatre during bone grinding whose effectiveness is mitigated by the combined role of curbed space and high-speed burr [30].

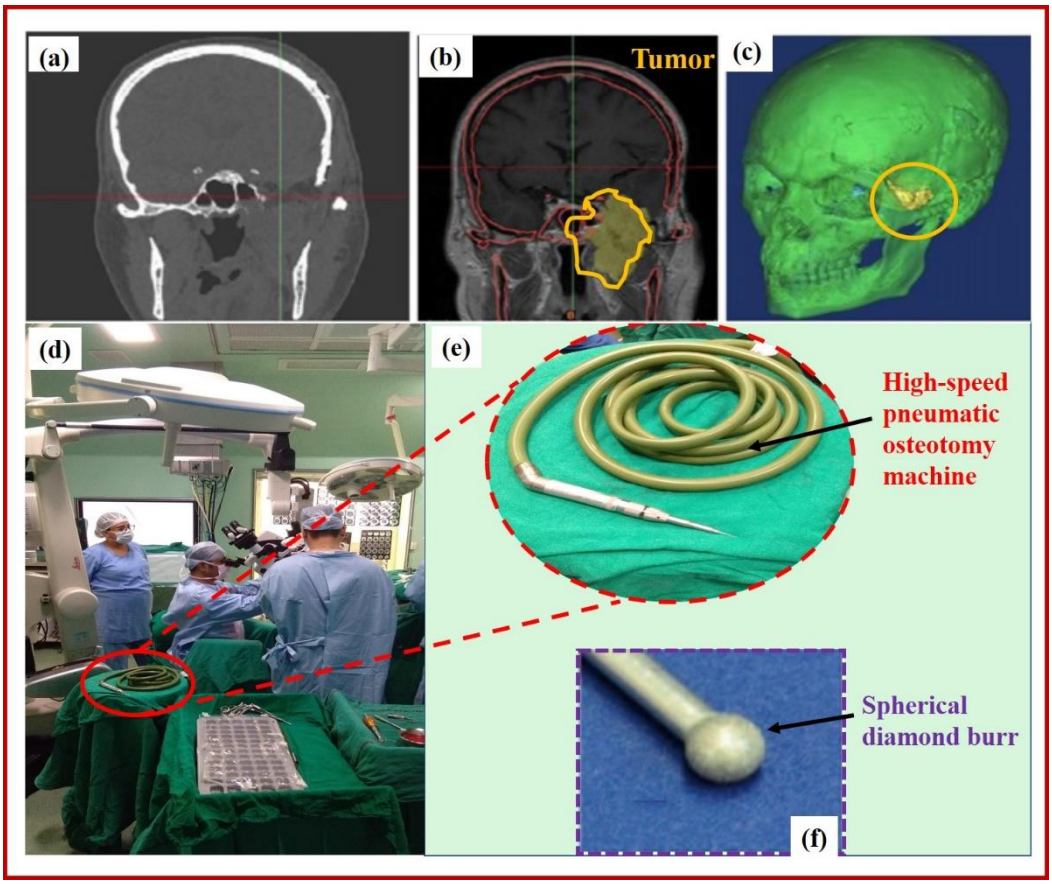

Figure 1.2: In-vivo bone grinding operation: (a) CT image [31]; (b) MRI image [31]; (yellow and red color indicates tumor and bone structure); (c) 3D skull model [31]; (d) OPD (AIIMS, New Delhi); (e) High-speed pneumatic grinding machine; (f) Diamond-impregnated abrasive burr [7].

The removal of bone chips from the surface of bone leads to the extensive generation of the heat at the grinding site, thus causing significant temperature rise which sometimes even exceeds the threshold level of thermal necrosis. Osteonecrosis or thermal necrosis is the primary concern for

the neurosurgeons working in this field. The thermal conductivity of the bone is very less due to which heat is not transferred to the surrounding medium and leads to local heating at the grinding site. This local heating further leads to the first, second and third-degree of burns. However, the temperature of 47℃ for 1 min causes irreversible damage to the bone (bone death) and is termed as thermal necrosis or osteonecrosis. It has been observed that specific cutting energy in case of grinding operation is higher than the other machining methods. The cutting energy is converted into the heat which further culminates the temperature escalation. The consumed energy is rapidly transferred directly into the workpiece through conduction mode of heat transfer and leads to a rise in temperature at the grinding site.

1.3. TEMPERATURE MEASUREMENT TECHNIQUES

The measurement of temperature during osteotomy is crucial to determine the possibility of thermal necrosis. Thermocouple and infrared (IR) thermography are the two techniques which have been implemented during bone machining. Kelly et al. [32] inserted thermocouples inside the optic nerve canal to measure the temperature around the bone drilling region during a machining time of 30 seconds. The results revealed a significant reduction of 3.3 ºC in the mean temperature using a diamond burr with continuous irrigation. Augustin et al. [33] reported a study in which the infrared thermography camera was used to determine the spatial distribution of the temperature during drilling of the porcine femoral bone. Some another researcher utilized thermocouples to measure the temperature during bone drilling [34]. Thermocouples were embedded at 1.0, 1.5, and 2 mm from the drilling site and the inability of the thermocouples to produce precise results were highlighted. Recently, Tai et al. [35] used thermocouples and predicted the temperature with inverse heat transfer method during skull base neurosurgery with

a spherical diamond burr. The actual representation of the thermocouples for the measurement of temperature during in-vitro bone grinding has been depicted in Figure 1.3.

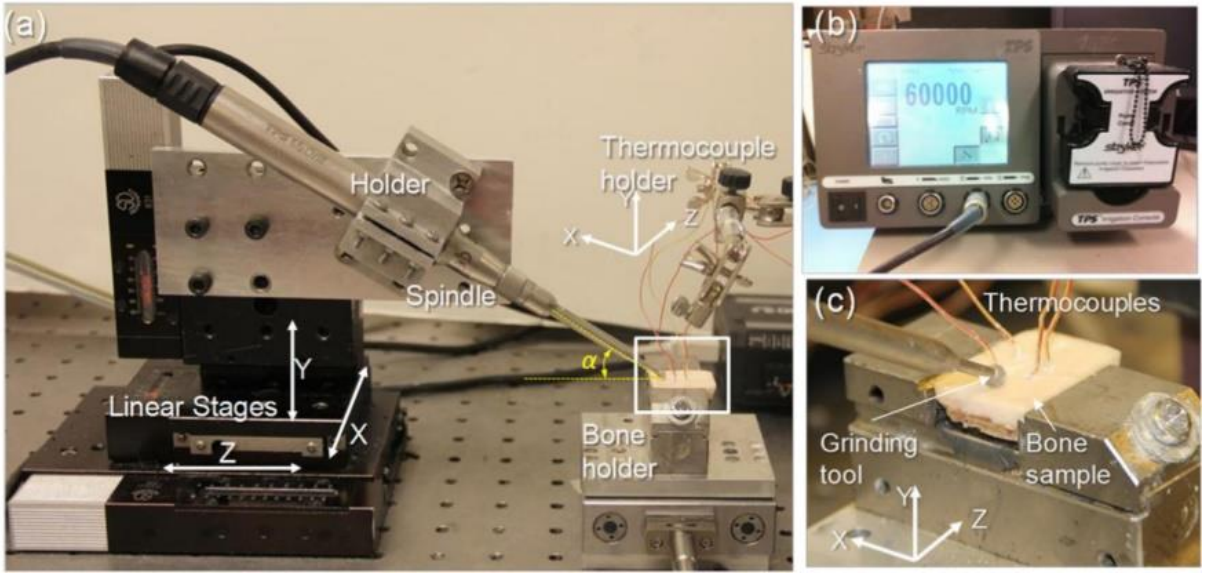

Figure 1.3: Measurement of temperature using thermocouples: (a) Experimental setup; (b) Datalogger; (c) Magnified view of the grinding site [16].

However, in actual surgical operations, the use of thermocouples is not feasible because pilot holes are required to drill in the bone to insert thermocouple in it. Moreover, thermocouples do not provide precise results as they are placed at a certain distance from the drilling/grinding zone. This limitation can be surpassed by using infrared (IR) thermography technique owing to its non-contact type nature. Additionally, the thermograms produced by IR technique provide precise temperature measurement as well as the distribution of temperature around the machining zone. Augustin et al. [33] reported a study in which an infrared thermography camera was used to estimate temperature distribution (spatial) of porcine femoral bone drilling. In a comparative study, Sasaki et al. [36] used thermograms to investigate the temperature during bone drilling with different cooling mechanisms. It was outlined that infrared thermography technique has the

potential to give precise temperature readings during osteotomy. The thermograms produced during bone grinding using IR thermography has been depicted in Figure 1.4.

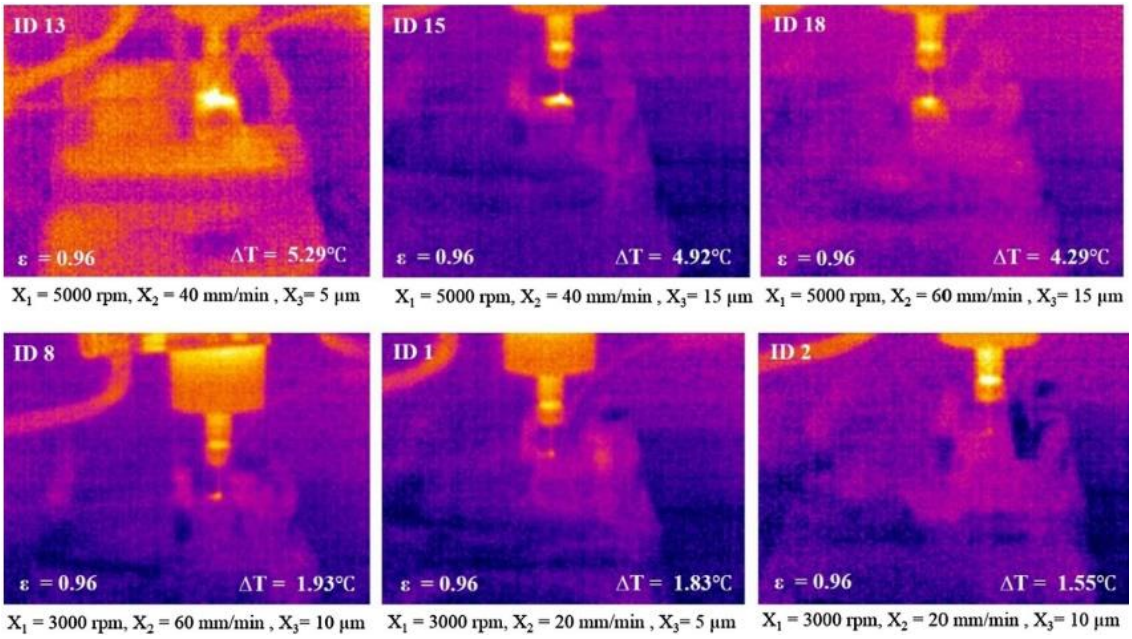

Figure 1.4: Infrared thermograms produced during bone grinding [37].

1.4 ROTARY ULTRASONIC BONE GRINDING

1.4.1 Ultrasonic Machining

Ultrasonic machining (USM) is an example of subtractive manufacturing in which a tool is actuated with appropriate frequency and amplitude to remove the material from the workpiece. Ultrasound refers to elastic wave having a frequency greater than 20 kHz [38]. The schematic representation of the ultrasonic machining is shown in Figure 1.5. The material is removed from the surface with three mechanisms namely hammering, impact and cavitation. Hammering cause mechanical abrasion in which abrasive grit get struck in between vibrating tool and workpiece, hence indent both tool and work surface. If the space between tool and work is greater than grit size then abrasive grit will fly and hit the workpiece during a collision with the tool. When abrasive slurry flows over the workpiece surface then it leads to cavitation. The process of

material removal starts with the movement of the tool from the uppermost rest position. As the tool moves downwards, its speed starts increasing and reaches a maximum at the mean position while its speed gets zero at the lowermost position [39].

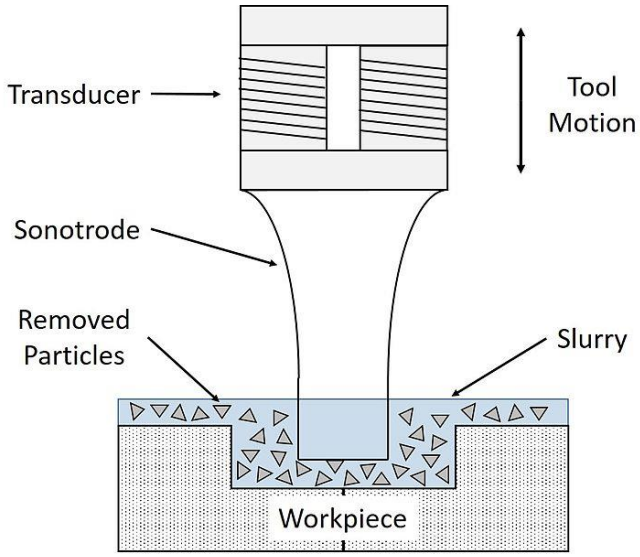

Figure 1.5: Schematic of ultrasonic machining process [40]

During the downward journey of the tool, it strikes the abrasive grit with higher impact near the mean position. Due to this high impact, some of the grits may fracture and more grits can come in contact with the tool during downward motion. The number of grits is maximum under the impact of the tool when the tool reaches the end of the strike. The penetration of the grit depends upon the diameter and hardness of the grit. The magnitude of momentum transfer during collision entirely depends upon the size of the grit. An abrasive slurry continuously circulates in-between tool and workpiece to ensure proper cooling and removal of swarf particles. The common type of abrasives used in USM is aluminium oxide, boron carbide, diamond, and silicon carbide [41]. The liquid preferred for slurry should have high thermal conductivity, non-corrosive and low viscosity. The thermal losses in acoustic design of the transducer can be

reduced and results can be optimized using numerical analysis and augmenting constraint method [42,43].

A. Applications

- Machining of 3D contours, ceramics and cutting parts from semiconductors.
- Ultrasonic sinking, drilling, and micro-machining.
- Production of electrodes for electric discharge machining.
- Engraving on the glass and other brittle materials.

B. Limitations

- Low material removal rate.
- Low penetration rate
- Shorter tool life
- For small holes, the abrasive slurry may erode the surface of the machined wall.
- Tool wear is another concern which stops machining with precise dimensions.

1.4.2 Rotary Ultrasonic Machining

Rotary Ultrasonic Machining (RUM) is a hybrid non-conventional machining process in which abrasives impregnated tool is rotated as well as actuated with a certain frequency to achieve the desired material removal rate. So, RUM uses material removal mechanism of both conventional grinding and ultrasonic machining. The advantages of RUM included high material removal rate, less heat generation, less thrust force, and torque compared to conventional methods. In RUM, all the abrasive particles participate in the ground due to which more material is removed with precise dimensional tolerances. A tool is actuated with frequency and is given a certain feed rate so that the tool moves towards the workpiece during machining. Machining zone is flooded with coolant to remove debris particles to protect tool and workpiece from erosion. The basic

elements of the RUM process are shown in Figure 1.6. Firstly, high power is supplied to the ultrasonic transducer then electrical energy is converted into mechanical actuation. The piezoelectric type transducer is preferred since it produces low noise with minimum loss of energy.

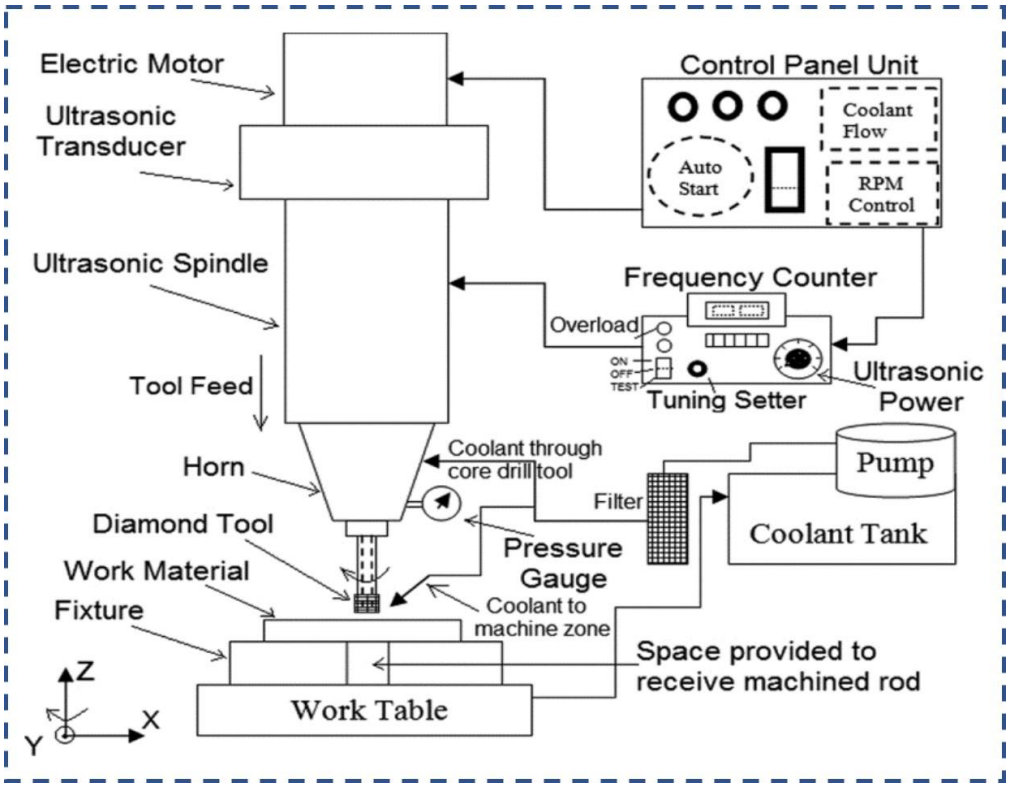

Figure 1.6: Basic elements of rotary ultrasonic machining [44]

The longitudinal vibrations get a boost while travelling in the horn and reach to the tool. Coolant is continuously fed in the machining zone from the coolant tank. A high-power pump circulates the coolant from the tank to the machining area. The rotational speed of the cutting tool can be changed by varying the speed of the electric motor from the control panel unit. The data acquisition system plays an important role in gathering the information about force, torque and other parameters. For the measurement of force and torque, a dynamometer is often used and plots are obtained from the software installed in the computer system attached to it.

Rotary ultrasonic machining (RUM) is gaining higher attention from the researchers worldwide due to the less heat generation and high surface quality involved in such a process. In one of the studies [45], it was reported that ultrasonic drilling provides better control over the process and cause less damage to the underlying dura mater. On another side, conventionally rotating tool can sternly harm the soft tissues. Moreover, unlike conventional processes rotary ultrasonic-assisted machining does not generate bone chips which reduce the chances of infection. Due to the combined material removal action of vibrational and conventional drilling, more material removal is observed in RUM than conventional process [46]. Furthermore, rotary ultrasonic-assisted grinding plays a key role in the desire to reduce the temperature generated during bone machining. It also leads to increase in the quality of processed bone coupled with environment-friendly characteristics.

1.5 MOTIVATION TOWARDS THE RESEARCH

Neurosurgery is performed for diseases in the brain, spinal cord, peripheral nervous system and their allied organs such as blood vessels, bone, and muscle [47]. Surgical operations in the field of neurosurgery embrace emergency operations achieved for stroke and head injury and the resection of life-threatening brain tumors. Also, included are those envisioned for the prevention of recurrence of stroke performed in the chronic phase as well as functional surgery that does not directly affect vital prognosis such as operations for facial spasms [48]. The need for treatment and the method of treatment differ among individual patients, even for those having the same diagnosis.

The rise in cutting forces and temperature during bone grinding is a major concern for the neurosurgeons worldwide. The heat generated during bone grinding could cause loss of vision, optic nerve damage, loss of facial muscles control, thermal necrosis, and blood coagulation

which is a major reason of the stroke in carotid artery [49]. So, mitigating temperature rise during grinding is important to avoid thermal damage to the bone.

Different clinical studies were carried out to evaluate the effect of the rise in heat during osteotomy on hard and soft tissues. Vrind et al. [50] investigated the thermal effect on rat sciatic nerve during bone osteotomy. The results revealed that an increase in temperature beyond threshold caused complete sensory and functional loss with a decrease in the amplitude of motor and reflex responses. On the same context, Xu and Pollock [51] studied thermal injury to the sciatic nerve of a cat at 47 and 58 ℃. It was found that higher temperature-induced axonal degeneration, loss of myelinated fibres, heat-induced angiopathy, and reduction in nerve blood flow. Similarly, Tamai et al. [52] investigated nerve root injury in a rabbit model during bone drilling. McDannold et al. [53] predicted the brain tissue damage due to temperature variations in 26 rabbits at 63 different locations and tissue damage was seen at every location.

The critically important nerves for the human functioning like olfactory cranial nerves, sensation nerves, nerves for eye movement, facial nerves, pharyngeal nerves, and spines nerves are connected to the brain through the bone [54]. Owing to anatomical complexity and presence of vital neural tissues adjacent to the bone has raised concerns in the medical community about the temperature rise during bone grinding. It has been observed that nerves are vulnerable to elevated temperature and thermal damage at the cellular level (cell necrosis) could start at 43 ℃ [55]. However, the threshold temperature of 47℃ cause irreversible damage to the bone cells (bone death) also termed as osteonecrosis [33,51,56,57]. In more than 3.6% of cases, the occurrence of paralysis in the facial nerve during bone grinding operation has been reported [58].

At present, the conventional tool used during the neuro-surgery is a spherical diamond grinding burr rotating at a speed more than 50,000 rpm is used [35]. Neurosurgeons entirely depend upon

their personal experience to remove a part of the bone in such a way that temperature does not exceed threshold limit but still temperature rises above a threshold value and to control the temperature, saline irrigation is used. Even after using irrigation, the temperature does not control/limit to the desired level. This would be more difficult for novice surgeons as they are new in their practice. So, there is a need to develop an experimental setup and to explore an optimized way of grinding of bone to achieve the minimum forces and temperature during bone grinding. Furthermore, in the current scenario, the need of the hour for the neuro-surgeons is a real-time measurement technique which will be highly beneficial for both novice and experienced surgeons.

1.6 ORGANIZATION OF THESIS

The present work has been categorized into the following chapters for better insight into the work methodology and results achieved during the experimentation.

Chapter 1: This chapter gives information about the human bone, microscope structure of bone, grinding process and its complications. This chapter discusses the rotary ultrasonic machining process and different temperature measurement techniques. The threshold levels of the thermogenesis and osteonecrosis have been highlighted along with the advantages of using the rotary ultrasonic bone grinding. The need and motivation of the present work have also been discussed.

Chapter 2: In this chapter, an extensive literature review is accentuated along with brainstorming process parameters. The literature studied has been categorized into different categories. 2.1) In-Vivo clinical thermogenesis studies on bone, 2.2) In-Vitro conventional drilling on bone, 2.3) In-Vitro conventional grinding on bone, 2.4) Rotary ultrasonic machining on hard and brittle materials, 2.5) Rotary ultrasonic machining on a bone.

Chapter 3: This chapter presents the bone grinding experimental setup along with workpiece and tooling. The experimental design and experimentation procedure are well explained in this chapter. The characterization techniques used to investigate the bone grinding process has been explained. The information about the statistical analysis is provided to determine the effect of individual parameters on response variables. The biological effect on the tissue during the bone grinding has been studied using the histopathology and its entire procedure is accentuated in this chapter.

Chapter 4: This chapter discusses the results observed during rotary ultrasonic neurosurgical bone grinding and conventional bone grinding. The temperature readings observed for the range of process parameters have been given along with the infrared thermograms. The parametric effect has been discussed along with comparative histopathological analysis.

Furthermore, the wear occurred on the lateral and end face of the tool has been discussed for different shape of the grinding burrs. The bone debris settled within the successive diamond abrasive grits have been discussed and corresponding surface micrographs have been presented. Furthermore, the abrasive wear and burr loading have been quantified for different shapes of the tools. The surface micrographs highlighting the impact of cutting force on cracks generation and propagation has been discussed along with the material removal mechanism.

Chapter 5: This chapter discusses the use of thermal dose model for predicting the tissue damage and cell necrosis. Thermal dose integrates the temperature over time to quantify the thermal effect on bone tissues in terms of cumulative equivalent minutes at 43°C i.e., CEM43°C. Furthermore, the finite element model has been developed in ANSYS software and analysis has been used to determine the sub-surface temperature of the bone. Subsequently, the sub-surface temperature is used to measure the depth of thermogenesis and osteonecrosis during bone

grinding. Furthermore, the results have been verified with thermal dose model and histopathological analysis.

Chapter 6:

This chapter presents the conclusions of the work carried out on bone grinding setup and its scope of future work.

1.7 SUMMARY

Human bone, which is very hard and brittle, is usually machined using the conventional grinding process to remove a part of the bone to reach the target region. In neurosurgical operations, bone grinding has been implemented worldwide to remove a part of the bone to create safe access for the identification and dissection of the benign and cancerous tumors present beneath the bone. The critically important nerves for the human functioning like olfactory cranial nerves, sensation nerves, nerves for eye movement, facial nerves, pharyngeal nerves, and spines nerves are connected to the brain through the bone [1]. The heat generated during bone grinding may lead to the thermogenesis and osteonecrosis. Furthermore, the estimation/measurement of the temperature at the grinding site is still under research and neurosurgeons depends upon their experience during clinical osteotomy. It has been observed that use of the thermocouples for measuring the temperature during bone grinding is not feasible and infrared thermography can be used for temperature measurement owing to its non-contact type nature. Furthermore, the infrared thermograms also assist in visualizing the spatial and temporal distribution of the temperature over the grinding site. The threshold levels of the thermogenesis and osteonecrosis have been highlighted along with the advantages of using the rotary ultrasonic bone grinding.

The need and motivation of the present work have also been discussed under the subsequent chapter of the thesis work.

CHAPTER 2: LITERATURE REVIEW

In this chapter, an extensive literature review is accentuated along with brainstorming process parameters. The effect of different parameters on the cutting force, torque, and most importantly on temperature is discussed. Human bone is usually machined using the conventional grinding process to remove a part of the bone to reach the target region. Most of the research carried out by previous researchers were focused on using a drill bit for bone drilling during orthopaedic surgical operations. But drilling cannot be used during the treatment of benign and cancerous brain tumors because it can cause severe damage to the underlying dura-mater within the brain. The heat produced during the osteotomy results in serious concerns like osteonecrosis, coagulation of blood, loss of facial muscle control, and loss of vision due to optic nerve damage. The soft tissues are highly sensitive to heat and causes severe damage to cervical and sciatic nerves. The effect of heating and processing time on tissues has also been discussed for arthroplasty process [59]. The tool wear and tool loading occurred during the grinding have a direct impact on cutting force, torque, and temperature which makes it crucial to study for orthopaedic and neurosurgical applications. Xi et al. [60] revealed that wheel wear and loading significantly amplifies the grinding forces which ultimately leads to the deterioration of the

workpiece surface. Similarly, Feng et al. [61] observed severe grinding tool wear at the corners of the tool and highlighted that tool wear has a significant effect on grinding force. On the same context, Malkin and Cook [62] measured the amount of dulling in the terms of wear flats produced on the grinding wheel and revealed that grinding forces have a strong impact on the wheel's wear. Moreover, higher grinding forces results in pain in human tissues [63,64]. It has also been evident that cutting forces increases as the axial depth of cut is increases owing to the increased size of cutting grit [65]. Hwang et al. [66] explained the growth of wear flats on the surface of the grinding wheel which primarily occurs due to the attrition and fracture wear.

In the present work, the literature studied has been categorized into different categories.

2.1) In-Vivo clinical thermogenesis studies on bone,

2.2) In-Vitro conventional drilling on bone,

2.3) In-Vitro conventional grinding on bone,

2.4) Rotary ultrasonic machining on hard and brittle materials,

2.5) Rotary ultrasonic machining on a bone.

2.1 IN-VIVO CLINICAL THERMOGENESIS STUDIES ON BONE

This section is dedicated to the thermogenesis and its consequences during bone osteotomy (grinding/drilling). Bone drilling studies have also been discussed to highlight the importance of temperature in terms of thermal injury to the soft and hard tissues. The irreversible death of bone cells is known as osteonecrosis which may collapse architectural bone structure and is one of the consequences of thermogenesis which could happen due to the numerous reasons like alcohol, excessive medication, accidental fracture, and heat exposure [67]. It has been observed that in grinding tissue damage depends upon the temperature elevation and duration to which the tissue

has been exposed to it. In cell culture studies, the breakpoint of the cell's carbonization is around 43 ℃ [55]. The extent of cell survival, coagulation necrosis, and thermal damage to the tissues is dependent upon the number of factors. For example, temperature elevation and duration of thermal exposure are two factors which determine the thermogenesis for a particular tissue. These factors can be merged into a single metric known as thermal dose. The thermal dose models have been extensively used in past studies for evaluating the thermal effects [37,55,76–85,68–75]. Furthermore, biological effect, the equivalence among different temperature and lasting time have been explained and verified in the previous articles. Therefore, the same model has been used in the present study for evaluating the thermal effect of rising temperature and the corresponding degree of thermal burn. Thermal dose integrates the temperature over time to quantify the thermal effect on bone tissues in terms of cumulative equivalent minutes at 43°C i.e., CEM43°C. Sapareto and Dewey [82] in 1984 proposed a model CEM 43℃ to convert a time-temperature relationship into an equivalent number of minutes and successfully verified with clinical findings. Thermal dose integrates the temperature over time to quantify the thermal effect on bone tissues in terms of cumulative equivalent minutes at 43°C i.e., CEM43°C. It generally refers to the minutes required to cause the same effect under constant heating at 43°C. The cell killing rate is always dependent on exposure time and temperature. It has been observed that sub-lethal damage is reported at a temperature of less than 43°C and with shorter exposure time. The rate of cell death at temperature <43°C is very low owing to the development of thermal tolerance. However, no thermal tolerance is noted when the temperature reaches above the threshold temperature of 43°C [78]. It has been reported that cell killing rate doubles for every degree rise in temperature above 43°C [77]. On another side, it reduces by a factor of four

on every degree below 43°C [78]. Sapareto et al. [86] suggested an analogy to study the kinetics of cell killing with the Arrhenius model at different temperature and exposure time.

This method has been widely used for describing hyperthermia in RF-heating treatments. This method also provides the analogy to study the kinetics of cell killing with the Arrhenius model at different temperature and exposure time. Henriques F.C [85] formulated the Arrhenius model in 1947 to predict the extent of thermal damage using transient temperature solution for epithelial tissues. Some researchers suggested that there is a little tissue damage below the threshold value while other assumes Arrhenius relationship between exposure time and temperature rise in temperature exceeds the threshold value. Biologically, temperature escalation causes vaporization of the water present in the cells. Subsequently, dehydration leads to cessation, shrinkage, and rupture of the cell membrane and ultimately results in carbonization. In the case of bone grinding, osteonecrosis occurs due to a rise in temperature and heat exposure for some time. The risk of osteonecrosis increases due to the osteocyte apoptosis, reduction in blood flow, and osteoclastic resorption during bone grinding [87]. The histograms are shown in Figure 2.1, clearly shows lacunas, which are the distinctive feature of the thermal necrosis.

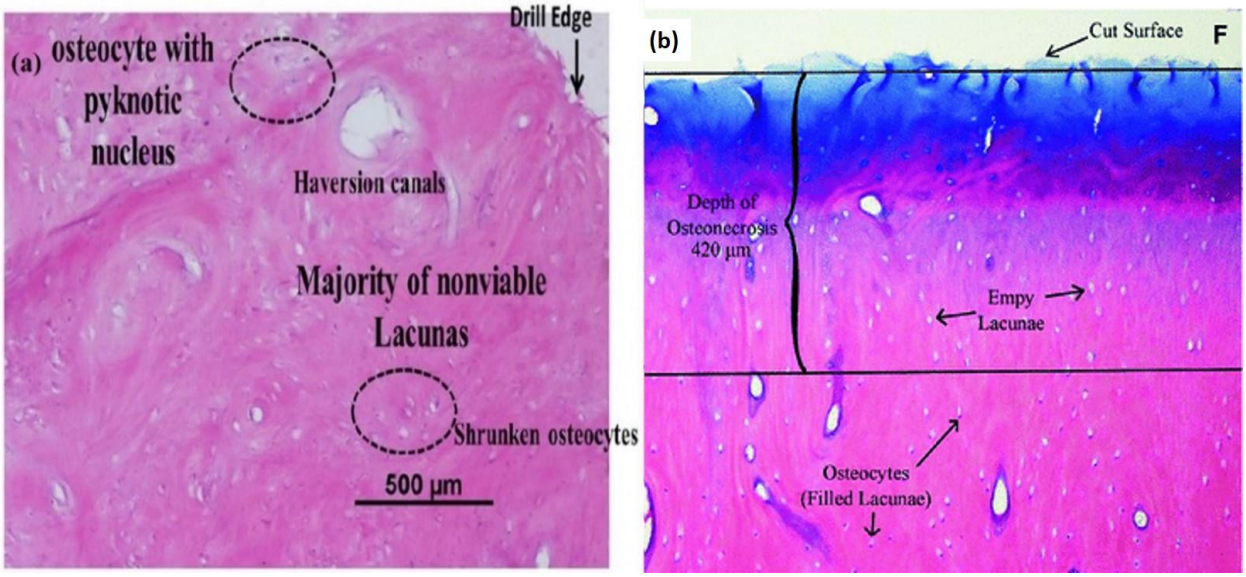

Figure 2.1: Histopathology images of the cut surface during bone machining. (a) pyknotic nucleus and non-viable lacunas [7] and (b) empty and filled osteocytes [88].

The collapse of bone structure can cause joint pain, bone destruction, and loss of function. Initially, bone exhibits normal phase with strong architectural bony structure [89]. Then as the osteonecrosis initiates, the functioning of the cell gets affected because of an absence of an enzyme called lysyl-tRNA-synthetase is vital for the functioning of the cell and is highly susceptible to the temperature change [90]. Additionally, this elevated temperature initiates denaturation process which significantly affects the collagen's functioning [91]. Recently, Babbar et al. [37] successfully used CEM43℃ based Arrhenius hybrid model for the prediction of thermal trauma during bone grinding.

The effect on the bone at high temperature was studied histologically by the different researchers. The empty lacunas (non-viable) signify the death of osteocytes which is due to heat exposure for a definite time. The damaged portion i.e. necrotic zone was calculated by the volume of empty and filled lacunas. The existence of osteocyte lacunas is directly dependent on the temperature level. When the temperature goes beyond the threshold limit, these lacunas evaporate leading to the necrotic region. The damage to the lacunas is categorized into four stages: 1) viable lacuna which are normal living osteocytes, (2) shrunken osteocyte, (3) osteocytes with a pyknotic nucleus, (4) empty lacuna (non-viable) [52,92,93]. The exposure time also plays a significant role while determining thermal necrosis threshold limit. In this direction, the work done towards evaluating the effect of increased temperature on human body tissues under different exposure time has been accentuated in Table 2.1.

Table 2.1. Average temperature observed during osteotomy.

Author and Year	Type of Species	Temperature	Exposure time	Remarks	Reference

Mortiz and Henriques (1947)	Pig	55 ℃	20 seconds	Irreversible thermal injury	[83]
Bonfield and Li (1968)	Bovine femur	50 ℃	-	Irreversible change in the structure of bone	[94]
Lundskog J (1972)	Rabbit	50 ℃	30 seconds	Bone death observed with histochemical evidence	[95]
Eriksson et al. (1984)	Rabbit Dogs Human	40 ℃ 56 ℃ 89 ℃	18 seconds	The difference in temperature occurs due to variation in cortical thickness of species. Bone necrosis observed	[96]
Berman et al. (1984)	Rabbits	67.5 ℃	1 minute	Necrosis of bone marrow Surgically damaged periosteum.	[97]
Monafo et al. (1987)	Rat	47 ℃	30 seconds	Irreversible damage to the sciatic nerve.	[56]
Uchiyama et al. (1989)	Canine spinal cords	45 ℃	30 minutes	Pigment exudation, vacuolation, and haemorrhage.	[98]
Hoogeveen et al. (1992)	Rat	43 ℃ 44 ℃ 45 ℃	30 minutes	No damage Mild oedema and vascular changes Severe damage to the destruction of the Neuron	[99]
De Vrind et al. (1992)	Rat	44 ℃	15 minutes	Loss of sensory functions The decrease in the amplitude of motor & reflex responses	[50]
Konno et al. (1994)	Pig	40 ℃ 60-70 ℃ 70 ℃	5 minutes	No change in nerve function Damage to nerve fibre Complete loss of nerve root functioning	[100]
Xu and	Rat	47 ℃ & 58 ℃	-	Axonal degeneration	[51]

Pollock (1994)				Loss of myelinated fibres Heat-induced angiopathy Reduction in nerve blood flow	
Augustin et al. (2008)	Goat	47 ℃	1 minute	The threshold of thermal necrosis	[57]
Hosono et al. (2009)	Porcine lumbar spine	Diamond burr: 174 ℃ Steel burr: 77 ℃	115 seconds 78 seconds	Nerve root palsy Thermal damage to nerve roots	[25]
Olson et al. (2011)	Human	63.9 ℃ ± 23.9 ℃	-	Severe burning of bone cells	[101]
Tamai et al. (2017)	Rabbit	52 ℃	60 seconds	Nerve root injury	[52]

As illustrated in Table 2.1, there is no general agreement on the exposure time and threshold limit up to which thermal necrosis could be prevented. It is believed that thermogenesis starts at 43 ℃ and temperature above 55 ℃ leads to coagulation of the structure of the cell (enzymes inactivation). On further increasing the temperature, the water present within the cells get evaporates due to which pressure rises within the cell and leads to carbonization and explosion of the cells [102]. However, maximum researchers [8,33,109–114,34,92,103–108] reported the average temperature of 47 ℃ for 60 seconds as the threshold limit for osteonecrosis.

McDannold et al. (2004) [53] predicted brain tissue damage due to temperature variations using MRI thermometry. A focused ultrasound heating was delivered to 26 rabbits at 63 different locations. Tissue damage was assumed as a function of peak temperature, acoustic energy, peak acoustic power, and thermal dose. During histology analysis, thermogenesis was seen at all locations with small to large areas of vascular damage. The temperature of 43 ºC was concluded as a threshold limit for tissue damage.

Gruber et al. (2005) [115] used the ultrasonic bone cutting device for osteotomy on 7 patients. The objective of the study was to find possible damage to surrounding nerves. It was seen that the ultrasonic bone cutting device took more time for osteotomy compared to conventional methods with saw, chisels, and burrs. But this concern was compensated by the high level of precision which was achieved with an ultrasonic device. Moreover, the control of operation was superior as a blood-free surgical field provided a clear vision of the machining area. This pilot study revealed that ultrasonic bone cutting device high level of safety to adjacent tissues due to its tissue-selective dissection nature.

Kelly et al. (2012) [32] highlighted the importance of different process parameters which can cause conceivable thermal damage to the neural tissues and osteonecrosis amid bone drilling. They investigated the factors that could lead to optic nerve injury due to a rise in temperature during drilling of bone. They placed a thermocouple inside the optic nerve canal and performed drilling for 30 seconds using CUSA NXT and Anspach eMax2 plus surgical high-power drill. A significant decrease of mean 3.3 ºC in the temperature was obtained using a diamond burr with continuous irrigation.

Yamamoto et al. (2013) [116] performed cervical spine-laminoplasty on 61 patients. A diamond burr of 3- and 5-mm diameter was used for intermittent drilling for 5- or 10-seconds duration with irrigation. Thermocouples were used to measure the temperature at the interface of tool and work. During the drilling, it was observed that there was a significant rise in the temperature. The average peak temperature achieved was 44 ºC for drilling session of 5 seconds. It was concluded that continuous cooling without irrigation may cause severe thermal injury and it was recommended that intermittent drilling may prevent thermal neuronal damage.

Tamai et al. (2017) [52] reported nerve root injury in a rabbit model during drilling during the lamina. Investigations were reported with irrigation (chilled or normal) and without irrigation. A 5 mm diamond surgical burr was used at a high-speed of 60,000 rpm. Sixty laminae were grouped into 3 (n=15, n=15, n=30) categories based on post-operative sacrifice. The results showed that beyond 60 seconds of drilling, the temperature around the nerve root reached up to 52 ℃. The thermal injury due to the drilling was seen immediately in one out of 3, three out of 14 after three days, and eleven out of 25 at seven days. The threshold level of the thermal necrosis as reported by the previous researchers have been highlighted in Table 2.2.

Table 2.2. Investigation of the threshold for thermal osteonecrosis.

Authors (Years)	Species Investigated	Conclusions
Mortiz and Henriques (1946)	Pig	Immediate damage to cells above 70 ℃
Bonfield and li (1968) [94]	Dog	Death of cells after 56 ℃
Lundskog (1968) [117]	Rabbit	Exposure for 30 sec caused irreversible death at 55 ℃
Eriksson & albrektson (1983) [118]	Rabbit	Osteonecrosis at 47 ℃ for 1 min exposure
De Vrind et al. (1992) [50]	Rat	Nerve damage starts at 43 ℃
Augustin et.al. (2009) [33]	goat	Thermal necrosis above 47 ℃
Olson et.al. (2010) [119]	Human bone	Severe burning of bone cells at 45 ℃
Tamai et al. (2017) [52]	Rabbit	Nerve root injury at 52 ℃

Matthes et al. (2018) [120] performed a clinical study on 90 patients and reported thermal necrosis to neural tissues during bony decompression of lumbar spinal stenosis. Three ways of osteotomy were compared namely conventional drilling with manual irrigation, conventional drilling with automatic irrigation and ultrasonic osteotomy with automatic irrigation. The temperature produced during the drilling was measured with an infrared thermography camera. It

was stated that the spinal cord is more sensitive to thermal damage. The results revealed the extraordinary benefits of ultrasonically assisted drilling (UAD) as a significant reduction in the temperature values was seen with ultrasonic actuation of the tool in comparison to the conventional drilling. The only disadvantage found was that UAD tool longer duration for drilling compared to other methods but this issue was overcome by the high precision and greater control of the drilling operation. It was observed that drilling with ultrasonic actuation was less prone towards thermal neural damage i.e., bone necrosis.

2.2 IN-VITRO CONVENTIONAL DRILLING ON BONE

The basic machining operation during any orthopaedic surgery may be influenced critically by varying the parameters. During grinding, the temperature generated at the wheel-work interface significantly affects the tool wear by softening the bonding material [121]. Yang et al. [122] designed a new drill bit and compared the results of drilling force and temperature during drilling of pig tibia bone with carbide and stainless-steel drill bit. The results showed that the change in drill's shape significantly reduces drilling temperature and forces. In 2017, Gupta et al. [104] studied the effect of the conventional drill bit and diamond coated hollow tool on temperature rise during drilling of porcine bone with spindle speed, feed rate, and drill outer diameter as process parameters. The results outlined that a lower rotational speed of 500 rpm, a feed rate of 10 mm/min, and drill diameter of 2.5 mm caused a lower rise in temperature while drilling with both drill bits.

Augustin et al. (2008) [57] reported a study in which an infrared thermography camera was used to determine the spatial distribution of the temperature during drilling of the porcine femoral

bone. They used only one set of input parameters to measure its effect on temperature. The parameters chosen were drill speed (1820rpm), drill diameter (4.5 mm), feed rate (84 mm/min), and drill point angle (100^{o}). The experiment was performed without irrigation and results highlighted that rise in temperature significantly affected by the hardness of bone. It was observed that bone marrow cavity aids in the removal of heat from the drilling zone and distribution of the temperature profile were irregular along the length of the cortical bone.

Daly et al. (2008) [123] used high-speed drills along with spray irrigation system (SIS) to increase the visibility in the surgery area and to prevent localized heating. To affirm the cooling effect of the irrigation system, a thermography study was performed. Then graphs were observed for spray-irrigation, without cooling and with irrigation every minute. It was found that local heating was reduced by 14-30% for spray- irrigation system compare to the irrigation system and air-jet mechanism of the SIS maintained a clear operative environment to perform surgery [25].

Wang et al. (2013) [19] investigated the effect of rotational speed, feed rate and drill bit diameter on force and torque during drilling of the bovine femur bone. The rotational speed, feed rate, and drill bit diameter were varied in the range of 550-900 rpm, 10-50 mm/min and 2.5-5 mm respectively. The outcomes highlighted that force and torque decrease in decreasing the feed rate and drill bit diameter and on increasing the rotational speed of the drill bit.

Jain et al. (2016) [108] investigated the effect of rotational speed, feed rate, and drill point angle on temperature rise during osteotomy of bovine bone. It was found that all three control logs of experimentation have a significant influence on temperature rise and rotational speed came out with a maximum contribution in heat generation i.e. 80.53%.

Jain et al. (2017) [111] performed multi-objective optimization of bone drilling parameters during drilling of bovine cortical bone as shown in Figure 2.2. Taguchi technique was modified and membership function was added to the approach for converting multiple responses into a single characteristic function. The study was carried out with three parameters rotational speed (1000, 2000, 3000), feed rate (50, 100, 150) and type of tool (twist drill, hollow pipe, abrasive coated). The effect of these input variables was determined on surface roughness and drilling force. The optimum parameters for minimum surface roughness and force were found to be rotational speed 1000 rpm, feed rate 50 mm/min and twist drill type of tool. It was noticed that type of tool was the most prominent parameter out of all input variables as its percentage contribution was 65.71 %.

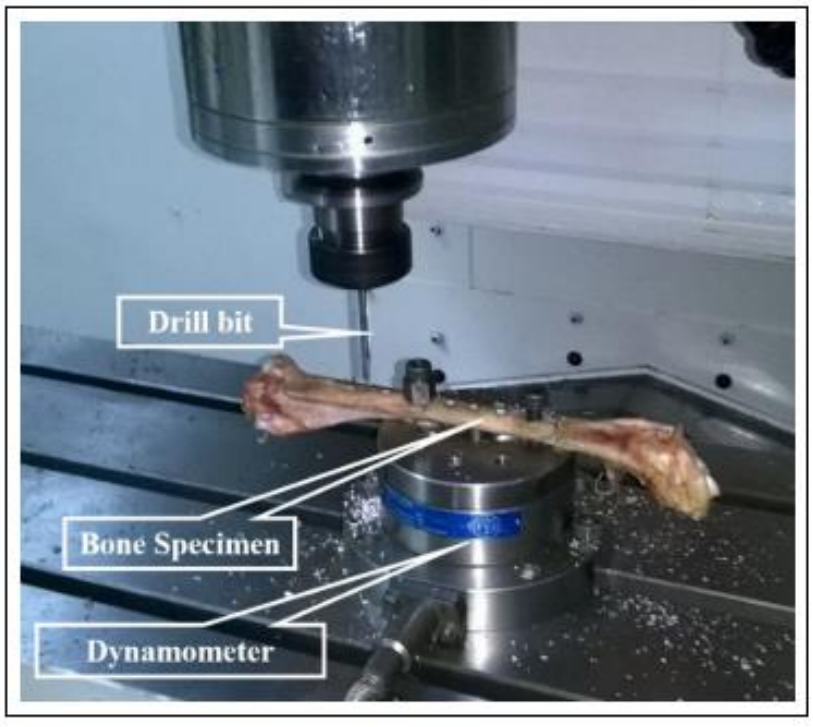

Figure 2.2: Conventional bone drilling setup [111].

Akhbar and Yusoff (2018) [124] performed a study to prevent the osteonecrosis by optimizing the bone drilling parameters. The investigation was reported with four input parameters rotational speed (1000, 2000, 3000 rpm), feed rate (0.04, 0.12, 0.20 mm/rev), tool diameter (2, 4, 6 mm), and depth of cut (1, 3, 5 mm). The simulation was carried out on DEFORM-3D software. The optimized set of parameters for minimum bone necrosis were found to be rotational speed 1000 rpm, the feed rate of 0.2 mm/rev, tool diameter 6 mm and depth of hole 1 mm. The maximum temperature achieved was below 46.7 ºC.

Cseke et al. (2018) [125] performed conventional rotary drilling on animal bone and biomechanical test materials. The effect of spindle speed and the feed rate was investigated for force, torque, and temperature. Three different workpiece materials were chosen namely SawBones® biomechanical test material, bovine cortical bone, and porcine femur bone. The levels selected for rotational speed were 700, 1000 and 1500 rpm and for the feed rate of 0.12, 0.15 and 0.2 mm/rev. The results revealed that force, torque and temperature decrease on increasing the rotational speed and on decreasing the feed rate.

Gupta et al. (2019) [126] reported a comparative study between the diamond-coated hollow tool and conventional twist drill during drilling of bovine cortical bone. The effect of spindle speed (500-2500 rpm), feed rate (10-50 mm/min) and outer diameter (2.5-4.5 mm) was investigated for the rise in temperature during drilling. The results concluded that the rise in temperature was lesser on using the diamond-coated hollow tool as maximum temperature obtained with the diamond tool was 48.2 ºC and with conventional drill bit 70.8 ºC. It was seen that lower spindle speed, feed rate and diameter results in less rise in the temperature.

2.3 IN-VITRO CONVENTIONAL GRINDING ON BONE

The neurosurgeons are primarily concerned with two aspects of bone grinding: 1) temperature measurement, (2) temperature control. At present, there is no device available which can provide real-time temperature measurements during the bone grinding. Neurosurgeons rely on their personal rich clinical experience for when to stop or start osteotomy. However, it is more difficult for novice surgeons because they are new in clinical practice. Secondly, hitherto, surgeons use saline irrigation for the removal of heat produced during the grinding. But, there are no guidelines for how much quantity of irrigation must be used? What should be the optimum flow rate for coolant delivery? What other cooling techniques could be used? Excess or scarcity of coolant may have adverse effects on the neural tissues. In this direction, attempts made by the previous researchers have been accentuated in the next two sections separately for the better understanding of the readers and to provide them with a comprehensive review of the recent innovations and methods used in the field of bone grinding.

2.3.1. Temperature Measurement

One of the most important aspects of bone grinding is the determination of temperature generated during the bone grinding. The heat generated during the bone grinding is transferred to the tool, bone debris, and bone itself. The maximum heat is carried away by the coolant and bone debris. However, the heat transferred to the bone gets entrapped in the bone owing to the low thermal conductivity (0.68 ± 0.01 W/mK) of the bone [9]. Consecutively, the temperature observed at the burr-bone interface surpasses safe hold limit of temperature which can cause damage to soft tissues as well as hard tissues. Figure 2.3 shows the experimental setup in which thermocouples have been used to measure the temperature at the bone grinding site.

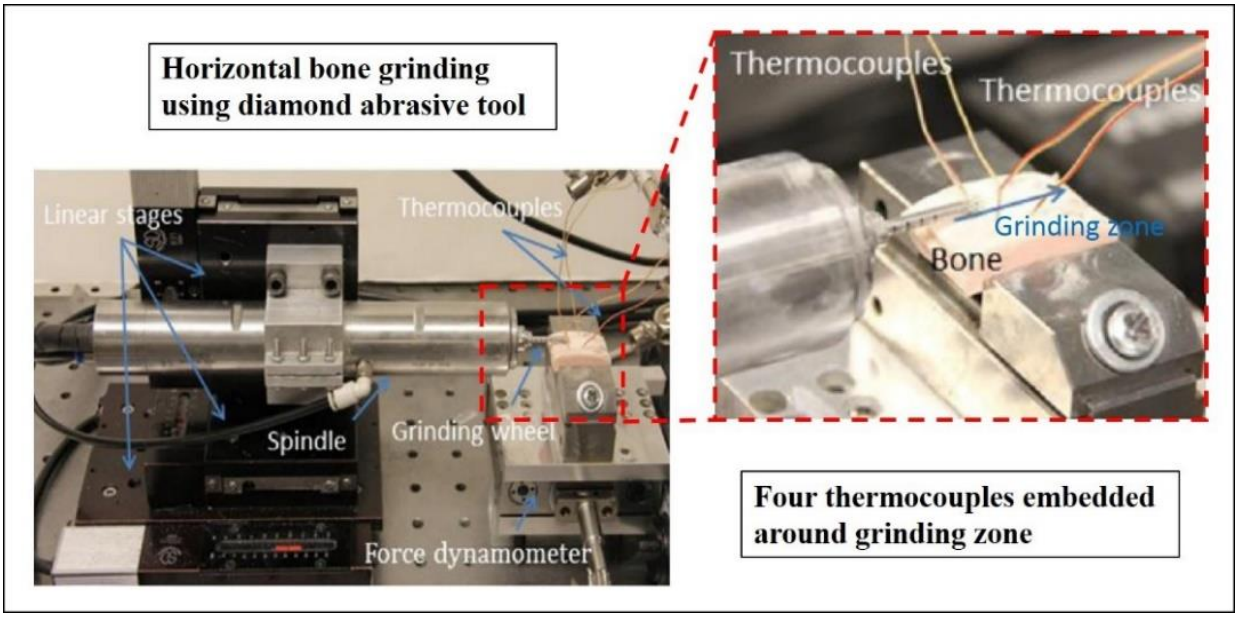

Figure 2.3: Four thermocouples used for measuring the temperature at the burr-bone interface during horizontal grinding [31].

Thermocouple and infrared thermography are the two techniques used for measuring the temperature rise during in-vitro bone grinding operations. A thermocouple consists of a pair of legs made from different conductors to form two junctions. Firstly, a hole is drilled in the bone for creating a space for the insertion of thermocouples in the near region of the grinding path. Generally, thermocouples are embedded within the range of 1-5 mm from the grinding zone [127]. Due to which their ability to give precise and accurate results declines.

Another remarkable technique i.e. simulation allows us to determine the temperature produced during grinding without investigating experimentally on animal and human bone. Simulating the temperature profile has been proven to be significantly effective in providing temperature reading and its distribution [128]. Different mathematical models are being developed for temperature estimation during grinding which shows a positive correlation with the experimental findings [129–133]. Since grinding is a complex process involving a lot of variables related to grinding force, torque, energy partition ratio, temperature, abrasive size and shape, tool dimensions, and abrasive density makes it difficult to model and simulate. But advanced computational techniques combined with ABAQUS and MATLAB software could allow us to predict the temperature rise during bone grinding. There is no doubt that thermocouples solved the problem of temperature measurement but it cannot be used for measuring the temperature of the bone's surface during the grinding process. However, in actual surgical operations, the use of thermocouples is not feasible because pilot holes are required in the bone to insert thermocouple in it. Moreover, thermocouples do not provide precise results as they are placed at a certain distance from the drilling/grinding zone. Due to which they are not able to give exact measurements of temperature. These limitations can be tackled by another technique i.e. infrared (IR) thermography technique. It is flexible Nondestructive testing (NDT) technique in which

infrared energy is emitted by the surface of the object, which is further detected by the infrared sensor. A 2D thermal image is obtained from these signals with one camera while the 3D surface can be achieved with a minimum of two cameras [134]. Temporal and spatial distribution of the temperature can be easily visualized by using this versatile technique [135,136]. Moreover, it is highly feasible for in-vivo surgical operations. Even though infrared technology is very useful for monitoring the temperature but inadequate information of bone properties specifically emissivity and technique's procedure is hindering its implementation in the operation theatre [14,137]. So, further investigations are required for the estimation of bone's thermal properties.

Shih et al. (2012) [31] used an inverse heat transfer method (IHTM) to predict the temperature during skull base neurosurgery. Heat flux (q) and thermal conductivity (k) of the bone was estimated. A diamond burr was used for grinding. A set of input parameters taken in this investigation were rotational speed of 60,000 rpm, a shank diameter of the tool of 4 mm, diamond abrasive size of 711 FEPA, the feed rate of 20 mm/min, depth of cut of 0.5 mm. It was observed that within 10 seconds, peak temperature increases beyond 50 ºC at the optic nerve.

Zhang et al. (2013) [19] proposed a thermal model to investigate the temperature during bone grinding with a spherical burr. They considered the rotational speed of 60,000 rpm, the feed rate of 20 mm/min, and the cutting depth of 0.4 mm for investigation. The maximum temperature at the tool-work interface was over 200ºC, while at the edge of the slot was 100ºC. The thermal injury prevailed up to 3 mm in the transverse direction and 3 mm below the ground surface under dry grinding conditions.

Tai et al. (2013) [16] developed a technique in which feedback of electrical motor was used to determine temperature rise. Heat flux was estimated with the help of IHTM under different environmental conditions. A round diamond burr was used for grinding of the bovine femur

bone. Investigations were reported by considering the rotational speed of 60000 rpm, the contact angle of 30º, the feed rate of 20-60 mm/min, and depth of cut = 0.5 mm. With less than 20% error in temperature estimation, this technique showed its capabilities in estimating possible temperature rise. The outcomes exposed that with 0.4-0.5 W grinding power, the temperature can rise beyond 50^0C in surrounding nerves.

Zhang et al. (2013) [138] used a spherical burr for grinding of bovine cortical bone. They explore the feasibility of using cool mist for temperature reduction. Bone grinding was performed using the rotational speed of 60,000 rpm, the feed rate of 20 mm/min, and depth of cut of 0.5 mm. the outcomes concluded that the rise in temperature decreases on using cryogenic saline mist and temperature achieved was less than 43ºC.

Danda et al. (2016) [29] used a diamond burr (surgical tool) for grinding the synthetic bone. The forces induced in the bone burring tools at high-speed were studied. Statistical analysis was employed along with the experimental methods to establish the correlations between burring motion and feedback of forces induced in the surgical tool. Two types of forces were analyzed i) Mean force ii) Vibrational force for different parameters. It was observed that there was no noteworthy correlation of feed rate with both the forces. Moreover, cutting and grinding burrs showed the difference in vibration and force data for a given combination of variables. It was observed that higher efficiency and lower burring force achieved at a tilt angle of 30 ºC because vibrational force was at its lowest at this angle. The different methods adopted by past researchers in the field of bone grinding has been summarized in Table 2.3.

Table 2.3. Literature recap of conventional bone grinding.

Authors (year)	Reference	Workpiece and tooling	Technique used	Findings/conclusions
Tai et al. (2012)	[127]	Bovine cortical bone Diamond burr	Inverse heat transfer method Thermocouples FEM model prepared in ABAQUS software. Estimation of heat flux, thermal conductivity, and thermal power	Temperature prediction model established. Peak temperature surpasses 50 ºC at optic nerve within 10s Developed models could become planning and training tools for surgeons Heat partition ratio: 0.6-0.7%
Wang et al. (2013)	[16]	Bovine femur bone Diamond round burr	Thermocouples Pulse-width modulation Inverse heat transfer method Dry grinding	Feedback of the electrical motor was used for predicting temperature Predicted results consistent with empirical measurements Electrical power positively correlated with thermal power In actual surgery, irrigation is used but here dry grinding was employed The proposed method proved to be feasible for temperature prediction with less than 20% error
Zhang et al. (2013)	[19]	Bovine cortical bone Spherical diamond burr	Inverse heat transfer method Finite element transfer method Malkin's triangular heat flux model in 3D	3D FETM- based grinding model proposed for temperature prediction The maximum temperature at the tool-work interface was over 200ºC, while at the edge of the slot was 100ºC

				The thermal injury prevailed up to 3 mm in the transverse direction and 3 mm below ground surface in dry grinding conditions
Danda et al. (2016)	[29]	Synthetic bone Diamond burr	Parallel burring Perpendicular burring MATLAB algorithm is used	Higher efficiency and lower burring force were obtained at 30º burring angle Feed rate had an insignificant effect
Wang et al. (2016)	[35]	Bovine femur bone Spherical diamond burr	Hybrid approach SFSM and SQP. Inverse heat transfer method	Experimental data incorporated with IHTM to estimate heat flux distribution Higher heat flux in the feed direction SFSM and SQP combined to calculate temporal and spatial variables simultaneously Triangular temperature distribution observed along the transverse direction
Shakouri et al. (2019)	[139]	Bovine femur bone Diamond burr	Infrared thermography	At all tested combinations of the parameters, thermal necrosis has been observed.

From the literature recap, it is clear that thermocouple is an often-implemented technique for temperature measurement. But in actual surgical operations, it is not feasible to first drill hole in the patient's bone thereby inserting thermocouples for the measurement of temperature. Therefore, infrared thermography technique has a lot of potential for the usage in operation theatre owing to its non-contact type nature. The information about the effect of varying process parameters and optimum grinding parameters for minimum temperature rise during the grinding is still scarce. Further, there is a need for the improvement in bone grinding methods and process efficiency for avoiding thermal necrosis during grinding.

2.3.2 Temperature control

The key aspect of bone grinding is to control and limit the temperature below the threshold level of osteonecrosis. During an osteotomy, the bone chips get settled within the successive abrasives and cause more rise in temperature during bone machining due to burr loading [137]. Effective irrigation with an optimum flow rate helps to mitigate the friction by efficiently removing the bone debris during the machining process [140]. In this direction, different researchers have explored various techniques. Internal and external cooling are the two methods which are extensively used for controlling the temperature during bone osteotomy (grinding/drilling) [35,87,141–143]. In internal cooling, coolant flows through the tunnels build inside the tool. Whereas, in external cooling, coolant is externally fed in the machining zone via external means such as drip irrigation etc. In the field of machining, mist cooling technology plays a significant role in mitigating temperature rise during grinding [30]. Mist cooling alludes to high-pressure air-flow (atomized) at a range of 4.0 bar to 6.5 bar [138]. The consumption of mist cooling and traditional grinding fluid flood cooling varies for a unit width of the grinding wheel which is 30 mL/h to 100 mL/h for mist and 60 L/h for fluid [138,144]. The clearer operative field is one of the major benefits of mist cooling technology. The flood irrigation and mist cooling during the bone grinding. Morris et al. [36] used high-

speed drills along with spray irrigation system (SIS) to increase the visibility in the surgery area and to prevent localized heating. It was found that local heating reduced by 14-30% for spray- irrigation system compare to the simple irrigation system. Furthermore, the air jet mechanism of the SIS maintained a clear operative environment to perform surgery. Kondo et al. [145] reported a maximum temperature of 47 °C during endonasal endoscopic skull base surgery with 720 ml/h saline flow rate and a further increase in temperature beyond 47 °C could result in the damage to brain tissues and nerves. In bone grinding, saline cooling is the fundamental cooling mode, however, the constrained space and high-speed grinding burr limits the effectiveness of saline cooling. The ideal cooling system can viably lessen the generation of heat, cool the bone without meddling with the operation procedure, and keep the operation area clean. Such a cooling system is what the surgeons require direly. Recently, the cooling performance of nanofluids, vegetable oil or base oil, vegetable oil-based nanofluids and Nanoparticle jet mist cooling (NJMC) has also been investigated and the excellent cooling and lubrication effects of NJMC have been confirmed [144].

Enomoto et al. (2014) [146] developed a new grinding wheel coated with titanium dioxide (TiO_2) and silicon oxide (SiO_2) particles. The size of TiO_2 particles was in the nanometer range with diameter 180 nm. Bovine femur bone was taken as workpiece material and abrasive coated wheel as a tool. Different input parameters like the rotational speed of 5000 rpm, the feed rate of 1 mm/min, the coolant flow rate of 180 mL/h, and diameter of diamond burr of 5 mm were considered in the study. Noticeable reduction in heat generation and grinding torque was achieved using such a grinding wheel which demonstrates its effectiveness against temperature rise.

Tai et al. (2016) [35] proposed an inverse method in which sequential function specification method (SFSM) combined with sequential quadratic programming technique to evaluate both temporal and spatial parameters. The investigation was performed with the rotational speed

of 60,000 rpm, burr diameter of 4 mm, contact angle of 30º, the feed rate of 20 mm/min, bone density of 2050 kg/m^3, Contact angle = 30º, the thermal conductivity of 0.5 W/mK, and initial temperature of 20 ºC. The results highlighted that this SFSM-SQP coupled approach could predict heat flux distribution.

Li et al. (2017) [147] performed experimental research in microscale bone grinding using a different type of nanofluids and concentrations. The workpiece used was bovine femur bone and nanofluids like hydroxyapatite (HA), SiO_2, Fe_2O_3, and carbon nanotubes (CNT) were used in the fraction of 2%, 4%, 6%, 8% and 10% resp. The results showed that temperature peaks varied inversely proportional to the mass fraction for a certain range and after that varies linearly with a mass fraction. It was concluded that thermophysical properties, shape and mass fraction of nanoparticles strongly influences their micromotion which in turn will influence the temperature in the grinding zone.

Jia et al. (2017) [144] performed a simulation study on the temperature field using dynamic heat flux density model. Bovine femur bone was taken for experimental study and grinding force signals were recorded. The results highlighted that lowest surface temperature was obtained in the order of 30, 50, 70 and 90 nm particle size and the corresponding temperature was 21.4%, 17.6%, 16.1%, and 8.3% lower than 33.6 ºC which was obtained on using cryogenic mist. The maximum heat convection coefficient of 1.8723 W/mm^2K was achieved at 30 nm particle size. The simulated temperature readings were validated with experimental findings. It was noted that the temperature of the surface of bone increases with an increase in nanoparticle size.

Jia et al. (2018) [11] investigated the temperature field under different grinding conditions like mist, dry, drip cooling and nanoparticle jet mist cooling (NJMC). A diamond-coated burr was used for microscale grinding of bovine femur bone with parameters rotational speed of

60,000 rpm, Feed rate of 120 mm/min, depth of cut of 0.01 mm, drip flow rate of 50 mL/h, mist flow rate of 10 mL/h. NJMC flow rate of 10 mL/h, MQL pressure of 0.54 MPa, nozzle diameter of 15 mm, nozzle angle of 15º. It was found that NJMC showed minimum temperature (27.5 ºC) followed by mist cooling, drip cooling, and dry grinding consecutively. The peak temperature obtained was 41.6 ºC in case of dry grinding, which was 10.1% higher than drip cooling, 29.3% higher than mist cooling and 37% higher than NJMC.

The results obtained by the past researchers highlighted that nanoparticle jet mist cooling has the potential to reduce the temperature produced during grinding. But no clear recommendations are given for its use. Additionally, the biological interaction of nanoparticles with human body tissues has not been explored. However, many researchers have investigated the biological effects of saline irrigation on human body tissues and outcomes revealed that excessive irrigation may damage neural tissues. So, there is a need to find an alternative way of cooling without damaging the neural tissues. Table 2.4 demonstrates the work done by past researchers in reducing the temperature produced during bone grinding.

Table 2.4. Different techniques used to suppress temperature during bone grinding.

Authors and Year	Reference	Workpiece and tooling	Technique used	Findings/Conclusion
Zhang et al. (2013)	[138]	Bovine cortical bone Spherical burr	Cryogenic mist Thermocouples	The rise in temperature decreases on using cryogenic saline mist The temperature achieved was less than 43ºC
Enomoto et al. (2015)	[146]	Bovine femur bone Abrasive coated wheel	Titanium oxide and silicon oxide coatings Thermocouples	The significant reduction in temperature was observed by using the TiO_2 coating on the wheel surface Wheel loading reduced due to the hydrophilic nature of TiO_2

Yang et al. (2016)	[147]	Bovine femur bone Abrasive coated wheel	Nanofluids with hydroxyapatite, SiO_2, Fe_2O_3, carbon nanotubes	Inconsistent temperature profile obtained for the mass fraction Shape, size, and thermo-mechanical properties of the nanoparticles may influence temperature rise Mass fraction: SiO_2 = <6% Fe_2O_3 = 4-8% CNT = 2-6%
Yang et al. (2017)	[144]	Bovine femur bone Diamond-coated burr	Dry grinding Drip grinding Mist cooling Nanoparticle jet mist cooling Thermocouples	It was found that NJMC showed minimum temperature (27.5 ºC) followed by mist cooling, drip cooling, and dry grinding consecutively The peak temperature obtained was 41.6 ºC in case of dry grinding, which was 10.1% higher than drip cooling, 29.3% higher than mist cooling and 37% higher than NJMC
Yang et al. (2017)	[11]	Cattle femur bone Diamond-coated burr	Simulation	Mist cooling temperature 33.6 ℃ Minimum temperature observed for 30 nm size followed by 50, 70, 90 nm consecutively Simulated results were consistent with experimental results Surface temperature and size positively correlated
Mizutani et al. (2018)	[148]	Bovine femur bone Diamond-coated burr	TiO_2 coating Trifluoromethyl surface coating	New wheels with hydrophobic porous layer developed Developed wheel significantly reduced temperature produced during grinding

2.4 ROTARY ULTRASONIC MACHINING ON HARD AND BRITTLE MATERIALS

Li et al. (2005) [149] compared rotary ultrasonic drilling (RUD) with conventional drilling (CD). A diamond-coated abrasive tool was used for drilling on ceramics matrix composites

(CMCs). The experimentation was carried out with three input parameters ultrasonic power, spindle speed, and feed rate. The levels were taken in the range 35-50% for ultrasonic power, 17-50 rps for spindle speed and 0.09-0.15 mm/s for feed rate. The measured output characteristics were cutting force, material removal rate, and hole quality. The results highlighted that RUD performed superior to CD as a cutting force was reduced by 50% in RUD while the material removal rate showed significant improvement in material removal rate by 10%. ANOVA analysis showed that all input parameters were significant.

Churi et al. (2006) [150] investigated material removal rate, surface roughness and cutting force during rotary ultrasonic drilling of titanium alloy. Three parameters taken for this work were spindle speed, feed rate, and ultrasonic power. The effect of a change in input parameters was studied for material removal rate, cutting force, and ultrasonic power. The outcomes revealed that maximum cutting force was achieved at 30% ultrasonic power while feed rate of 0.25 mm/sec caused higher material removal rate.

Pei et al. (2012) [151] performed a feasibility study on carbon fibre reinforced plastic using rotary ultrasonic machining (RUM). The effect of rotational speed, feed rate, and vibration amplitude was investigated for edge chipping, tool wear, surface roughness, and thrust force. The results concluded that RUM could be used for high surface finish and lesser thrust force. High rotational speed and the lower feed rate were recommended in this investigation for higher productivity.

Chai and Song (2012) [152] used rotary ultrasonic grinding for machining the ceramic material (ZrO_2) block with dimension 35mm × 8mm × 40mm, composition 94.8% ZrO_2 and 5.2% Y_2O_3, and hardness 11GPa. Taguchi L_9 orthogonal array design was used with four input parameters wheel speed, abrasive mesh number, feed rate and depth of cut. The results revealed that there was a significant reduction in surface roughness on using rotary ultrasonic

grinding process and optimal levels for input parameters came out to be wheel speed 1000 rpm, depth of cut 0.1 mm, feed rate 3 mm/min and 240 mesh number.

Zhang et al. (2014) [137] investigated rotary ultrasonic drilling (RUD) on the optical K9 glass for different process parameters. The response of input parameters spindle speed (2000-5000 rpm), feed rate (0.01-0.04 mm/s), ultrasonic power (0-50%) was studied on output characteristics cutting force, surface roughness and power consumption. The recommended set of parameters for minimum surface roughness were rotational speed of 5000 rpm, the feed rate of 0.01 mm/s and ultrasonic power of 20%. RUD results in lesser cutting forces in comparison to the conventional drilling process.

Geng et al. (2014) [153] made a comparative analysis for drill wear mechanism in RUM and CD. The workpiece chosen was CFRP composites and parameters considered spindle speed, feed rate, and drilling depth. The response of these parameters was studied for the drilling force, tool wear and tool life. The significant reduction in the drilling force was achieved with RUM compared to CD and tool life increased by 28%. The higher material removal rate was attained with rotary ultrasonic machining.

Cong et al. (2016) [154] made a comparative analysis for conventional grinding (CG) and rotary ultrasonic machining (RUM) of carbon fibre reinforced plastic. These two drilling methods were compared on different characteristics like cutting force, torque, surface roughness, hole diameter, and material removal rate. The outcomes revealed that for equal material removal rate force and torque values were higher in CG than RUM. Moreover, surface roughness was higher in the case of CG and hole size consistency was less. It was observed that the material removal rate was higher in RUM compared to CG.

Wang et al. (2017) [155] used rotary ultrasonic machining for surface grinding of optical BK7/K9 glass. An experimental investigation was done to determine the effects of ultrasonic

power on cutting forces, torque, surface roughness, and edge chipping. The machining parameters selected were tool rotational speed (3000 rpm), depth of cut (0.75 mm), feed rate (1 mm/s), tool abrasive size (60-80), and ultrasonic power levels (0, 20, 40, 60, 80 %). The results revealed that ultrasonic vibration significantly reduced the cutting forces and correspondingly torque also reduced increasing the ultrasonic power.

Jain et al. (2019) [126] reported a tool wear study for conventional drilling (CD) and rotary ultrasonic drilling (RUD). Five different diamond-coated abrasive tools were chosen for drilling in amorphous solid. The microscopic analysis of the tool before and after drilling showed that wear and grains fracture caused during CD. It was outlined that RUD causes less damage to the tool and can be used for a longer duration.

2.5 ROTARY ULTRASONIC MACHINING ON BONE

Rotary ultrasonic machining (RUM) is gaining higher attention from the researchers worldwide due to the less heat generation and high surface quality involved in such a process. In one of the studies [45], it was reported that ultrasonic drilling provides better control over the process and cause less damage to the underlying dura mater while conventionally rotating drill bit can sternly harm the soft tissues. Moreover, unlike conventional processes rotary ultrasonic-assisted machining does not generate bone chips which reduce the chances of infection. Due to the combined material removal action of vibrational and conventional drilling, more material removal is observed in RUM than conventional process [46]. The desire to reduce the temperature generated during bone machining and further to increase the quality of processed bone coupled with environment-friendly characteristics, rotary ultrasonic-assisted grinding plays a key role. Some of the benefits are illustrated in Figure 2.4 and 2.5 below:

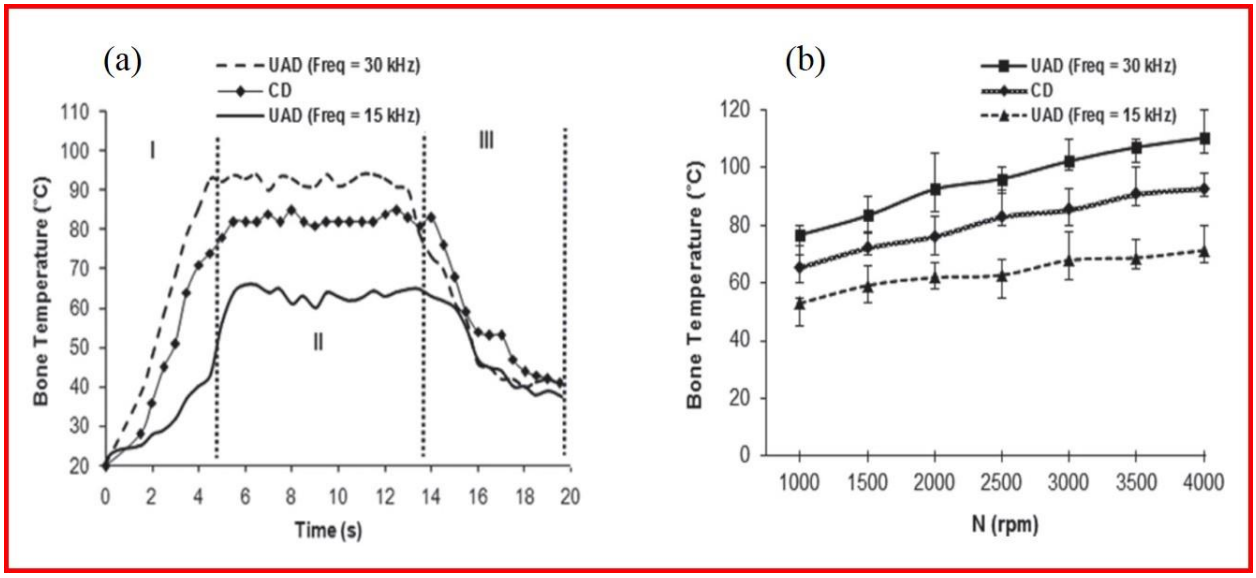

Figure 2.4: Comparison of bone temperature in Conventional Drilling (CD) and Ultrasonic Assisted Drilling (UAD): (a) less temperature was observed in Ultrasonic assisted machining in three different stages (I – Initial drill-bone contact stage; II – drilling with full lips engagement with the bone; III – retraction stage); (b) different speeds which show that less temperature was observed in Ultrasonic-assisted drilling (feed rate −50 mm/min, vibration amplitude −10 μm) [156].

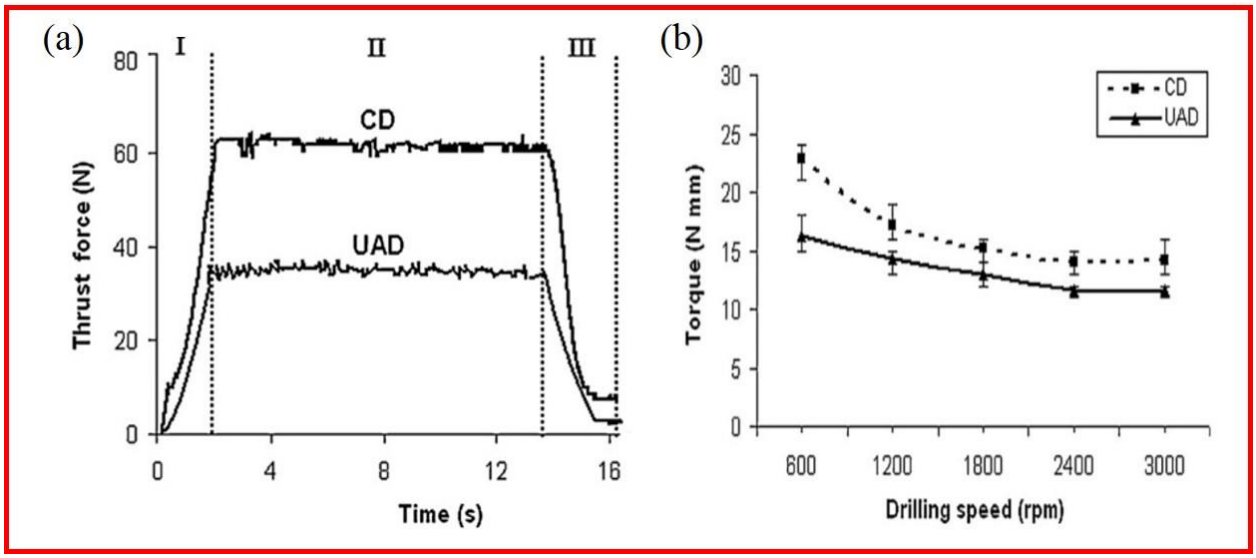

Figure 2.5: Comparison of Conventional and Ultrasonic Assisted Drilling; (a) Thrust force Vs Time; (Drilling speed N =1800 rpm; Feed Rate =40 mm/min) (I – drill engagement stage;

II – drilling; III – drill exit) (b) Torque Vs Drilling speed; (Frequency f = 20kHz, amplitude a =10µm, feed rate = 40mm/min.) [156]

Beyond economics, rotary ultrasonic-assisted machining offers many technical aspects which were discovered by various authors and these include better microstructures, finer structures, lower defects, and better surface finish, less delamination of surface and enhanced mechanical properties. These characteristics have been reported in Figure 2.6 and 2.7.

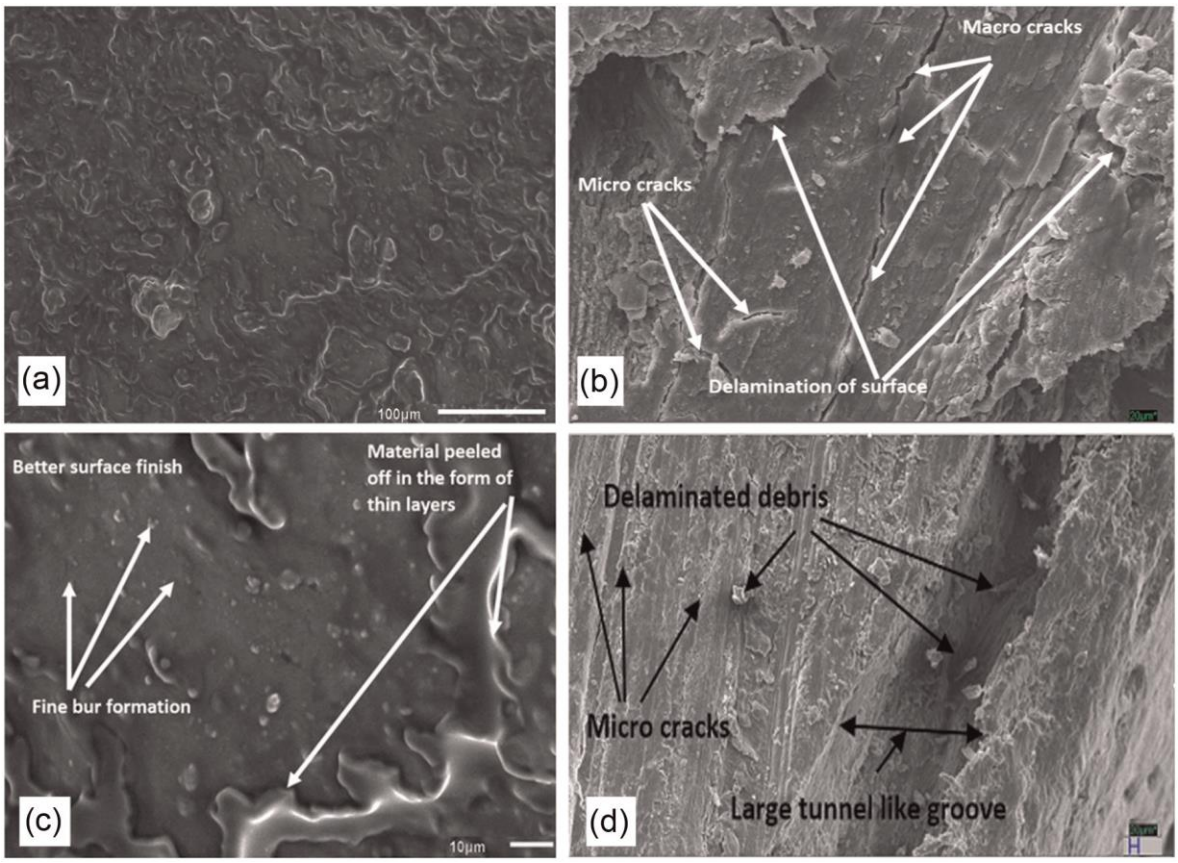

Figure 2.6: SEM image of the drilled bone surface which shows that minimum surface damage in UAD as compared to CD (a) bone drilled using UAD, (b) SEM micrograph of CD drilled bone. (c) ultrasonic drilled bone and (d) CD bone [105].

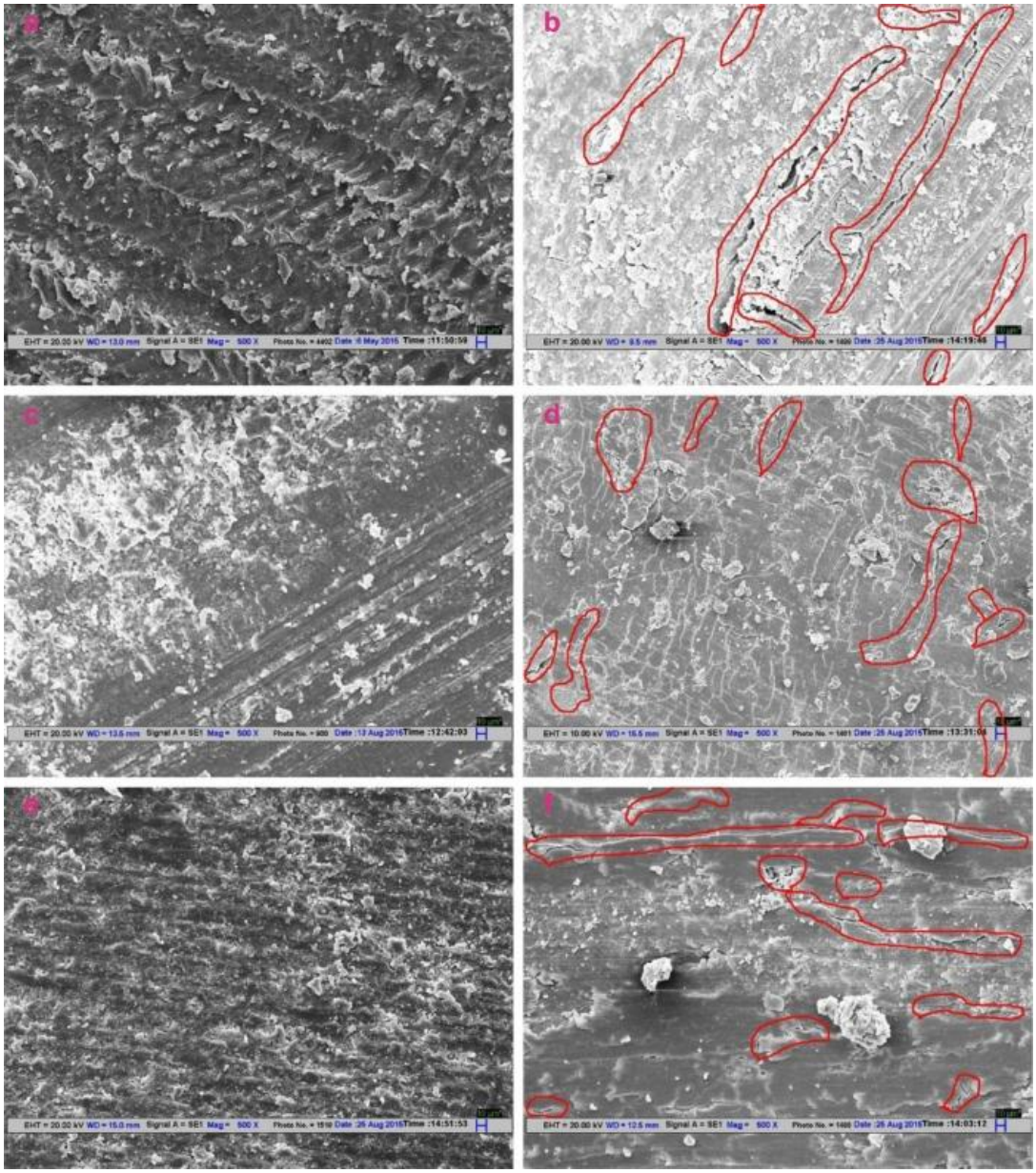

Figure 2.7: Comparison of CD and UAD; Effect of rotational speed on microcracks generation: (a), (c), (e) UAD; (b), (d), (f) CD group, indicating UAD produces fewer cracks than the CD [103].

Karaca et al. (2011) [157] investigated various parameters such as rotational speed, feed rate, mineral density, drill force, bone sex, and tip angle during conventional bone drilling of calf tibias. Statistical and histological analysis was also carried out for determining possible thermal damage. It was found that temperature had an inverse relation with feed rate and drill force while had a direct relation with drill speed. The rise in temperature was more in case of

female tibia than the male tibia. Increasing the drill tip angle and mineral density also increased maximum temperature during drilling. Moreover, the quality of bone in case of high temperature was worse than the region under low temperature.

Alam et al. (2011) [158] experimentally investigated the force and torque during CD and UAD of cortical bone as shown in Figure 2.8. Investigations were carried out by considering four input parameters rotational speed, feed rate, amplitude, and frequency. It was observed that force decreases by 27% in the range of 600-3000 rpm for CD and by 55% in UAD. There was a significant reduction in the force on decreasing the amplitude whereas feed rate had less effect on output in UAD. The frequency was varied in the range 10-30 kHz and the corresponding decrease in force and torque was 57% and 28% respectively. For 5-15 µm variation in amplitude, the force decreases by 46% and torque decrease by 14%.

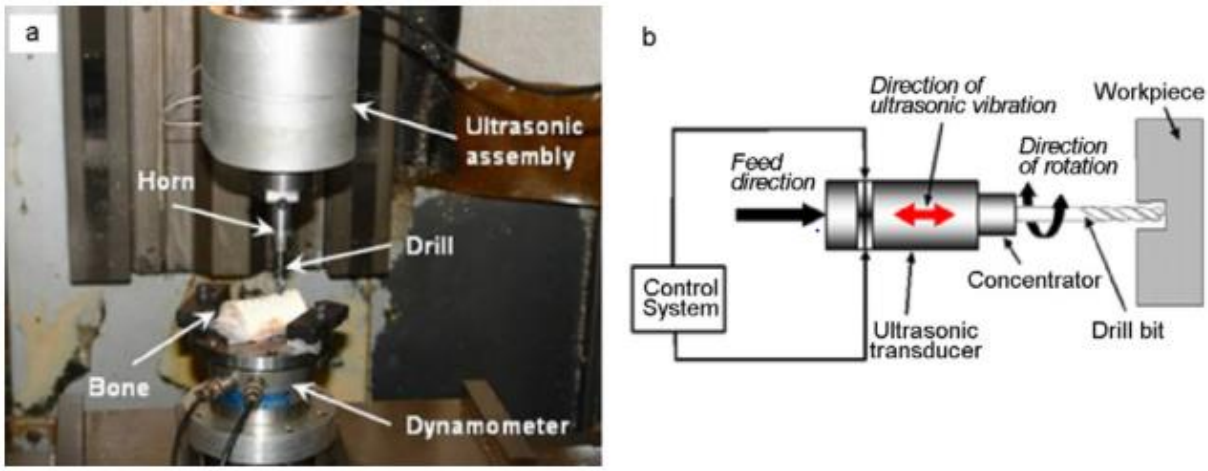

Figure 2.8: Ultrasonic bone drilling setup: (a) Experimental arrangement for measurement of thrust force and torque in drilling; (b) schematic of the ultrasonic device for drilling [49]

Alam et al. (2014) [159] performed a rigorous analysis of temperature in conventional and ultrasonic-assisted drilling (UAD). The workpiece chosen was bovine femur bone and investigations were carried out to determine the effect of drilling speed, feed rate, amplitude, and frequency of temperature rise. The results showed in both cases temperature rose above

the threshold value for thermal necrosis using high speed and feed rate. The amplitude of vibration had no significant effect on temperature while UAD with a frequency of less than 20 kHz caused lower temperature rise.

Hao et al. (2015) [45] drilled a micro-hole on cat skull bone with the assistance of applied ultrasonic vibration. A conically tipped tool (300 μm in diameter) was actuated with 29.7 kHz frequency. Microstructural and finite element analysis revealed that a micro-hole can be successfully drilled in a skull bone without damaging dura mater. The possibility of infection was significantly reduced with the use of ultrasonic actuation. A significant reduction in the cutting force was observed with the increase in the amplitude of the vibration.

Shakouri et al. (2015) [80] compared conventional drilling with the rotary ultrasonic drilling of the bovine femur bone as shown in Figure 2.9. Investigations were carried out to prevent thermal necrosis during drilling of bone with input variables cutting speed (500, 750, 1000, 1500, 2000) and feed rate (500, 100, 150) while the depth of cut, frequency, the amplitude was kept constant. The results demonstrated that rotary ultrasonic drilling significantly reduce the temperature and cutting force in comparison to conventional drilling. It was seen that temperature rise in vibration-assisted drilling was more at a low rotational speed. But on increasing the rotational speed, the rise in temperature decreases. Furthermore, the thermal injury was minimum at a rotational speed of 1000 rpm and a feed rate of 100 and 150 mm/min. It has been observed that feed rate had no significant effect on the rise in the temperature.

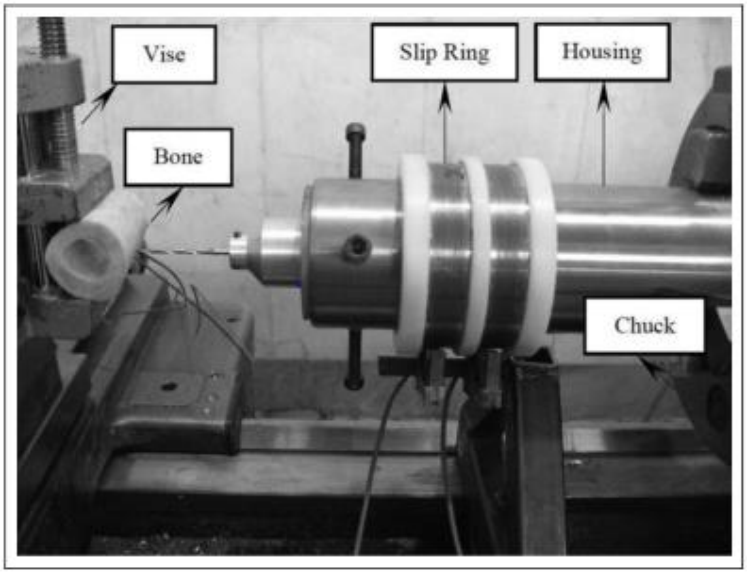

Figure 2.9: Ultrasonic-assisted drilling process [51]

Gupta and Pandey (2017) [34] used a diamond-coated abrasive tool for rotary ultrasonic drilling (RUD) and conventional drilling (CD) of bovine cortical bones. The parameters like rotational speed, feed rate, drill diameter, amplitude, and frequency were investigated for thermal necrosis. The temperature readings were recorded by using a k-type thermocouple. It was noticed that RUD results in the lower temperature of 40.2 ºC ± 0.4 ºC than the temperature obtained in conventional drilling (74.9 ºC ± 0.8 ºC). In CD severe thermal tissue burns were seen and microscopic analysis revealed that injury was caused to tissues due to high drilling force while no thermal necrosis was seen in RUD.

Singh et al. (2018) [7] carried out parametric investigations during conventional and vibrational drilling to compare the results found in terms of osteonecrosis. The process parameters selected for the experimentation are rotational speed (600, 1200, 1800, 2400, and 3000 rpm), feed rate (10, 20, 30 40, and 50 mm/min), and drill point angle (60, 80, 100, 120, and 140º). The lower levels of the bone drilling parameters were suggested to avoid thermal injury during bone drilling. The largest contribution was made by rotational speed i.e.

80.53% towards the response characteristics. Histological examination outlined that vibrational drilling caused less cell damage in comparison to conventional drilling.

Alam et al. (2019) [160] performed histological analysis during vibrational drilling of bovine femur specimens. Three process parameters namely speed, vibration frequency, and feed rate at five levels. Experiments were performed with a transducer which can generate vibration up to 40 kHz and 30 μm amplitude. The results of the histological analysis revealed that higher temperature could cause damage to cell osteocytes and can lead to thermal necrosis. Grey relational statistical analysis outlined that feed rate followed by frequency and speed had a significant effect on the bone drilling process. It is further stated that thermal damaged can be reduced to a great extent using 1000 rpm speed, 30 mm/min feed, and 20 kHz frequency. The results outlined that drilling performed by the vibrating tool has the potential to increase the cells viability and bone healing than conventional drilling.

Zhang et al. (2019) [28] investigated microcracks, thermal necrosis, non-viable lacunas, and characteristics of hole edges during pig bone drilling using five different drill geometries under same process parameters. Mechanical and thermal damage was evaluated by measuring the force and temperature during drilling. It was observed that the chisel edge had a strong influence on bone damage. More microcracks were observed in the transverse direction and greater density of non-viable lacunas was reported in the longitudinal direction.

Kanaya et al. (2019) [161] performed a comparative analysis to study in-vivo thermal damage to the osteocytes during pig bone drilling with conventional and modified drill bits. Drilling parameters were thrust force 10 N and drilling speed as 800 and 1500 rpm. It was found that modified drill was able to reduce the temperature and time required to generate a hole during drilling. Further, a significant reduction in osteocytes damage was observed for the modified drill bit in comparison to the conventional drill bit.

2.6 HOSPITAL VISITS AND OBSERVATION

During the research work, multiple visits have been made at the All India Institute of Medical Science (AIIMS), New Delhi, India regarding consultation and in-depth information about the neurosurgical bone grinding operation. A research collaboration has been made with the renowned neurosurgeon Dr Deepak Agrawal (M.D. Neurosurgery). His team also abetted us with all the facilities required for the completion of this research work. Figure 2.10 depicts one of our visits to AIIMS out-patient department operation theatre.

Figure 2.10: Surgical operation theatre performing in-vivo bone grinding operation on a female skull bone (*Courtesy: All India Institute of Medical Science (AIIMS), New Delhi, India*).

The bone grinding operation was performed on the skull of a 40 years old female patient. Figure 2.11(a) shows the overhead surgical light and microscope during the on-going surgical operation. The surgical light provides necessary illumination on the grinding site for better visibility. Whereas, the surgical operating microscope provides improved vision and

magnification of the anatomy. Figure 2.11(b) shows the high-speed surgical pneumatic air pencil grinder and bone grinding tool. Figure 2.12 shows the drip irrigation which is used during removal of bone flap to decrease the temperature generated during bone grinding.

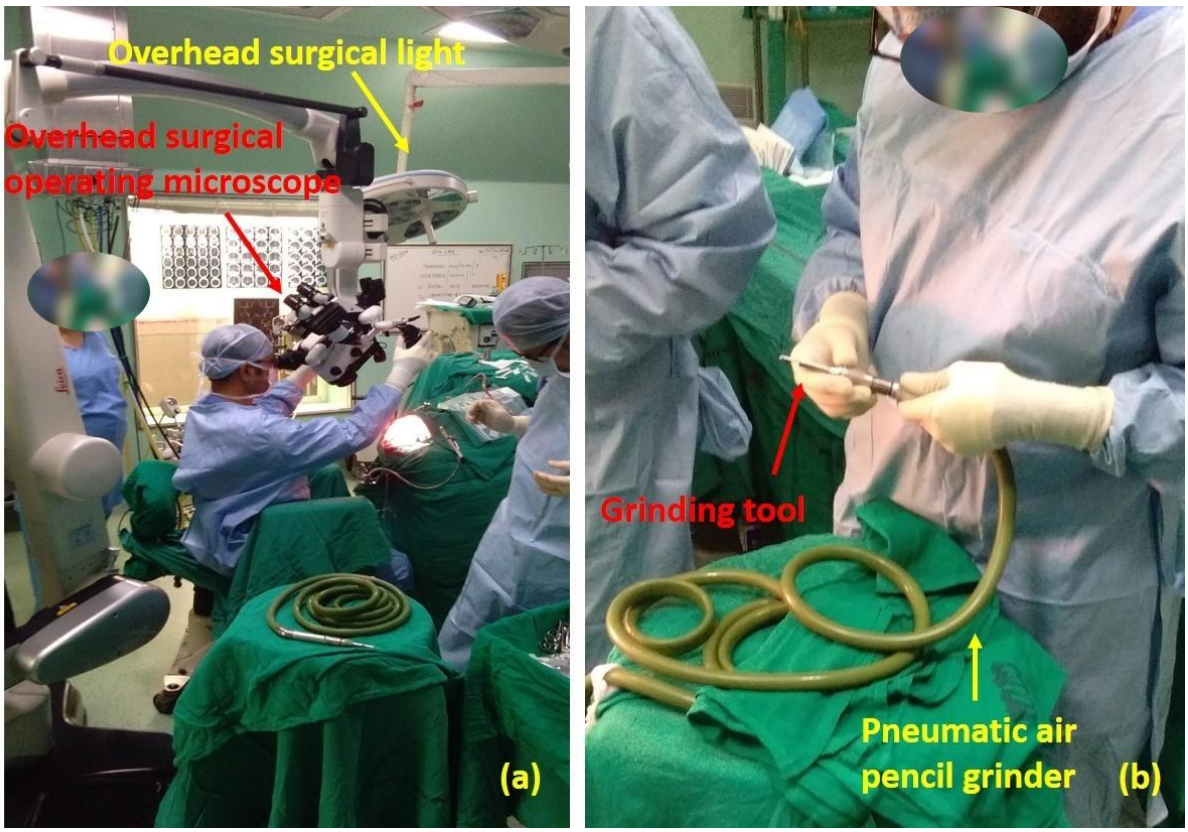

Figure 2.11: Surgical operation theatre (a) Overhead surgical light and microscope; (b) Pneumatic air pencil grinder and grinding tool (*Courtesy: All India Institute of Medical Science (AIIMS), New Delhi, India*)**.**

Figure 2.12: Drip irrigation used for removal of heat during bone grinding (*Courtesy: All India Institute of Medical Science (AIIMS), New Delhi, India*)**.**

Figure 2.13 shows a screen which provides a magnified view of the grinding site, thereby, assist in reaching the locations of the tumor. Firstly, a passage is created by removing the part of skull bone with grinding burr followed by the removal of tumor present underneath the bone.

Figure 2.13: Screen showing the enlarged view of the surgical area and dura mater (*Courtesy: All India Institute of Medical Science (AIIMS), New Delhi, India*)

2.7 RESEARCH GAPS AND ANALYSIS

Following are the research gaps which are extracted from the literature review:

- Exposing and resecting tumor lesions require extensive grinding of the bone surrounding the optic, cavernous sinus, carotid artery and branches of the trigeminal. During bone grinding, heat is generated and may damage the nerves, hence it is imperative to preserve these critical nerves during the resection of a tumor during neurosurgical operations. Such thermal injury is of particular concern for neurosurgeons due to lack of knowledge on heat propagation to the nerve during bone grinding
- Clinical research and in-vivo surgical operation revealed that heat-induced thermogenesis during neurosurgical bone grinding can cause severe consequences such as blood coagulation, optic nerve damage, loss of facial muscles control, and osteonecrosis. Hence, an alternative way is required to limit the temperature below the threshold value to avoid thermal injuries.
- Based on the literature review, it was analyzed that **bone drilling** has been investigated a lot but few studies are available for **bone grinding**. The material removal mechanism of drilling and grinding is quite different; hence bone grinding should be explored for osteotomy.
- At present, neurosurgeons use the hand-held grinding device and process parameters are varied as per their need without considering the effect on temperature rise during surgical grinding. Consequently, a set of controlled optimized parameters is required for especially for novice neurosurgeons, considering the heat-induced consequences.
- As discussed in the literature, work done by different investigators using a rotary ultrasonic machining process reflects that RUM has huge potential in mitigating the

temperature rise during the different machining operation. Keeping in mind the benefits of RUM, this process can be used for grinding of bone during a neurosurgical operation.

- The thorough analysis of the literature revealed that the effect of different drill bits has been investigated during bone drilling for orthopaedic operations. But no study has been reported to determine the effect of different grinding burrs during neurosurgical operations.
- A lot of studies are available which shows the comparison of conventional drilling and rotary ultrasonic drilling of bone. On the flip side, no research study has been carried for a comparative analysis of conventional bone grinding and rotary ultrasonic neurosurgical bone grinding.
- Tool wear plays a significant role in controlling the temperature, surface roughness and crack propagation during machining of any material. The tool wear in terms of burr loading, dislodging of abrasives, and microcracks have never been reported for bone grinding.
- Different analytical models were being developed for the prediction of force, surface roughness, vibration amplitude, material removal, wheel topography and loading with the help of different assumptions, functions and approaches. Till now, analytical models developed for rotary ultrasonic actuation are still scarce and further improved models are required especially considering the thermal trauma owing to the elevated temperature. In this direction, thermal dose models (such as CEM43℃) could play a significant role in determining the degree of burn caused owing to the rise in temperature during bone grinding.

The overall comparison of bone machining with conventional and non-conventional approach considering different problems accompanying bone is shown in Figure 2.14. Further, the

percentage of different materials machined with RUM and process parameters investigated are represented in Figure 2.15 and 2.16.

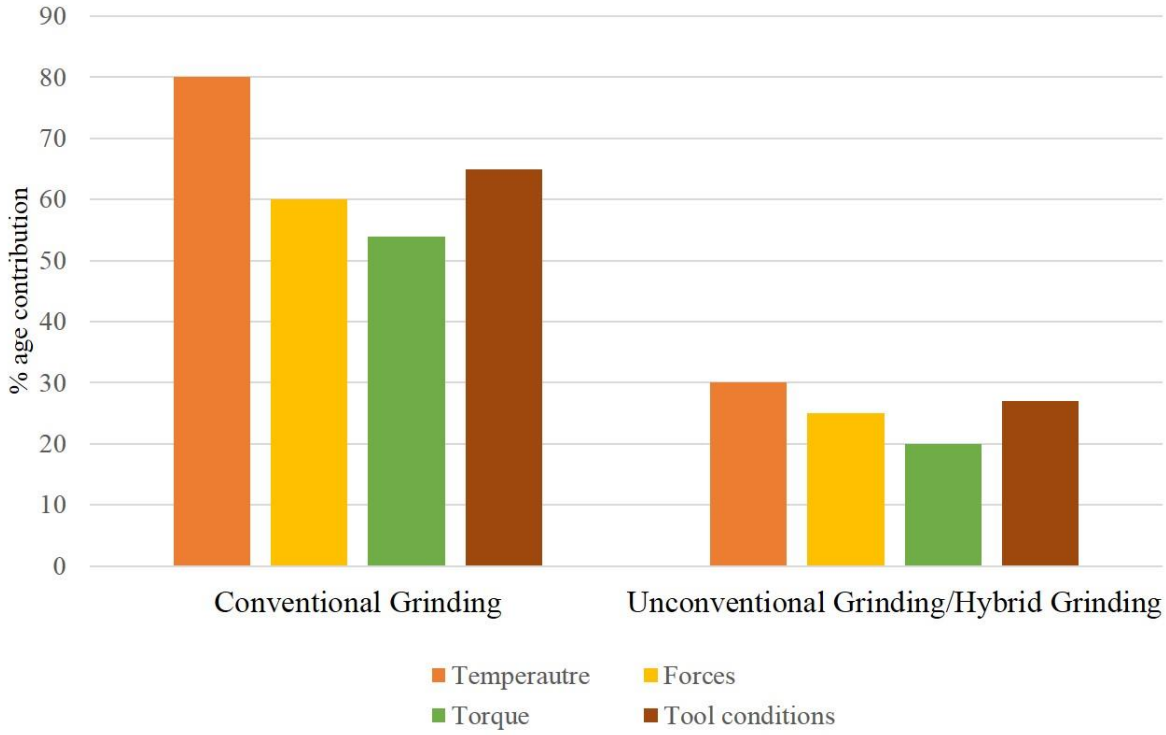

Figure 2.14: Comparison of the percentage contribution of different output characteristics explored in conventional and unconventional grinding.

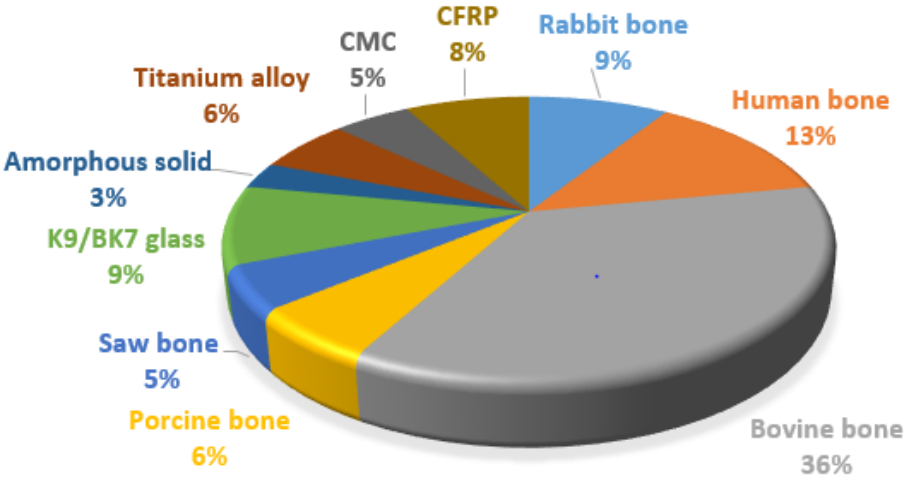

Figure 2.15: Different work materials considered in RUM.

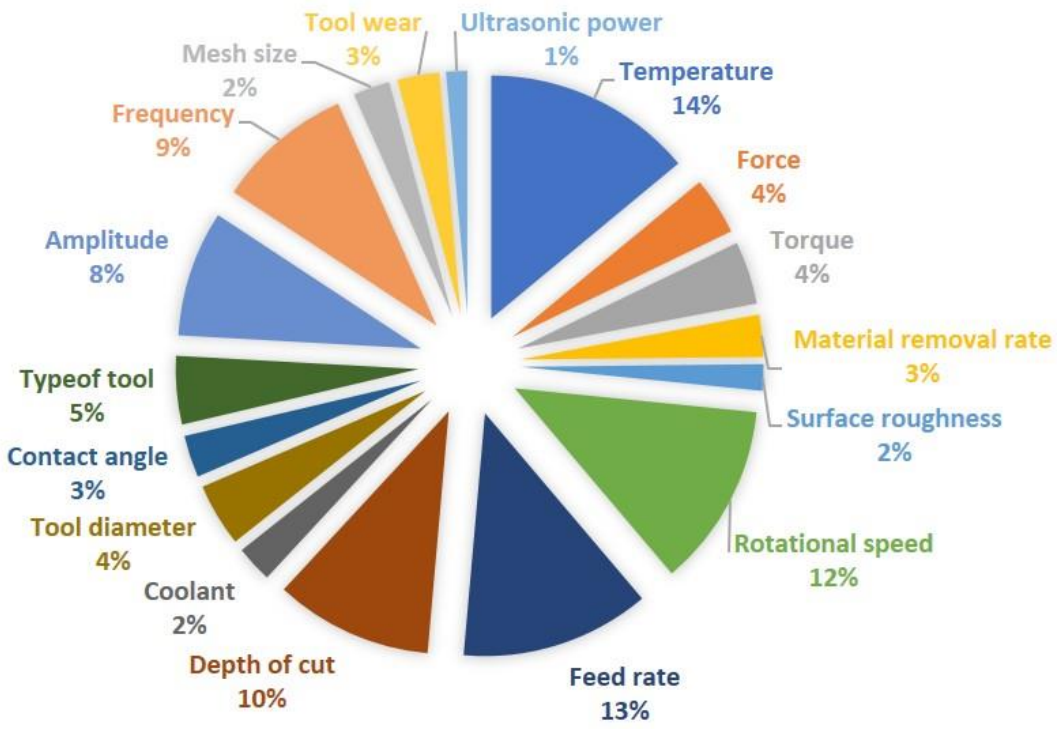

Figure 2.16: Percentage of different process parameters considered in RUM.

At present, a rotating burr is used in surgical operations without ultrasonic actuation. This procedure may not decrease the temperature to a safe level. In this direction, the ultrasonically actuated burr may prevent osteonecrosis during bone grinding. The key advantages of ultrasonic actuation being the selective cutting of hard tissue (bone) and preservation of the soft neural tissue, less vibration and noise, absence of thermal trauma in adjacent, reduction in bleeding, better healing and good access of the operative field. Hence above-stated literature and exceptional advantages of ultrasonic gives us a great possibility for **Experimental Investigation of Neurosurgical Rotary Ultrasonic Bone Grinding.**

2.8 RESEARCH OBJECTIVES

The major objectives of the proposal are:

1. To investigate and analyze the influence of the various process parameters of rotary ultrasonic neurosurgical grinding (RUNG) on thermal characteristics/aspect and thus process optimization.
2. To study surface morphology of the grinding tool, burr loading and cracks on the bone during the grinding process.
3. To explore the scientific basis of the process and hence analytical modelling of the rotary ultrasonic neurosurgical grinding (RUNG) process.

2.9 METHODOLOGY

The flowchart shows the step by step methodology of performing the proposed research work.

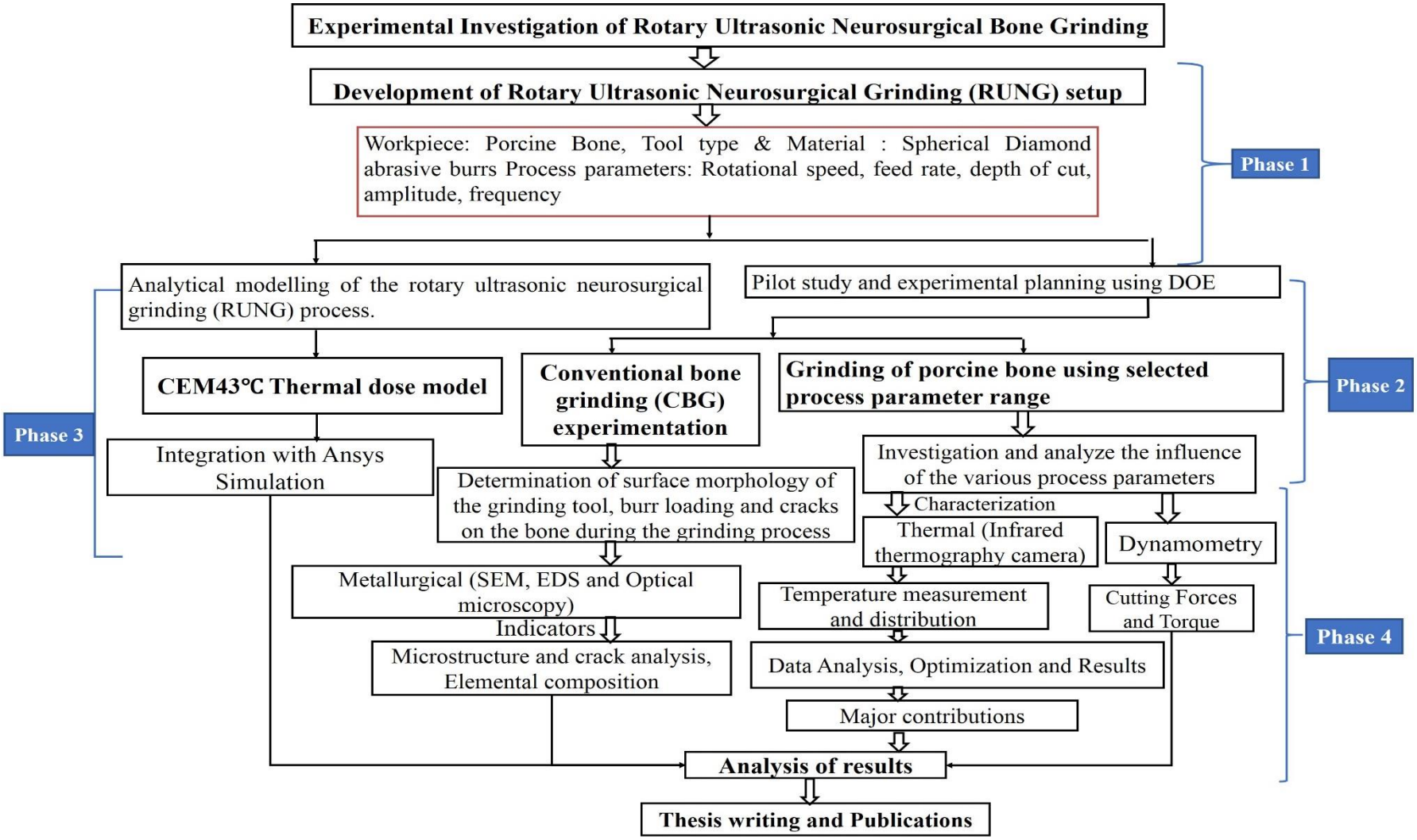

2.10 SUMMARY

Most of the research carried out by previous researchers were focused on using a high-speed drill bit for bone drilling during orthopaedic surgical operations. However, drilling cannot be used during the treatment of benign and cancerous brain tumours because it can cause severe damage to the underlying dura-mater within the brain. Therefore, a grinding burr is used to remove the skull bone in the layer-by-layer manner instead of the bulk material removal from the surface of the bone. It has been observed that elevated levels of the temperature can cause thermogenesis and osteonecrosis owing to the generation of the heat during bone grinding. In this direction, rotary ultrasonic bone grinding may assist in mitigating the rise in temperature during bone grinding. The importance of thermal dose models has also been highlighted for evaluating the degree of thermal burn. Additionally, it has been noticed that rotary ultrasonic machining significantly reduces the machining time owing to the combined material removal mechanism of conventional and vibrational machining. Therefore, reduced machining time will thus further promote better healing and reduction in the post-operative recovery time.

CHAPTER 3: GRINDING SETUP AND EXPERIMENTATION

3.1 SELECTION OF BONE

The selection of the bone in the present study is a challenging task since human bone is not easily available for the experimentation. It was revealed that the properties of animal and human bone resemble a high degree of resemblance [103,162–166]. Due to which many researchers used animal bone for their experimental work. The thermo-mechanical properties of the bone have a significant influence on the behaviour of the response characteristics towards the machining process. To fulfil the changing functional demands, the bone optimally adapts itself with continuous remodelling. It has been observed that properties like porosity, architecture, collagen fibre orientation, fatigue damage etc. strongly affects the mechanical properties of the bone. These properties have a strong influence on the outcome during the grinding of bone. The properties of human bone vary with age, group, people, and size. Human skull bone consists of three layers in which outer layers are known as cortical bone and sandwiched inner portion known as spongy or cancellous bone. The average thickness of the skull bone lies in the range of 4-7 mm [45]. In the past studies [7,8,93,103,106], researchers have used the same pig bone for experimentation since its properties closely resemble the human bone's properties as shown in Table 3.1.

Table 3.1. Thermo-mechanical properties for the animal and human bone [7,9–15,167,168].

Property	**Unit**	**Animal Bone**	**Human Bone**
Young's modulus	GPa	19.4 ± 5.8	18.6 ± 3.5
Ultimate stress	MPa	129 ± 16.5	132 ± 12.8
Tensile strength	MPa	113 ± 2.1	124 ± 1.1
Compressive strength	MPa	147 ± 1.1	170 ± 4.3
Thermal conductivity	W/mK	0.64 ± 0.04	0.68 ± 0.01
Density	kg/m^3	1950-2100	1800-2000
Poisson's ratio	−	0.34 ± 0.09	0.4
Emissivity	−	≈ 0.95	0.96 ± 0.01
Specific heat	J/KgK	1260	1140 – 2370

Therefore, in the present study, skull bone harvested from the dead pig is used for the experimentation. Moreover, ethical concerns are associated with human bone. The animal bone used in the present study is collected from local butcher shop which supplies pig meat for food industry applications. No animal was especially sacrificed for completing present experimentation. The experiments were immediately performed within several hours of the slaughter.

3.2 PREPARATION OF BONE SPECIMEN

The bones were acquired from the two different locations of the porcine. The preliminary experimentation was carried out porcine femur bone as shown in Figure 3.1. The femur bone consists of different parts namely proximal epiphysis, mid diaphysis, and distal epiphysis. The experiments were performed on the cortical part of the bone having high density. The ends of the bone were cut and preliminary trials have been carried out on mid diaphysis section of the bone. The bone marrow inside the cavity has been removed and bone specimens were then cleaned to remove flesh present on the bone. However, the final experiments were performed on the skull bone specimens as shown in Figure 3.2.

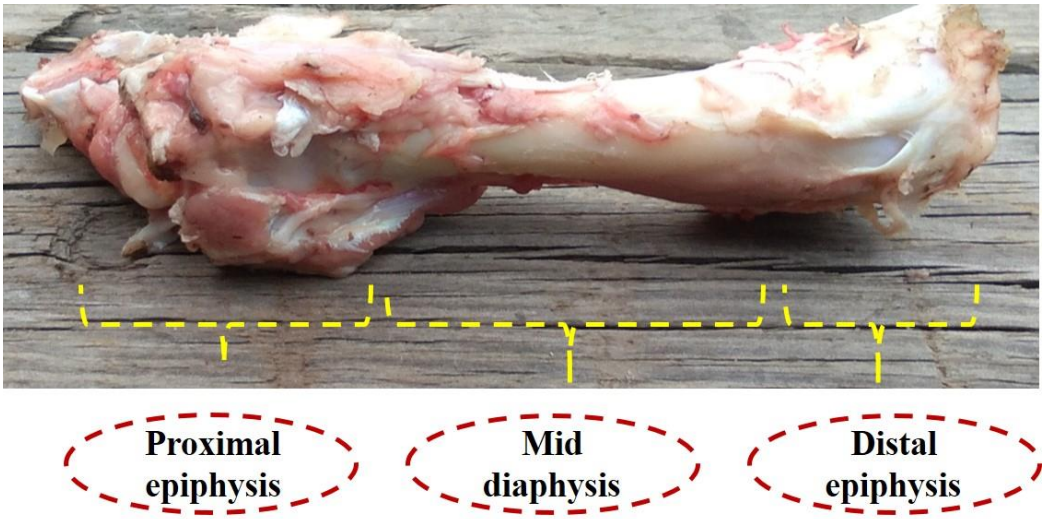

Figure 3.1: Porcine femur bone for preliminary experimentation.

Figure 3.2: Porcine skull bone specimens for final experimentation.

The porcine is 10-12 months old which reflects the properties of the human age group of 20-45 years. This age group is mostly free from any kind of disease. The experiments were immediately performed to avoid loss in the physical properties of the bone.

3.3 TOOLING

The experimentation was carried out using a surgical spherical grinding burr. The diamond abrasive burr was used since a diamond is composed of carbon and biologically does not harm the body tissues. The tool aided for the experimentation is a round diamond burr of 4 mm diameter as shown in Figure 3.3. The diamond abrasive grits of 200/300 ANSI mesh size were electroplated over the lateral and end face of the burr.

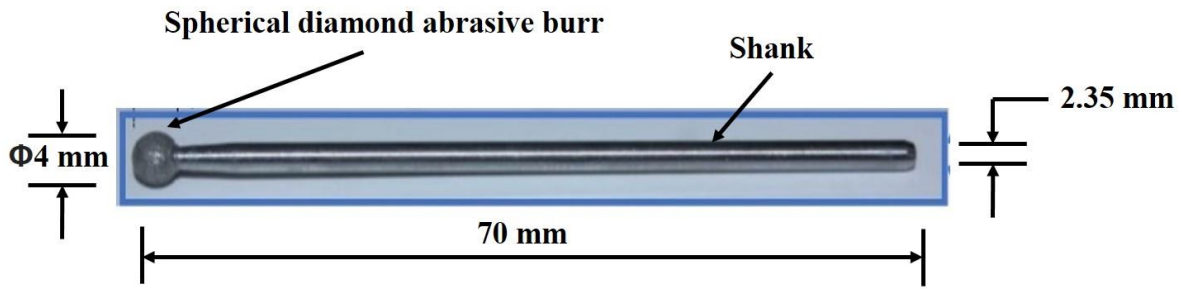

Figure 3.3: Spherical diamond abrasive burr for experimentation.

As per the discussion with neurosurgeons, an attempt has also been made to investigate the four different shapes of tools during bone grinding as given in Table 3.2. The different shaped surgical grinding tools used in the present investigation were spherical tool, convex tool, cylindrical tool and tree-shape tool as shown in Figure 3.4. The total length of the tool is 60 mm and the diameter of the shank is 6 mm. Authors tried to maintain the approximately same burr dimensions. The small variation in the diameter of all the four selected tools is due to the market constraints and availability of tools.

Table 3.2. Specifications details of all diamond-impregnated abrasive tools.

S. no.	Tool name	Type	Tool shank material	Abrasive type	Abrasive mesh size	Burr dimensions (mm)	Abrasive coated technique
1	Spherical tool (T1)	Solid	EN 31	Diamond	46	Dia.: 9.98	Vacuum brazed
2	Convex tool (T2)	Solid	EN 31	Diamond	46	Dia.: 9.74	Vacuum brazed
3	Cylindrical tool (T3)	Solid	EN 31	Diamond	46	Dia.: 10.1	Vacuum brazed
4	Tree-shape tool (T4)	Solid	EN 31	Diamond	46	Dia.: 9.56	Vacuum brazed

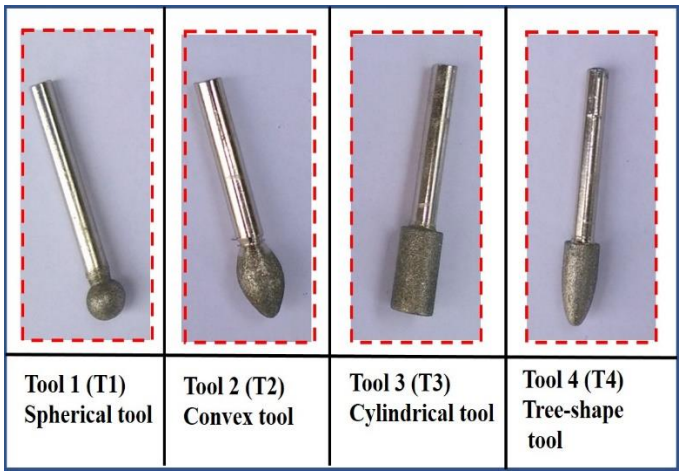

Figure 3.4: Different shaped surgical grinding burrs: (a) spherical tool, (b) convex tool, (c) cylindrical tool, (d) tree-shaped tool.

3.4 ROTARY ULTRASONIC BONE GRINDING SETUP

3.4.1 Preliminary Experimental Setup

To investigate the effect of ultrasonic actuation on temperature rise during bone grinding, an in-house experimental setup was designed and fabricated. A 3-Axis CNC vertical milling centre was used for experimentation to give tool motion automatically in different directions. The illustration of the developed setup has been shown in Figure 3.5. The complete experimental setup: (a) CNC machine with the spindle, tool holder, and abrasive tool, (b) control panel (c) horn assembly, (d) fixture, (e) infrared thermography, (f) analysis and reporting tool. The process parameters were controlled by the controller unit of the machine. A fixture was also been developed to precisely hold the bone without any disturbance during machining. The generator produces a vibration frequency of 20 kHz which fascinates the axial vibrations to the tool.

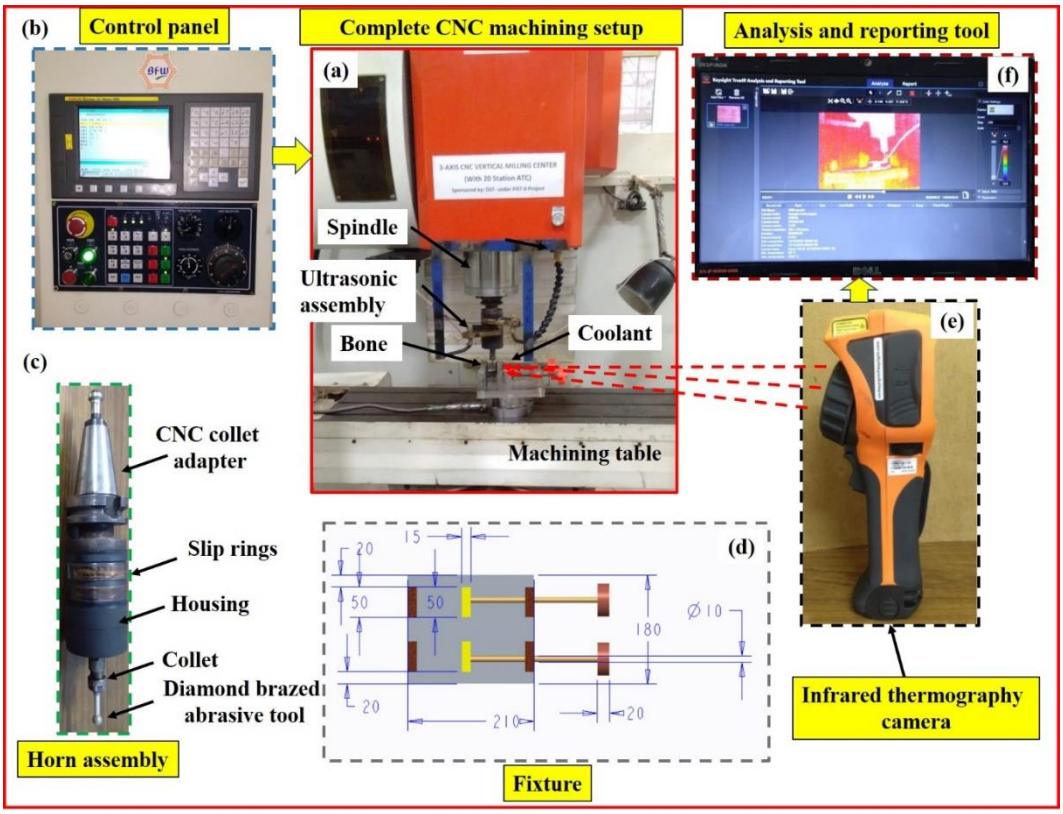

Figure 3.5: In-house developed experimental setup used for the preliminary experimentation.

The electrical energy produced by the generator is supplied to the piezoelectric transducer through slip rings and carbon brushes which is further converted into the mechanical energy (i.e. vibrations). These mechanical vibrations travel through the horn and get amplified before reaching the burr. The saline irrigation was used for cooling purpose. The specimens were clamped on a fixture to avoid any unwanted movement during grinding.

The limitation of this experimental setup was that the maximum permissible rotational speed is 5000 rpm. However, as per the discussion with neurosurgeons, it was realized that during bone grinding, they use high-speed pneumatic bone grinding setup in which tool rotates at very high rpm up to the rotational speed of 60,000rpm. Therefore, new experimental setup is developed for the same purpose which has been discussed under subsequent sub-section.

3.4.2 Final Pneumatic Experimental Setup

A novel in-house experimental setup was developed for experimentation which is used in conjunction with CNC vertical milling machine. The schematic representation of the experimental setup has been shown in Figure 3.6. The experimental setup is capable of producing ultrasonic vibration up to 40 kHz with a piezoelectric transducer. The experiments were performed as per designed matrix.

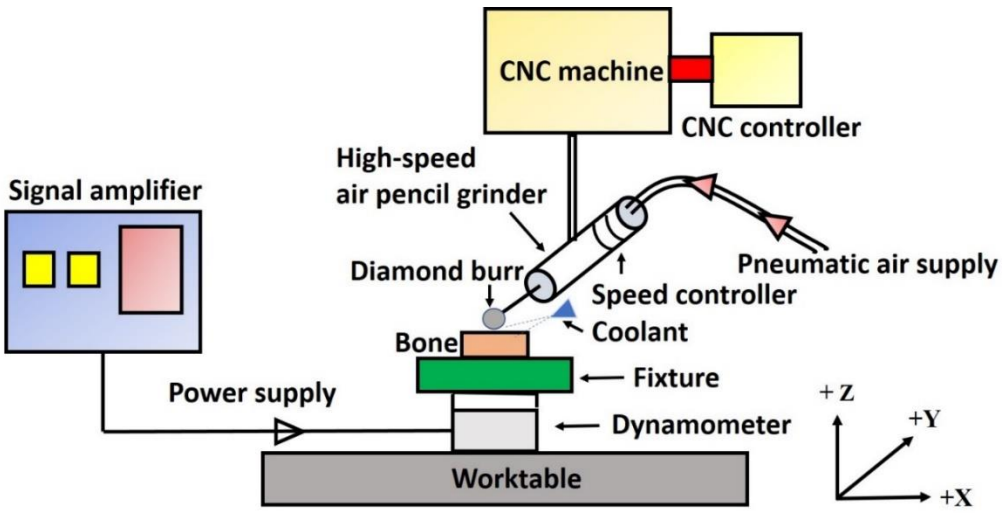

Figure 3.6: In-house developed bone grinding experimental setup.

Figure 3.7 shows the experimental setup and devices used for completing the experimentation. The complete experimental setup consists of (a) rotary ultrasonic bone grinding setup (RUNG) mounted on CNC machine along with high-speed pneumatic air pencil grinder (b) groove length on a bone specimen (c) infrared thermal camera (d) True-IR analysis and reporting tool (e) ultrasonic transducer (f) ultrasonic generator box (g) spherical diamond impregnated grinding burr. Three different frequencies transducers were used as per the designed matrix to actuate the bone using ultrasonic vibrations. The ultrasonic transducer was connected to the ultrasonic generator box which ensures sufficient electric supply for the working of the transducer.

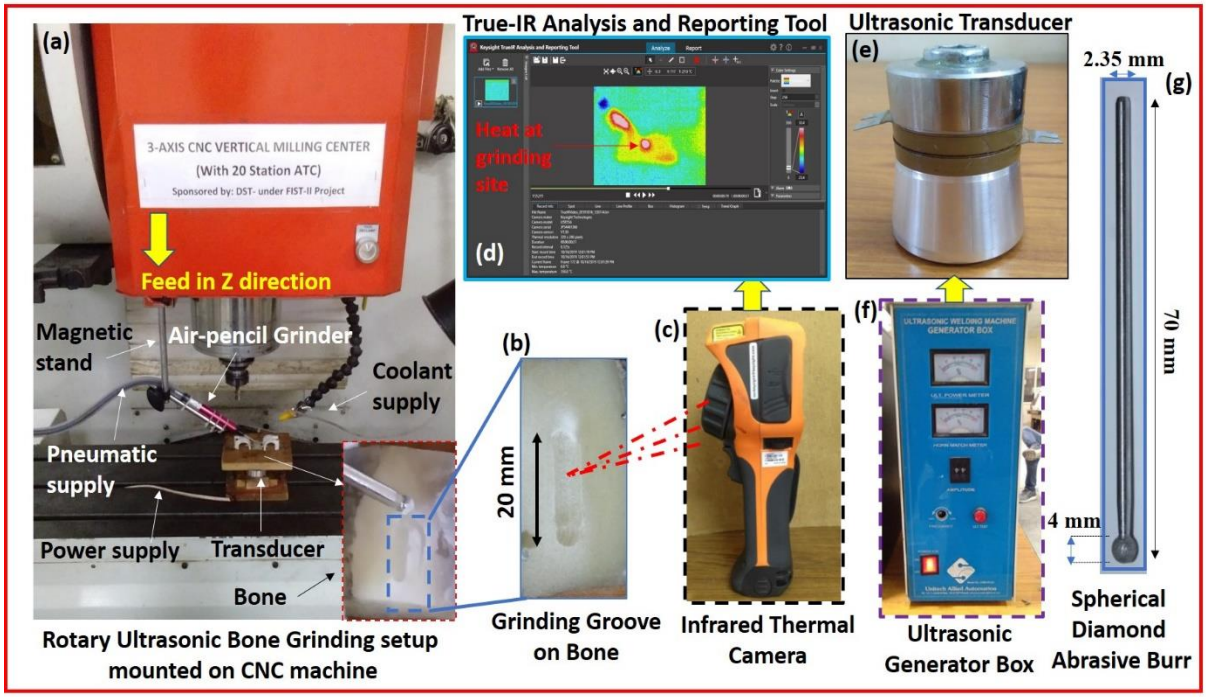

Figure 3.7: The complete rotary ultrasonic bone grinding experimental setup.

Further, the feed rate to the burr and bone is provided using a computer-controlled mechanism. A sterile solution (coolant) was used to irrigate the grinding site; thereby, removal of bone chips and heat from the grinding zone. A continuous pneumatic supply is supplied to the air pencil grinder to achieve high-speed of the grinding burr. The high-speed air pencil grinder was inclined at an angle of 30° as used in osteotomy during removal of a

bone flap from a skull bone. Since the mechanics of cutting remains the same, therefore, whole bone grinding operation mimics the actual surgical conditions.

3.5 EXPERIMENTAL DESIGN

A broad range of parameters and their levels were selected for trial runs and eventually, the most significant parameters with their three levels have been decided accordingly. Also, owing to machining constraints, market availability constraint, feasibility in actual surgical conditions and based on previous literature available in this domain [8,103,159,169–175], the present parameters and their levels were decided as shown in Table 3.3.

Table 3.3. Bone grinding parameters and their levels with response characteristics for RUNG.

Parameters	**Level 1**	**Level 2**	**Level 3**	**Response characteristics**
Rotational speed (rpm)	35000	45000	55000	1. Temperature 2. Tissue damage 3. Depth of thermogenesis and osteonecrosis
Feed rate (mm/min)	20	40	60	
Ultrasonic frequency (kHz)	20	28	40	
Constant parameters				
Parameter	**Unit**		**Value/Working range**	
Vibrational amplitude	µm		15	
Length of pass	mm		20	
Depth of cut	mm		0.5	
Coolant flow rate	cc/min		20	

The second set of experimentation was carried out for conventional bone grinding experiments. The levels of rotational speed, feed rate, and frequency of vibration selected for the experimentation is shown in Table 3.4.

Table 3.4. Process parameters and levels of bone grinding experiments for CBG experiments.

Parameters (Unit)	Level 1	Level 2	Level 3	**Response characteristics**
Rotational speed, (rpm)	35000	45000	55000	1. Cutting forces 2. Torque
Feed rate, (mm/min)	20	40	60	

Depth of cut, (mm)	0.50	0.75	1.00	

A three-level full factorial 3^3 design has been used to investigate all possible combinations of the process variables. The levels are generally referred as -1 (low vale), 0 (intermediate value), 1 (high value). A full factorial design facilitates to study the possible model curvature in the criterion variable during analysis. The pictorial representation of the full factorial design is shown in Figure 3.8. The corresponding sets of coded and un-coded parametric combinations are tabulated in Table 3.5.

In total, 81 experiments were carried out to complete the present study with 27 unique experiments. The effect of these grinding parameters was analyzed in terms of temperature and the percentage of viable cells using statistical and histopathological analysis. A constant depth of cut of 0.5 mm and 20 mm length of the pass is maintained for all experiments.

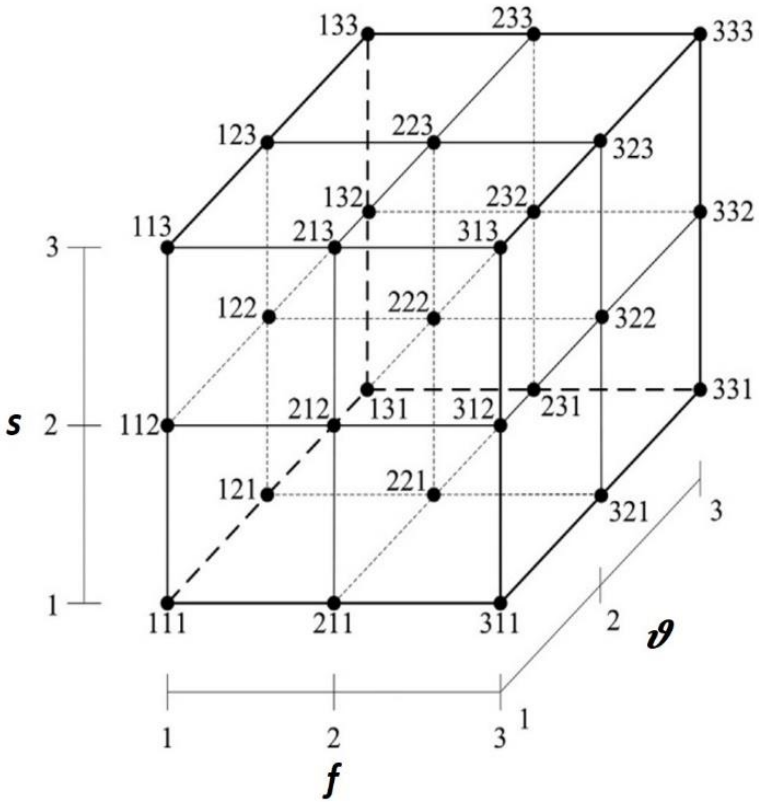

Figure 3.8: Pictorial representation of 3^3 full-factorial experimental design [176]

Table 3.5. A full factorial design in its coded and un-coded notation for RUNG experiments.

Std. Order	Run order	Coded notation			Un-coded notation		
		Rotational speed (rpm)	Feed rate (mm/min)	Ultrasonic frequency (kHz)	Rotational speed (rpm)	Feed rate (mm/min)	Ultrasonic frequency (kHz)
4	1	-1	0	-1	35000	40	20
23	2	1	0	0	55000	40	28
24	3	1	0	1	55000	40	40
7	4	-1	1	-1	35000	60	20
15	5	0	0	1	45000	40	40
6	6	-1	0	1	35000	40	40
10	7	0	-1	-1	45000	20	20
19	8	1	-1	-1	55000	20	20
3	9	-1	-1	1	35000	20	40
2	10	-1	-1	0	35000	20	28
12	11	0	-1	1	45000	20	40
11	12	0	-1	0	45000	20	28
14	13	0	0	0	45000	40	28
20	14	1	-1	0	55000	20	28
16	15	0	1	-1	45000	60	20
9	16	-1	1	1	35000	60	40
21	17	1	-1	1	55000	20	40
5	18	-1	0	0	35000	40	28
27	19	1	1	1	55000	60	40
13	20	0	0	-1	45000	40	20
26	21	1	1	0	55000	60	28
17	22	0	1	0	45000	60	28
8	23	-1	1	0	35000	60	28
25	24	1	1	-1	55000	60	20
18	25	0	1	1	45000	60	40
22	26	1	0	-1	55000	40	20
1	27	-1	-1	-1	35000	20	20

3.6 BONE GRINDING PROCEDURE

The sequential manner in which experimentation was carried out is shown in Figure 3.9. Firstly, the bone specimens were prepared then air pencil grinder and coolant unit are installed on the CNC machine. The temperature generated during the bone grinding has been

measured with the infrared thermography while the cutting forces were measured using the dynamometer. The dynamometer was installed beneath the bone to measure the grinding forces during CBG. The dynamometer was further connected to the charge amplifier to amplify the signal's output. Whereas, the infrared camera is mounted at a certain distance from the grinding site. A fixture was designed to hold the bone samples firmly.

A high-speed air pencil grinder was used to rotate the spherical diamond abrasives grinding burr. High-pressure air supply (up to 90 bar) is supplied to rotate the grinding burr up to a speed of 55k rpm. The process parameters were varied from the control panel of automatic CNC machine (VMC, Chandra+, Bharat Fritz Werner Ltd.) as per the designed set of orthogonal array design. The whole ultrasonic assembly was mounted on the CNC machine to provide feed-in X, Y and Z direction.

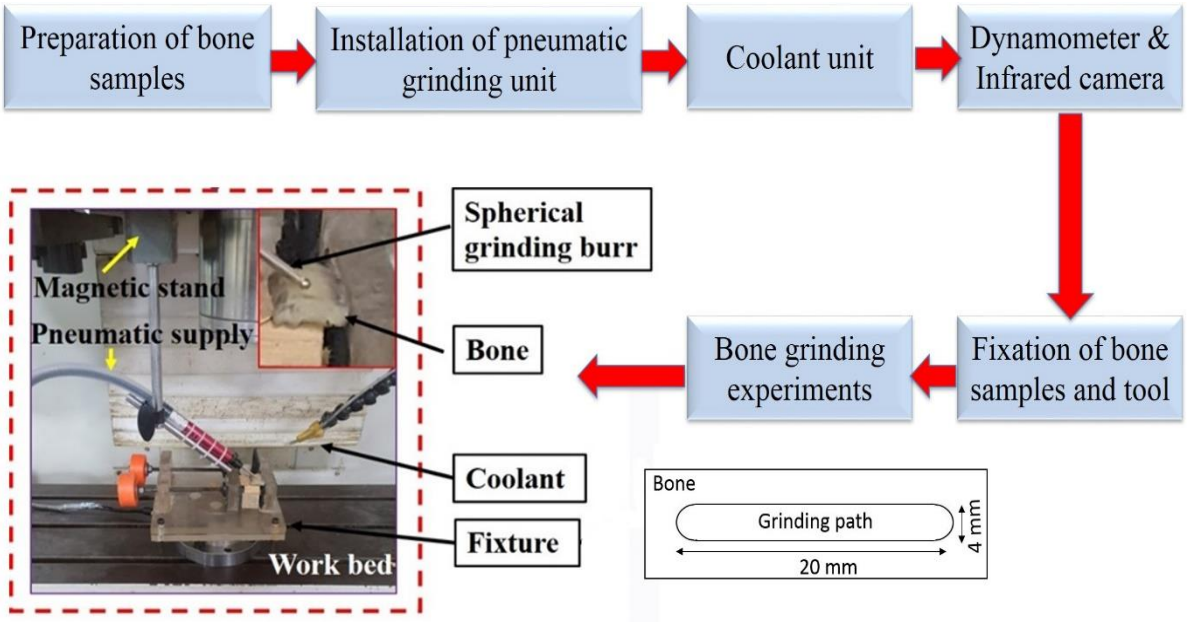

Figure 3.9: Sequential manner followed in performing bone grinding experiments.

A signal amplifier was connected to the dynamometer during experimentation. The rotational speed is controlled via the speed controller knob on the pneumatic air pencil grinder. A length 20 mm pass was being followed on the bone. The pneumatic air supply was turned ON to run

the grinding tool at high-speed. The grinding burr was inclined at an angle of 30º to the bone specimen as shown in Figure 3.10.

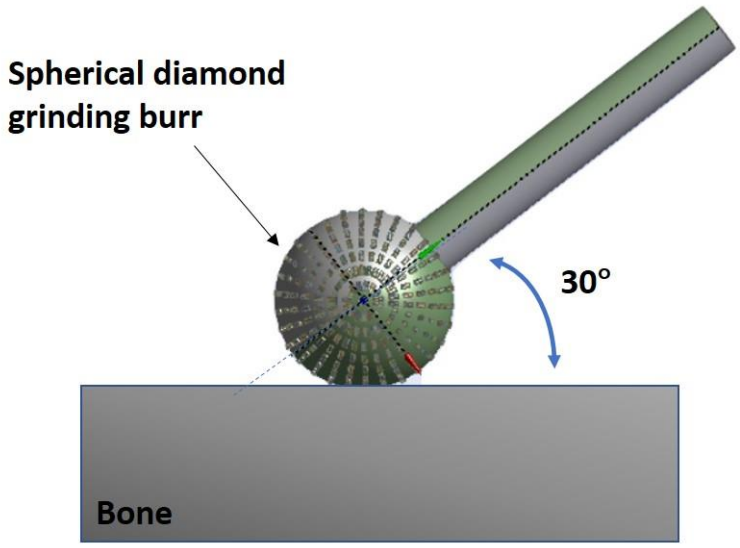

Figure 3.10: Schematic representation of grinding burr and bone.

The whole grinding area was flooded with a sterile solution (coolant) to mimic in-vivo bone grinding conditions at ambient temperature. The normal saline solution used in the present study has 9 gm of salt per litre of water i.e. 0.9% sodium chloride (NaCl) in 1L of H_2O. The observed flow rate is 20 cc/min maintained constant throughout the experimentation. Bone specimens were placed on the top of an ultrasonic transducer which would cause the bone to vibrate instead of grinding burr. Simultaneously, the CNC machine was used to provide feed to the grinding burr in +Y and -Z direction. As the grinding continues, the material was removed from the surface of the bone in the form of bone chips. Due to the abrasion between burr and bone, heat was generated which escalates the temperature at the grinding site. The temperature on the surface of bone was measured using the infeed thermography camera.

The pictorial representation of the RUNG and CBG process has been shown in Figure 3.11. In the case of RUNG, grinding burr is rotated with pneumatic supply and vibrations were

supplied to the bone, as evidently in Figure 3.11(a). There exist continuous engagement and disengagement of the tool and bone. The continuous engagement and disengagement of the tool and bone was achieved using an ultrasonic transducer which is placed beneath the bone.

The terminals of the ultrasonic generator box was connected to the ultrasonic transducer for continuous power supply. The ultrasonic transducer actuates the bone at given frequency and amplitude which caused momentarily engagement of the tool with bone. The amplitude of vibration was kept constant at 15 µm and frequency is variable which is at three levels i.e. 20, 28, and 40 kHz. The piezoelectric ultrasonic transducers with varying frequency of 20 kHz, 28 kHz, and 40 kHz are used during the experimentation. The amplitude of vibration was kept at 15 µm and transducers are connected to the ultrasonic generator box. The temperature generated during bone grinding was continuously monitored with the help of infrared thermography.

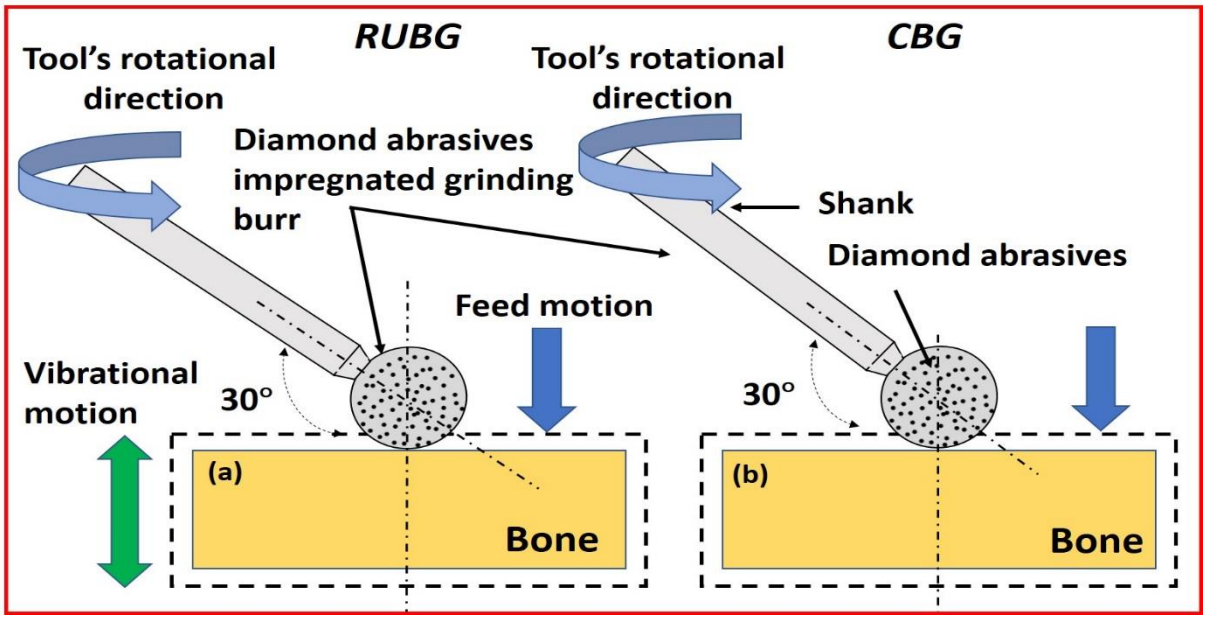

Figure 3.11: Pictorial representation of (a) rotary ultrasonic bone grinding and (b) conventional bone grinding.

During infrared thermography, the 8 thermograms are produced in 1 second with a recording interval of 0.125 seconds which means 8 different temperature readings within 1 second. For

feed rate of 20 mm/min, the machining time is 60 seconds (length of the pass is 20 mm) i.e. 480 readings of temperature during 1 trial only. Therefore, authors have decided to average the temperature readings for each trial to analyze the mean maximum temperature during the machining operation. Consecutively, the spatial and temporal distribution of the temperature and depth of thermogenesis and osteonecrosis has been measured using finite element simulation analysis. It should be noted that for each set of parametric combination, three consecutive trials have been performed and their average has been presented on the manuscript. In total, 81 experiments were carried out and 27 unique cases. Furthermore, the statistical analysis i.e. analysis of variance (ANOVA) was carried out at a 95% confidence interval. The optimization toolbox has been used in MATLAB to minimize the change in temperature with minimum deviation. The cutting forces developed during grinding were quantitatively measured using a dynamometer (2852A-02, Kistler Group, Switzerland). Subsequently, bone samples are characterized using surface electron microscopy to observe the micro-cracks over the surface of a bone. The thermal damage to the bone owing to the heat generation has been evaluated using histopathology.

In the case of CBG, grinding burr was rotated at prerequisite rotational speed and bone is kept stationary without supplying vibration to it. Since the neurosurgeons use conventional bone grinding during craniotomy, therefore, the cutting forces produced during the bone grinding have been measured for CBG experiments. Once all experiments are executed with RUNG further experiments will be performed with conventional grinding. For comparative analysis, CBG experiments are carried out with a set of optimized parameters which caused maximum and minimum temperature during bone grinding. Subsequently, confirmation experiments have been performed at optimized conditions.

3.7 QUANTITATIVE ANALYSIS OF BONE ADHESION AND TOOL WEAR

It is expected that burr loading and burr wear affects the cutting ability of the abrasives and friction at burr-bone interface which eventually affects the temperature produced during bone grinding. To address this concern, quantification analysis has been made for different shape of the grinding burrs. As per the suggestions from neurosurgeons, a quantitative analysis of bone adhesion and tool wear has been carried out for different shapes of the grinding burrs. To evaluate the tool wear after conventional grinding, the weight (in gm) of the four tools was measured by using a high-precision digital weighing balance (XPE Analytical Balance, METTLER TOLEDO, USA). The weight of the tool was measured before and after the machining of porcine bone. A used tool includes the dislodging and wears off abrasives. Simultaneously, the bone debris also adheres to the tool. Hence, to evaluate the amount of dislodging/wear off particles and the amount of bone adhere to the tool, a "weight loss" method is adopted.

It has been observed that the removal of one debris from the burr by using conventional methods is not possible due to the high chemical and mechanical affinity of bone. So, to estimate the weight of the bone, an ultrasonic bath sonicator (Sarthak Scientific Services, India) was used to remove the bone debris adhered over the burr as shown in Figure 3.12(a). Each sample was kept in an ultrasonic bath sonicator for 15 mins continuously and repeated three times to ensure complete removal of bone debris attached to the burr face. The four samples were observed before and after sonication and weigh in two different conditions. Initially, water was pure (before sonication) but after sonication water gets contaminated with bone particles which can be seen in Figure 3.12(b). Afterwards, the weight of the abrasives removed over the burr is calculated by subtracting the weight of the tool after sonication from the initial weight of the tool.

Let,

W_i = Initial weight of the tool (gram)

W_{ab} = weight of the dislodge abrasives (gram)

W_b = weight of adhered bone debris (gram)

W_{f1} = Final weight of the tool before sonication = $W_i - W_{ab} + W_b$ …….*eq. 3.1*

<u>To evaluate 'W_b'</u>

W_w = Weight of pure water

W_c = Weight of contaminated water = $W_w + W_b$

Therefore, $W_b = W_c - W_w$

Once W_b is evaluated, W_{ab} can be found by subtracting the W_b amount from W_{f1}.

Hence, $W_{f2} = W_{f1} - W_b$ ---------- *eq. 3.2*

Where W_{f2} is the weight of the tool after sonication.

From (1) & (2)

$W_{f2} = W_i - W_{ab}$

OR $W_{ab} = W_i - W_{f2}$ (as $W_i > W_{f2}$ always)

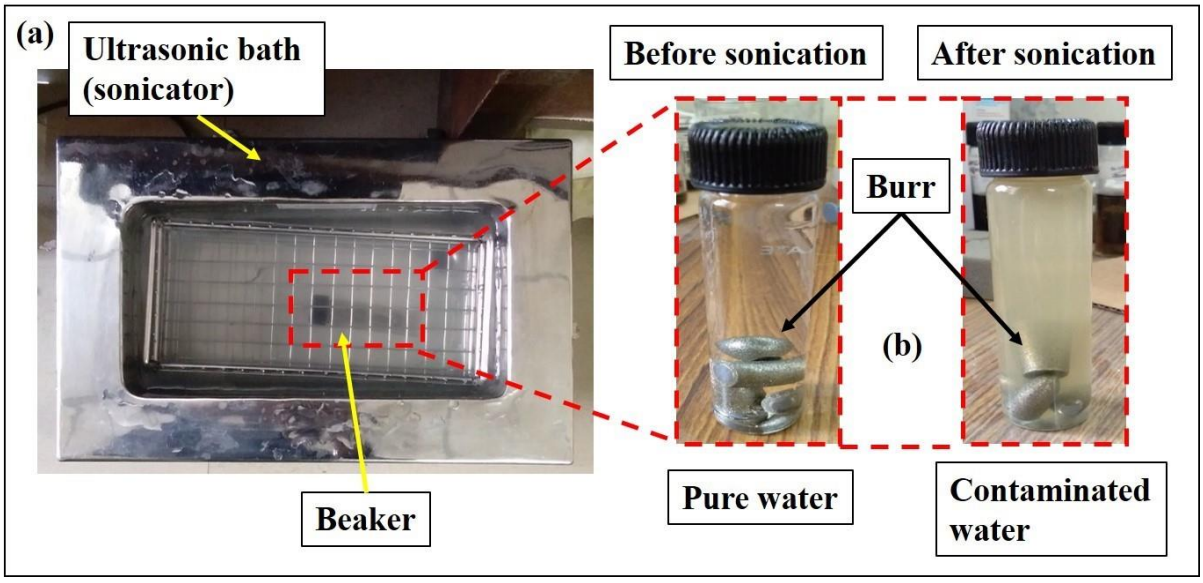

Figure 3.12: Ultrasonic bath: (a) burrs immersed in a sonicator for 45 min of immersion period and (b) comparison of water quality before and after sonication.

3.8 CHARACTERIZATION TECHNIQUES

The characterization techniques used in the thesis work for determining the parametric effect on the different response characteristics have been shown in Table 3.6.

Table 3.6. Characterization methods used during the experimentation.

S. No.	Characterization/Measurement method	Output
1	Infrared thermography	Temperature
2	Dynamometry	Cutting forces
3	Digital weighing machine	Tool wear and burr loading
4	Histopathology	Cell's damage
5	Surface electron microscopy/Optical microscope	Surface morphology
6	Energy dispersive spectroscopy	Elemental composition
7	Thermal dose model	Thermal tissue injury
8	Simulation	Depth of thermogenesis and osteonecrosis

The devices used for measuring temperature and cutting forces during bone grinding has been shown in Figure 3.13. The temperature generated during bone grinding was measured using

the infrared thermography. Generally, there are two methods of measuring the temperature rise during bone grinding which are “Thermocouple method” and “Infrared thermography”. In the first method, thermocouples were used to measure the temperature at the machining site by placing it at a certain distance beneath the machining zone. In past studies, thermocouples have been used during in-vitro studies [19,31,177–179]. In this method, firstly, holes were drilled near the grinding site and then thermocouples were inserted within the holes. However, in actual in-vivo surgical operation, it is not feasible to drill the holes in the patient’s skull before bone grinding. Furthermore, thermocouples were inserted at some distance from the grinding site and lead to inaccurate results. This concern can be tackled using IR thermography method since it is non-contact type in nature and hence, used.

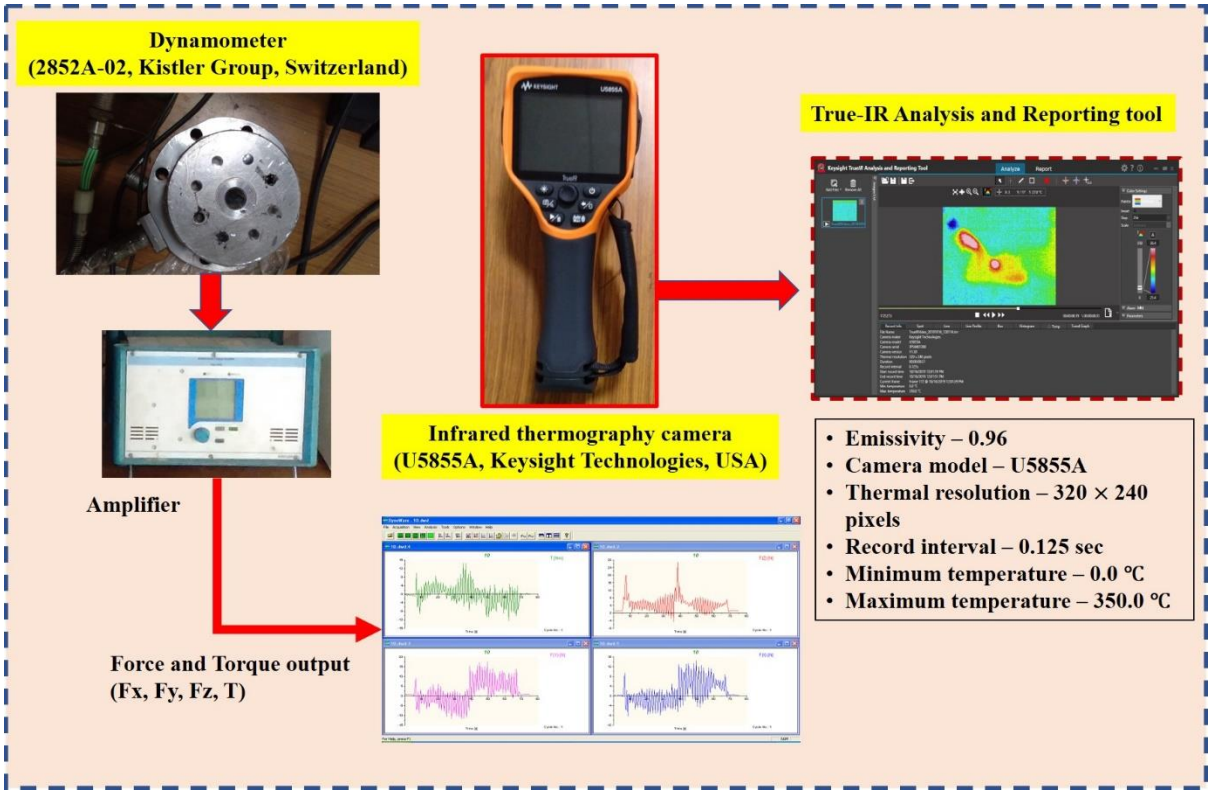

Figure 3.13: Representation of the devices used for measuring temperature and cutting forces.

Owing to the momentary contact of the grinding burr with bone, the infrared camera was focused on the surface of bone throughout the grinding. Therefore, authors were able to

measure the temperature on the surface of bone using IR camera even when tool disengages with the bone (refers to Figure 3.14).

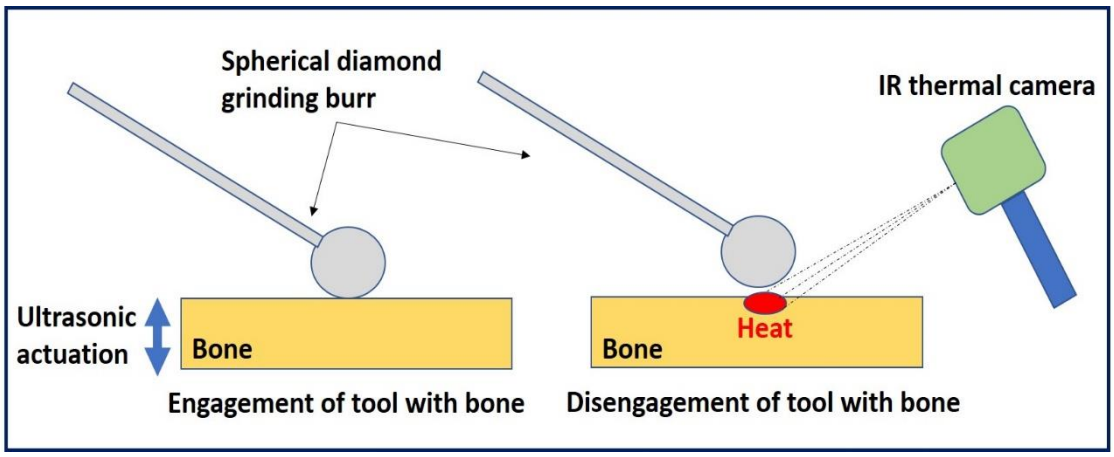

Figure 3.14: Schematic illustration showing the measurement of temperature on the surface of bone using IR thermography camera.

Furthermore, an infrared camera was recalibrated after each trial and results were re-confirmed using the temperature reading observed on using a laser gun. The measured temperature readings during bone grinding are then analyzed in Keysight True-IR analysis and reporting tool software.

The grinding forces and torque generated during the bone grinding was measured with a dynamometer (Model: 2852A-02, Kistler Group, Switzerland). The data obtained was further analyzed in the statistical software. The grinding burr was inclined at an angle of 30°. Furthermore, minimum forces were reported during conventional bone grinding at 30° orientation angle [180].

3.9 HISTOPATHOLOGY OF BONE SPECIMENS

Histological analyses were carried out on optimized samples to evaluate the osteonecrosis and thermal injury around the grinding site. Histological examination works as a means to determine the bone's health around the grinding zone. The standard preparation was performed to create bone tissue slides from the biopsy ground samples. First of all, the biopsy

specimens were labelled as per the machining conditions used during the osteotomy followed by tissue fixation process which prevents the specimens from decomposition and autolysis. The tissue samples were preserved using 10% formalin solution after bone grinding. Then de-calcification is carried out for 10 days before further processing of the tissue samples. Samples were cross-checked at 2-day intervals to ensure the proper decalcification. Bigger specimens are given multiple cuts and kept for fixation. Small tissue skins are made and then put in perforated metallic jar tissue processing cassettes. These cassettes are also put in a perforated metallic jar in a rotary machine called as histokinette. It consists of a central arm and 11 sided arms with 11 beakers. The aqueous fluid from the tissues is removed and then further processing is carried out by cleaning, embedding, and blocking. Tissue pieces were embedded in molten paraffin wax blocks.

After the operations of tissue processing, microtomy is carried out with the help of a microtome which cuts the section of tissue embedded in paraffin wax. The thickness of the section varies from 6 to 8 μm. The cutting knife is inserted into the microtome and is fixed firmly by tightening tools. Subsequently, trimming is carried out in which paraffin wax is cut and actual tissue is exposed. The paraffin block cuts better if it is placed on ice for 2-5 minutes before section cutting. After cutting, sections were floated out in hot water bath slides and to enhance the fixation of the tissue section, slides were then put on a rack and kept in an incubator. Cleaning is carried out by placing the slides in xylene jar for 2 mins. Then the tissue was passed through decreasing concentration of alcohol i.e. absolute alcohol for 2 mins, 90% alcohol for 1 min, 70% alcohol for 1 min. Afterwards, the sections underwent H and E staining. Haematoxylin (H) imparts blue colour and eosin (E) gives a pink colour to the cytoplasm. Haematoxylin stain was put on the slide for 20-30 mins and thereafter slides were washed in running water followed by differentiation using 1% acid alcohol for 3-8 seconds. Then again slides were washed under tap water for about 5 mins and eosin stain put for 2

mins followed by a wash with water. Subsequently, the slides were passed through increasing concentration of alcohol i.e. 50%, 70%, 90%, and absolute alcohol for dehydration. Again, slides were put in xylene for 2 mins and then a drop of DPX is put on the slide over tissue piece and covered with a rectangular or square coverslip. After the preparation of tissue slides, histograms were taken using an optical microscope (RADICAL) to visualize the thermal damage around in and around the grinding site in terms of volume of viable and non-viable osteocytes within lacunae. The percentage of the viable cell lacunas was calculated for a specified region which represents the number of viable osteocytes to the total number of osteocytes in the examined region. Figure 3.15 shows the location and size of the region selected for the histopathological examination have been demonstrated in the trial experiment.

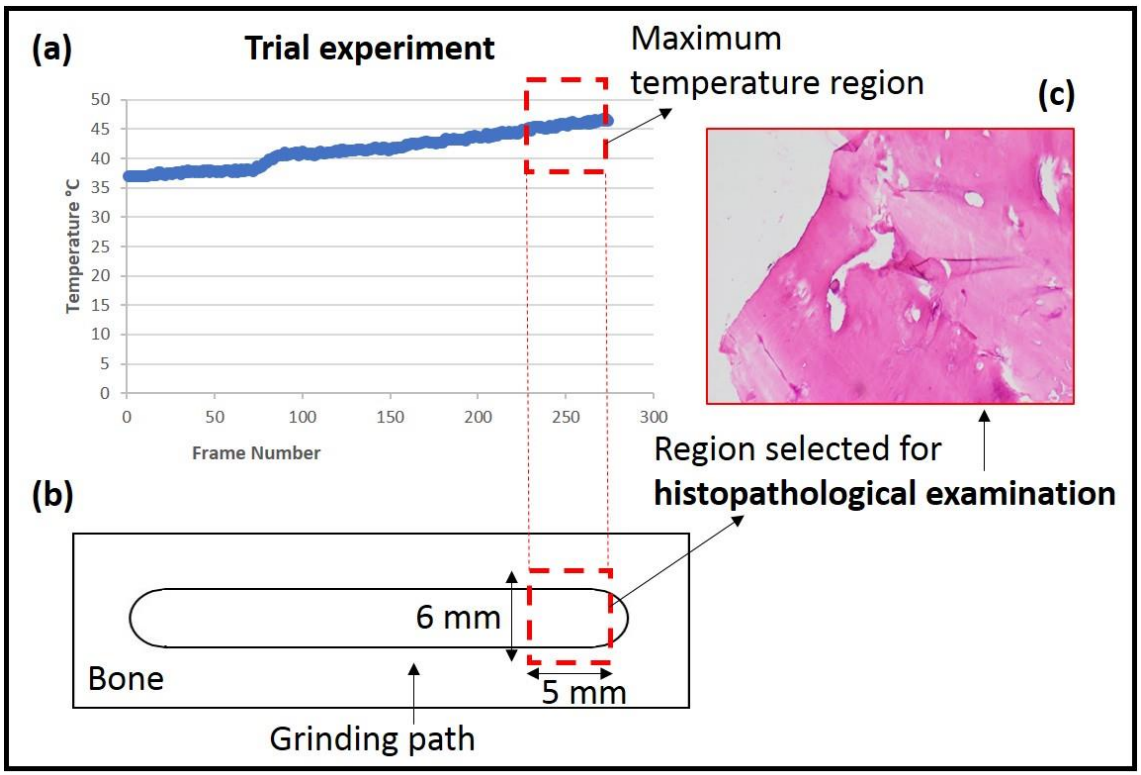

Figure 3.15: Location and size for a histological sample for evaluating the thermal damage.

Figure 3.15(a) depicts the temperature readings observed during the bone grinding. It clearly shows that as the grinding continues along the path (refers to Figure 3.15(b)), the temperature

keeps on increasing with the machining time. The region where maximum temperature readings observed were considered for evaluating the tissue damage during histopathological analysis as shown in Figure 3.15(c).

3.10 SUMMARY

The bone grinding experimental setup developed for the present study has been discussed in details along with the design and technical specifications for CBG and RUNG. The experimental design and experimentation procedure are well explained in this chapter. The technique used for measuring the temperature and cutting forces has been discussed along with their specifications. The characterization techniques used to study the post grinding specimens has been explained. The biological effect on the tissue during the bone grinding has been studied using the histopathology and its entire procedure is accentuated in this chapter.

CHAPTER 4: ANALYSIS AND DISCUSSIONS OF RESULTS

The results presented in this chapter comprises of the observations reported during bone grinding experiments. The temperature readings were measured using the infrared thermography technique. The tissue damage due to the rise in temperature has been discussed with the help of histopathological analysis. The results of cutting forces and torque measured using the dynamometer at different levels of process parameters are presented. The corresponding tool wear and burr loading (accumulation of bone debris within successive diamond grits) have been explained for different shape of grinding tools and its quantification results are presented. Furthermore, the surface morphology of the bone after grinding is presented duly supported with surface micrographs.

4.1 RESULTS USING PNEUMATIC EXPERIMENTAL SETUP

The results observed during high-speed pneumatic bone grinding setup were analysed and discussed. The bone specimens after rotary ultrasonic bone grinding experiments have been shown in Figure 4.1.

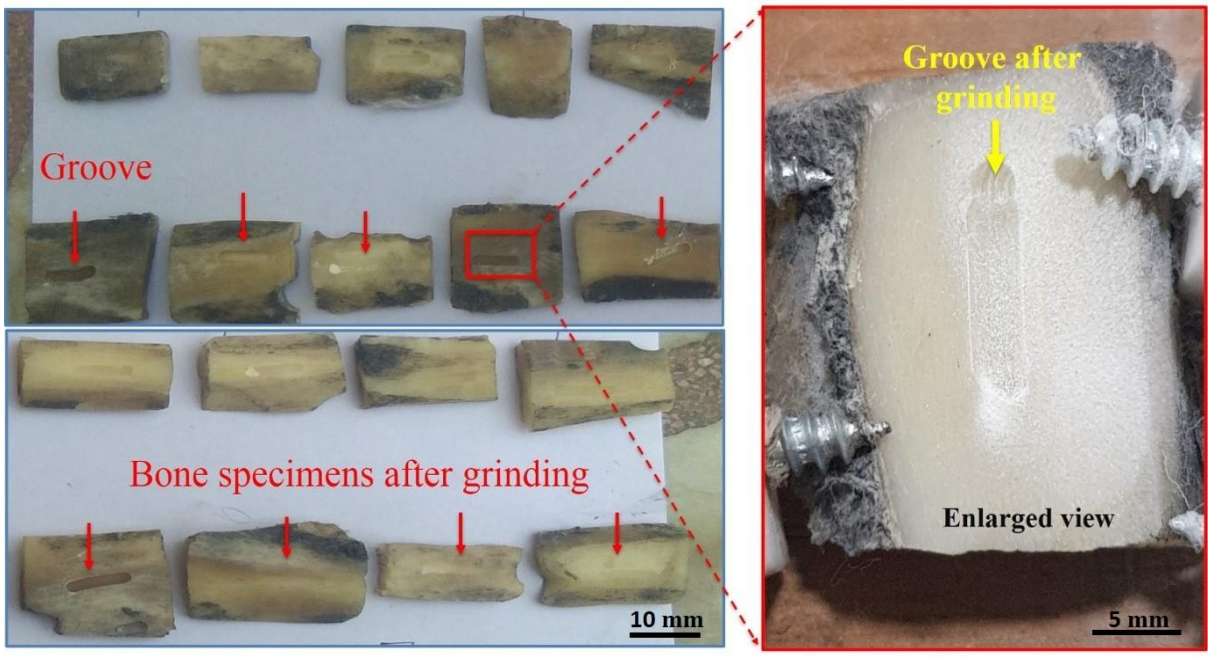

Figure 4.1: Bone Specimens after grinding.

4.1.1 Temperature Measurements

Table 4.1 shows the results obtained for average temperature and percentage of viable cell lacunas (filled osteocytes) for different parametric combinations. Standard order represents each possible unique combination of the process parameters.

Table 4.1. Full factorial experimental design and response variables during RUNG.

Exp. No.	Std order	Experimental setup				Response variable	
		Rotational speed (rpm)	Feed rate (mm/min)	Frequency (kHz)		Temperature (℃)	Standard deviation
						Avg.	S.D.
1	4	35000	40	20		42.3	1.25
2	23	55000	40	28		46.5	0.78
3	24	55000	40	40		47.5	0.62
4	7	35000	60	20		44.7	1.37
5	15	45000	40	40		44.3	2.07
6	6	35000	40	40		46.7	1.11

7	10	45000	20	20		41.5	2.17
8	19	55000	20	20		42.6	2.42
9	3	35000	20	40		44.6	1.97
10	2	35000	20	28		41.5	0.8
11	12	45000	20	40		42.3	0.61
12	11	45000	20	28		43	0.50
13	14	45000	40	28		45.2	1.06
14	20	55000	20	28		42.3	2.14
15	16	45000	60	20		45.2	1.65
16	9	35000	60	40		47.3	0.61
17	21	55000	20	40		45.7	1.04
18	5	35000	40	28		43.8	0.75
19	27	55000	60	40		50.8	1.06
20	13	45000	40	20		43.2	0.26
21	26	55000	60	28		45.2	1.10
22	17	45000	60	28		47.3	0.89
23	8	35000	60	28		43.2	0.80
24	25	55000	60	20		48.3	2.81
25	18	45000	60	40		49.5	1.32
26	22	55000	40	20		44.8	0.70
27	1	35000	20	20		38.8	1.93

The results presented are the average values and their standard deviation for triplicate experiments. Standard deviation (S.D.) shows the dispersion of data about the average value. It is vivid that parametric combination (std. order 1) with the rotational speed of 35000 rpm, a feed rate of 20 mm/min, and ultrasonic frequency of 20 kHz produces less temperature which is 38.8℃ and standard deviation of 1.93. Correspondingly, no thermal damage has been observed for these parametric conditions and only viable cell were found during histological examination with no disappeared osteocytes. On another side, severe thermal damage was reported for std order 27 i.e. rotational speed of 55000 rpm, a feed rate of 60 mm/min, and ultrasonic frequency of 40 kHz. The infrared thermograms at different time intervals 0, 5, 10, 15, 20 seconds during the experimentation with a rotational speed of 55000 rpm, a feed rate of 60 mm/min, and ultrasonic frequency of 40 kHz has been shown in Figure 4.2. As the

machining time increases, it was observed that temperature also increases for a constant feed rate.

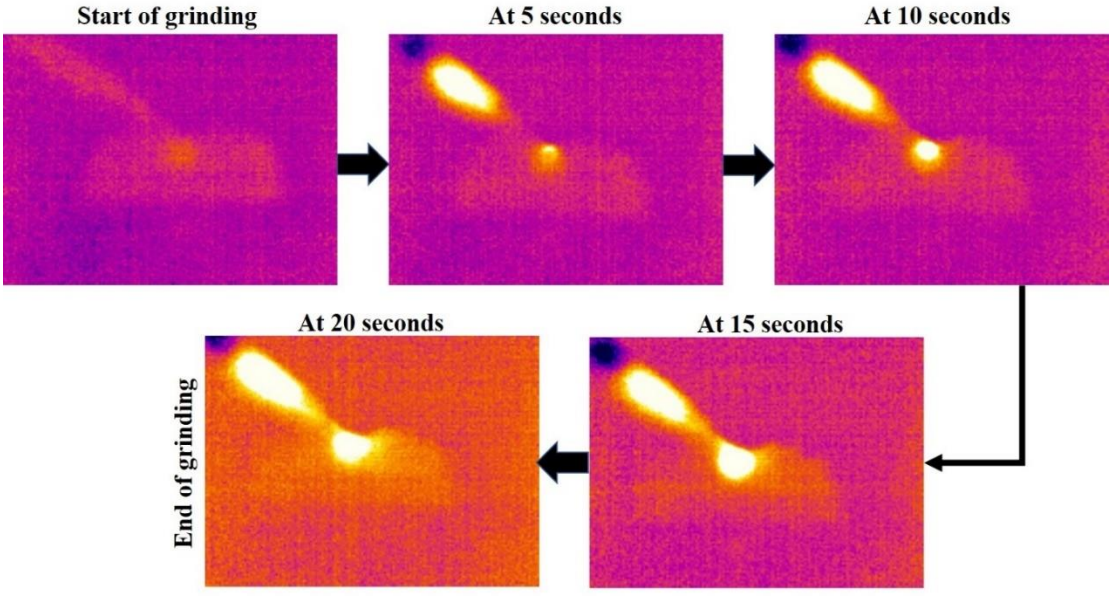

Figure 4.2: Infrared thermograms at different time intervals during the experimentation with 55000 rpm, 60 mm/min, and 40 kHz.

4.1.2 Statistical Analysis

Analysis of variance was implemented to determine the percentage contribution of each machining parameter towards the response variable at 95% confidence level (refer to Table 4.2). Linear and two-way interaction have been presented and results demonstrate that all three machining parameters rotational speed, feed rate, and frequency are significant terms which highly influences the response variable since their p-value is less than 0.05 (i.e. $p < 0.05$) and are also shown in Pareto chart (refer to Figure 4.3). The terms which are on the right side of the red dotted line (standardized effect = 2.306) are significant whereas the terms on the left side of the line are insignificant. It is clear that no significant interaction has been reported in the study and individual effects have a major contribution towards the response

characteristics. The maximum percentage contribution is of feed rate i.e. 45.43% followed by frequency (23.87%) and rotational speed (i.e. 12.85%).

Table 4.2. Analysis of variance (ANOVA) of temperature and percentage contribution.

Source	DF	Adj SS	Adj MS	F-Value	P-Value	Percentage contribution (%)
Model	18	180.222	10.012	9.27	0.002	95.42
Linear	6	155.158	25.860	23.93	0.000	82.15
Rotational speed	2	24.276	12.138	11.23	0.005*	12.85
Feed rate	2	85.796	42.898	39.70	0.000*	45.43
Frequency	2	45.087	22.543	20.86	0.001*	23.87
2-Way Interactions	12	25.064	2.089	1.93	0.178	13.27
Rotational speed*Feed rate	4	4.402	1.101	1.02	0.453	2.33
Rotational speed*Frequency	4	12.144	3.036	2.81	0.100	6.43
Feed rate*Frequency	4	8.518	2.129	1.97	0.192	4.51
Error	8	8.644	1.081			4.57
Total	26	188.867				

*represents significant terms

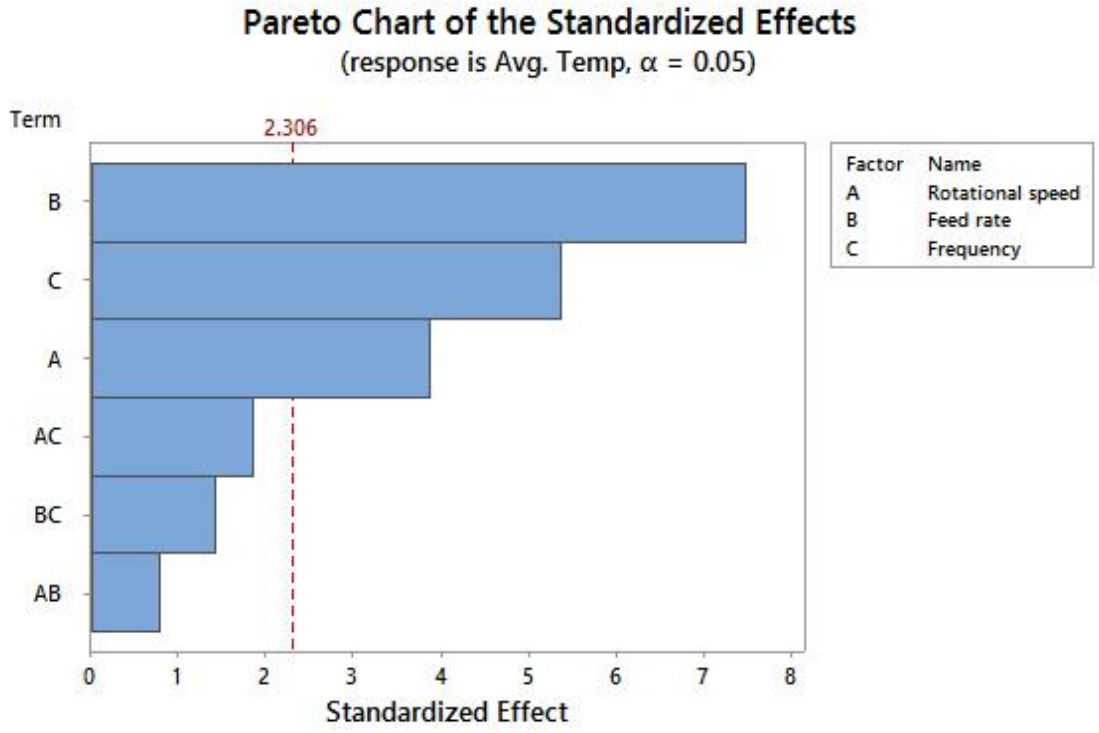

Figure 4.3: Pareto chart plot for temperature during RUNG.

4.1.3 Effect of Rotational Speed

The effect of process variables on the response parameters was determined and illustrated in Figure 4.4. It is revealed that the increase in rotational speed from 35000 rpm to 55000 rpm leads to the escalation of temperature at the grinding site (black coloured line) from 43.7 to 45.9℃.

4.1.4 Effect of Feed Rate

Figure 4.4 shows that temperature increases from 42.5 to 44.9℃ on increasing the feed rate from 20 to 40 mm/min (red coloured line). Further increase in the feed rate leads to the increment of temperature from 44.9 to 46.8℃ during 40 to 60 mm/min of feed rate.

4.1.5 Effect of Ultrasonic Frequency

The ultrasonic frequency also plays a significant role in the behaviour of change in temperature during bone grinding. It was revealed that as the frequency is increased from 20

to 28 kHz, the temperature increases from 43.4 to 44.2 ℃ and raises till then 46.5℃ at 40 kHz of ultrasonic frequency (blue coloured line).

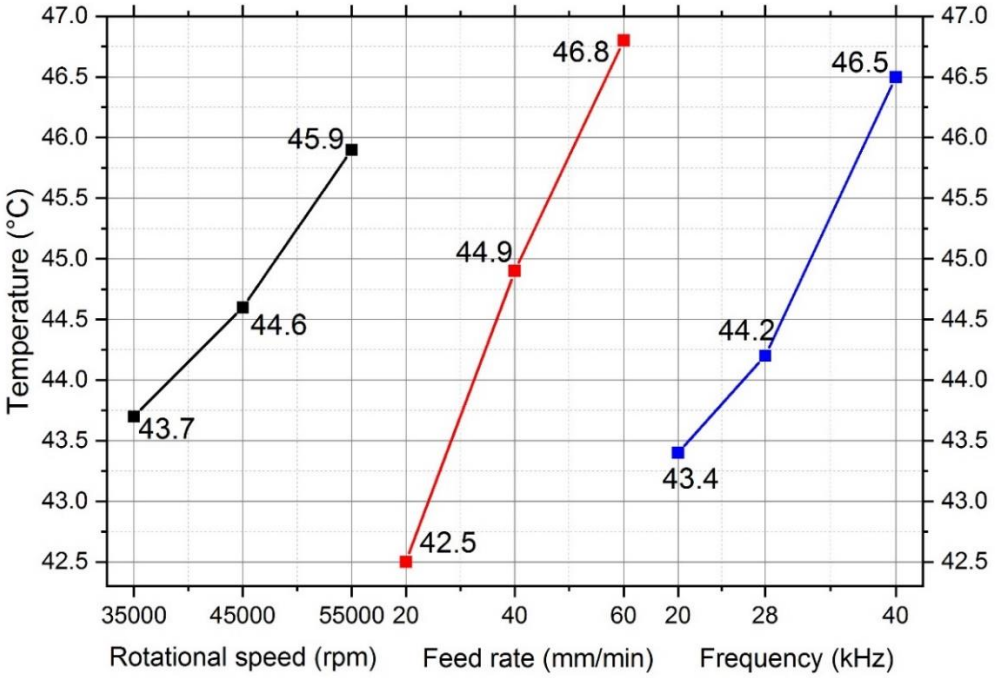

Figure 4.4: Parametric effect of input variables on temperature.

4.1.6 Effect of Interactions

Although, the interactions of individual variables are not significant. Nevertheless, interactions have 13.27% contribution in the criterion variable out of which 2.33% of rotational speed × feed rate, 6.43% of rotational speed × frequency, 4.51% of feed rate × frequency. Therefore, the 2-way interactions have been shown in terms of the combined parametric effect on the temperature rise during bone grinding, as evidently in Figure 4.5. It is vivid that temperature elevation keeps on increasing as the rotational speed and feed rate changed from level 1 to level 3. It was observed that temperature observed at a rotational speed of 35000 rpm and feed rate of 20 mm/min is less in comparison to the temperature observed at the rotational speed of 55000 rpm and feed rate of 20 mm/min.

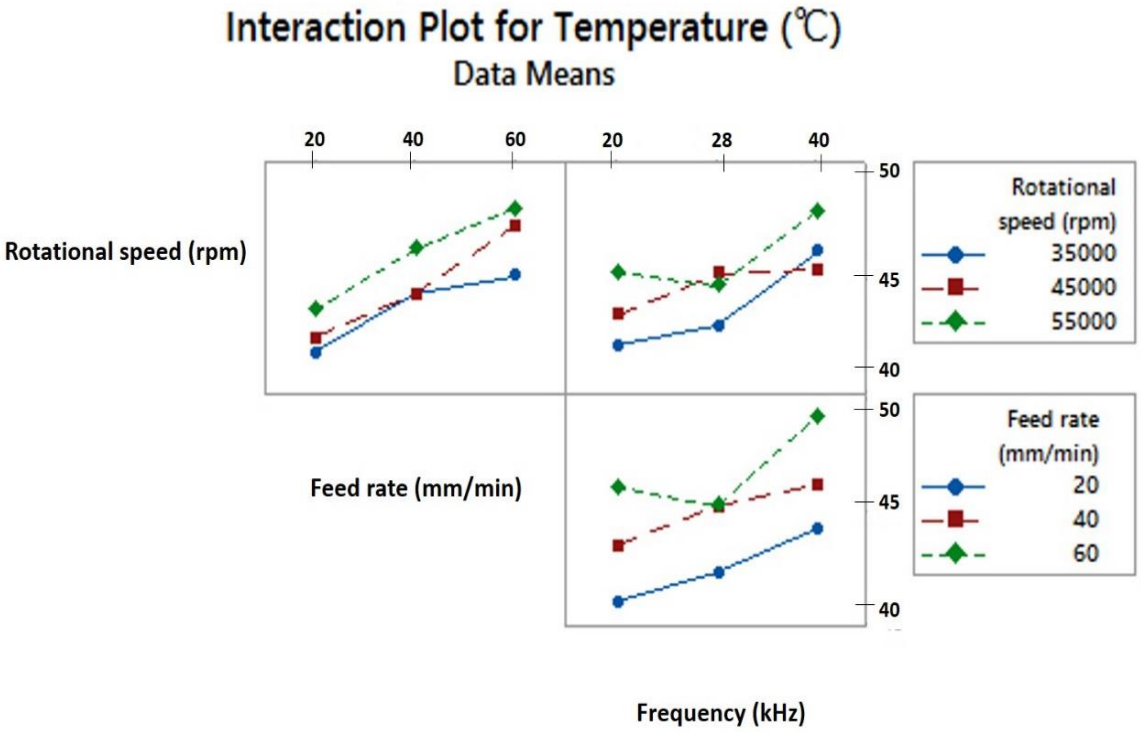

Figure 4.5: Interaction plots for temperature.

Similarly, the temperature increases as the rotational speed are increased keeping the frequency 20 kHz. It was observed that temperature reported at the rotational speed of 35000 rpm and frequency of 20 kHz is less in comparison to the temperature observed at the rotational speed of 55000 rpm and frequency of 20 kHz. However, at 28 kHz, a higher temperature is observed at 45000 rpm and lower at 35000 rpm. Furthermore, the higher temperature was observed at 55000 rpm when the ultrasonic frequency of 40 kHz is used. The combined increase in the feed rate and frequency also caused an increase in the temperature observed during bone grinding. It was observed that temperature reported at the feed rate of 20 mm/min and frequency of 20 kHz is less in comparison to the temperature observed at the feed rate of 60 mm/min and frequency of 20 kHz.

4.2 DISCUSSION

It was observed that lower levels of rotational speed, feed rate, and frequency results in better viability of the cell lacunas. The existence of higher shear and friction forces at higher

rotational speed leads to the rise in friction, thereby, increasing the temperature at the bone grinding site. Furthermore, it was noticed that the positive effect of applying the ultrasonic vibrations significantly declines at the higher rotational speed owing to the increases heat generation rate. At higher rotational speed the majority of kinetic energy is converted into the thermal energy; thereby, increasing the temperature at the grinding site. However, on another side, too much lower level of rotational speed leads to the larger chip size and thus causes a significant increment in the cutting forces which in turn can initiate and propagate microcracks over the surface of a bone. Subsequently, chip removal becomes difficult at a rotational speed less than 35000 rpm owing to the significant decrease in the centrifugal force and can further induce the risk of infection and thereby, post-operative healing time.

The higher level of feed rate is associated with the thermal necrosis and caused a significant decrease in the live osteocytes. The disappearance of the live osteocytes can be decreased by opting lower feed rate during bone grinding. More non-viable cells have been reported near the immediate vicinity of the cut surface at higher feed rate. It was observed that more material of the bone is removed at a higher level of feed rate; thereby, cause a significant increase in the temperature at grinding site owing to the increased heat generation rate due to larger material deformation. This rise in temperature then leads to osteonecrosis in and around the grinding site. The volume of penetration of abrasive grits into the bone increases on increasing the feed rate which leads to more material removal within the specified time. Moreover, increased penetration volume of abrasive grits also increases the size of bone chips produced during grinding. Therefore, excessive rubbing of the bone chips increases the friction at the grinding site and further contributes to the rising temperature. Furthermore, it is pragmatically noteworthy to mention that microcracks have been observed over the surface of a bone at a higher feed rate owing to the significant escalation in the cutting forces at a higher feed rate. However, at the feed rate of 20 mm/min, the rate of heat generation and friction

significantly reduces and thus leads to the decline in the temperature generated during bone grinding. Furthermore, it has been observed that feed rate less than 20 mm/min caused a significant increment in the machining time which certainly pose the risk of infection and increase exposure time. There are no strict guidelines for using the feed rate during actual in-vivo surgical operations. The neurosurgeons used feed rate as per their clinical experience.

The results also revealed that too low or too high frequencies are also undesirable. The higher frequencies i.e. ≥ 40 kHz caused a significant increase in the temperature elevation wing to the greater conversion of supplied energy into the heat. It is well established that the ultrasonic transducer requires more power consumption (i.e. energy) to effectively work at higher frequencies. Therefore, more amount of energy is transferred into the bone owing to the greater existence of the heat at higher frequencies. The lower thermal conductivity of the bone then further contributes to the increased temperature by entrapping the heat into the bone. There is no doubt that contact ratio significantly decreases at higher frequencies but the dissipation of the heat into the bone at higher frequencies overcomes the decrease in temperature owing to the reduction in contact ratio. Therefore, a higher temperature has been observed during bone grinding at higher ultrasonic frequencies. Whereas, the lower temperature has been observed at the lower levels of ultrasonic frequencies owing to the reduced contact ratio between the grinding burr and bone. The reduced contact time significantly decreases the transformation of heat into the grinding zone, thus lowering the temperature at the grinding site. Besides, the frequency of less than 20 kHz increases the contact time between grinding burr and bone. Subsequently, more heat is transferred into the bone owing to the increased time for conduction of heat. As a result, the lower level of ultrasonic grinding is preferable for bone grinding instead of performing conventional bone grinding. In the present study, better cell viability is attributed to vibrational movements resulting in an insignificant thermal alteration in the bone tissue.

The results obtained in the present study shows significant improvement in reducing the temperature elevation during bone grinding to avoid thermal trauma using ultrasonic-assisted grinding. It has been observed that intermittent contact leads to a decrease in the contact ratio between burr and bone. However, in the case of conventional grinding, grinding burr remains in direct contact with the bone during the entire course of grinding. Moreover, intermittent contact reduces the bone chip's rubbing against the surface of bone which in turn decreases the friction at the burr-bone interface. The pulsating action of the grinding burr caused a reduction in average friction at the interface. The intermittent contact during RUNG leads to the disengagement of the burr with bone and caused the removal of heat through the irrigating fluid. Furthermore, the rate of bone's material deformation can be hindered using intermittent contact since it is proportional to the heat generation. Hence, the temperature can be reduced using intermittent contact during bone grinding.

4.3 HISTOPATHOLOGY

At the microscopic level, compact bone consists of osteons (Haversian system). Further, each osteon has a cylindrical structure which consists of Haversian canal, lamellae, lacunae, and canaliculi. Haversian canal is a central tube which includes nerves and blood vessels. Lamellae ("little plates") are strong matrix concentric rings formed from mineral salts such as calcium, phosphate, and collagen fibres. The hardness to the bone's structure is imparted by minerals whereas collagen fibres provide strength to the bone. The small spaces between the lamellae in which bone cells (also called as "osteocytes") are present, known as Lacunae. Further, these lacunae are connected by minute channels known as canaliculi which are primarily responsible for the transport of nutrient to and waste products away from the osteocytes. It has been observed that the temperature of 43℃ leads to the cell necrosis which burns the osteocytes present within the lacunas of the osteons. However, the temperature of

47℃ for 1 min causes irreversible damage to the bone (bone death) and is termed as thermal necrosis or osteonecrosis [4,16,19,31,139].

The biological and structural entities have been revealed using histograms. The influence of grinding parameters rotational speed, feed rate, and frequency have been shown by evaluating thermal damage in the bone biopsy specimens which occurs due to the high temperature produced during grinding. The influence has been reported in terms of viable, non-viable osteocytes, partially filled lacunas, osteocyte density, a distance of viable and non-viable osteocytes from the cut surface, and canalicular system (Haversian canals). The viable lacunas (filled osteocytes) are shown by arrows indicating dark spots and non-viable osteocytes (empty lacunas) are represented by a dotted circle. The temperature of 43℃ has been considered as a threshold temperature to cause cell damage [55]. However, the threshold temperature of 47℃ cause irreversible damage to the bone cells (bone death) also termed as osteonecrosis [33,51,56,57].

Figure 4.6 shows the histological images of the biological samples with a rotational speed of 35000 rpm, a feed rate of 20 mm/min and frequency of 20 kHz (Figure 4.6(a) and 4.6(b); CBG, Figure 4.6(c) and 4.6(d); RUNG). Figure 4.6(a) and 4.6(b) shows that the majority of the cells are dead and have been resorbed in bone owing to the high temperature produced during bone grinding. Only a few viable osteocytes after 200 µm (approx.) away from the cut surface and high density of non-viable lacunas (empty osteocyte) are reported near the cut surface, as evidently in Figure 4.6(a) and 4.6(b). As expected, the disappearance of the cells decreases as the examination is focused away from the cut surface. Now, Figure 4.6(c) and 4.6(d) consists of a high density of viable lacunas (filled osteocytes) due to the low temperature generated during RUNG.

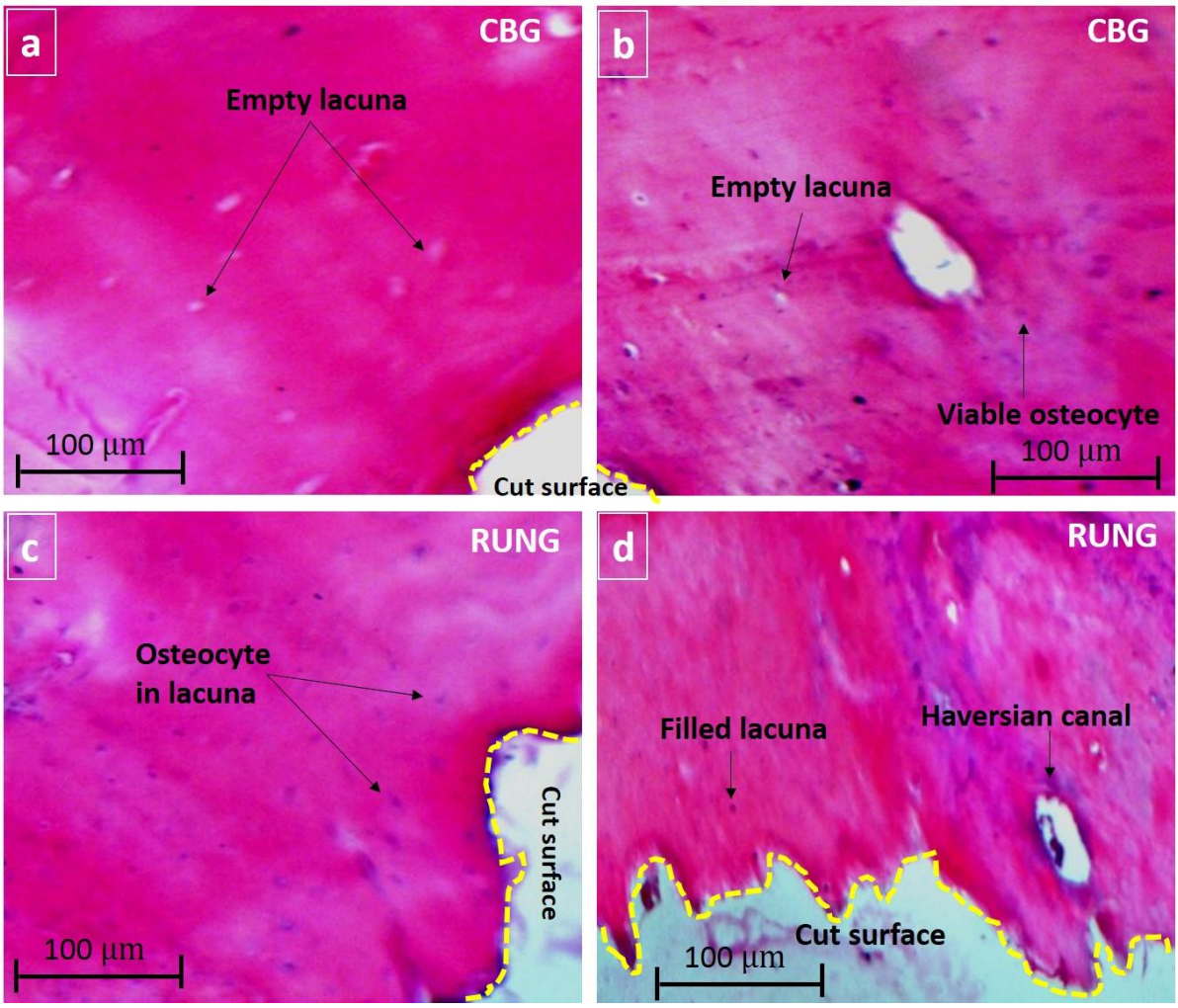

Figure 4.6: Histograms of the grinding parameters rotational speed = 35,000 rpm, feed rate = 20 mm/min, frequency = 20 kHz (causing minimum temperature) (a) and (b) conventional bone grinding (c) and (d) rotary ultrasonic bone grinding.

A few non-viable lacunas are also found. From histological images, it is observed that bone trabeculae have filled osteocytes and empty osteocytes which lies near and away from the cut surface as per the machining conditions opted to perform an osteotomy. Histograms are shown in Figure 4.6(c) and 4.6(d) are better than that shown in Fig 4.6(a) and 4.6(b) in terms of viable osteocytes, indicating less thermal damage in RUNG than observed in case of conventional grinding.

The majority of filled lacunas are visible near the cut surface in Figure 4.6(c) and 4.6(d) is due to the proposed RUNG process for bone grinding. Moreover, the temperature of 38.8℃ is observed during RUNG which is less than the threshold temperature of 43℃ to cause thermal trauma. Hence, no thermal damage is reported near the cut surface during RUNG. On another side, the majority of empty lacunas reported near the cut surface in Figure 4.6(a) and 4.6(b) because the generated temperature is 47.5℃ during CBG. Therefore, more thermal damage has been observed in the case of conventional grinding. Figure 4.7 shows the histological images of the biological samples with a rotational speed of 55000 rpm, a feed rate of 60 mm/min, and frequency of 40 kHz (Figure 4.7(a) and 4.7(b); CBG, Figure 4.7(c) and 4.7(d); RUNG).

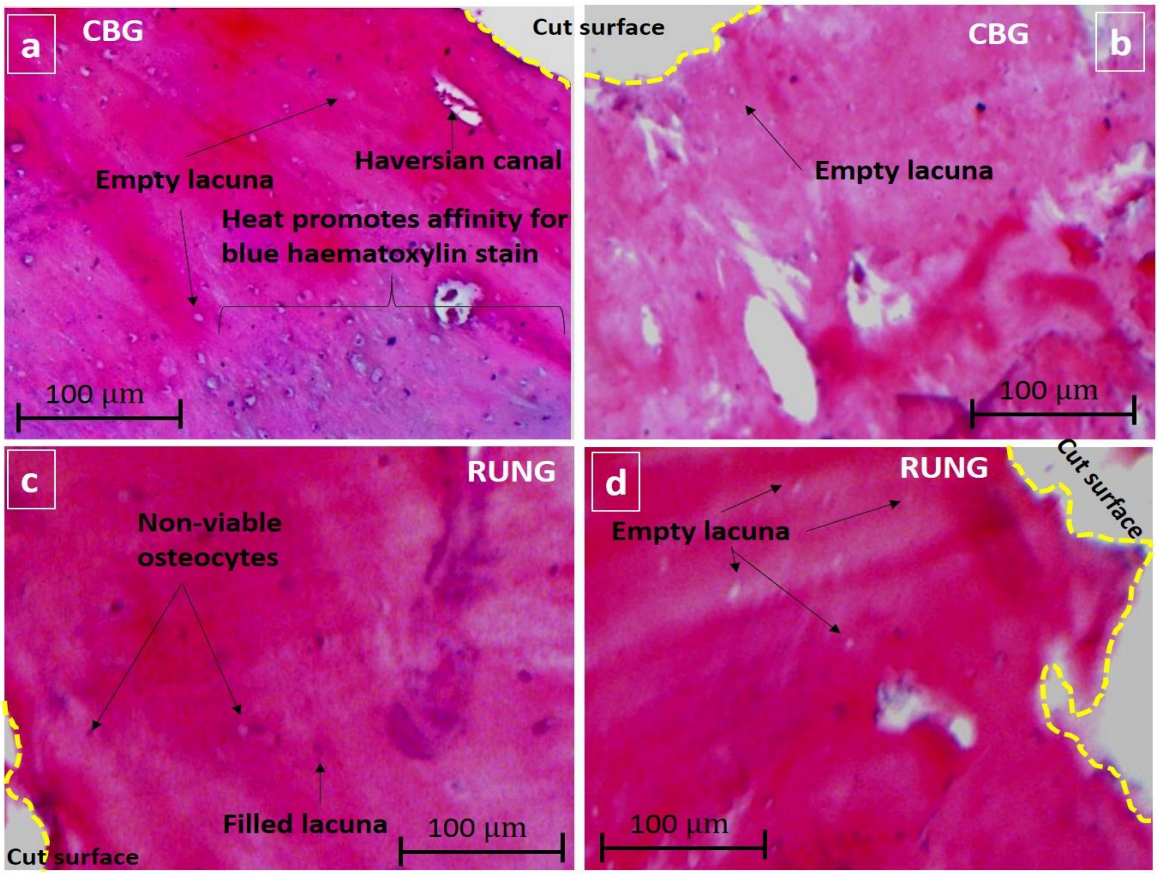

Figure 4.7: Histograms of the grinding parameters rotational speed = 55,000 rpm, feed rate = 60 mm/min, Frequency = 40 kHz (causing maximum temperature) (a) and (b) conventional bone grinding (c) and (d) rotary ultrasonic bone grinding.

The temperature obtained during CBG is 58.4℃ and during RUNG is 50.8℃. The density of non-viable osteocytes is more in Figure 4.7(a) and 4.7(b) which represent more thermal damage during grinding. Haversian canal and some partially filled lacunas are also visible. However, in case of RUNG more viable lacunas were present along with non-viable lacunas, at 200 µm (approx.) away from the cut surface. Throughout the histological analysis, it has been observed that lower temperature results in less damage to the osteocytes without the occurrence of necrosed tissues. Furthermore, it was noticed that lower rotational speed (35000 rpm), lower feed rate (20 mm/min), and lower frequency (20 kHz) caused less rise in temperature during bone grinding

On another side, higher levels of these parameters can significantly affect the temperature and subsequently bone's quality and its post-operative regeneration ability. Experimental data revealed that less temperature is generated in RUNG in comparison to the CBG. More severe cell damage has been seen in CBG in comparison to RUNG. These comparative results demonstrate the importance of using vibrations during surgical bone grinding. Furthermore, these experiments could lead to the automation of controlled robot-assisted bone grinding with the aid of ultrasonic vibrations.

The average temperature reported is 50.8℃ which is highest among all parametric combinations. Further, these parametric conditions with maximum and minimum temperature have been used to reveal the biological characteristics in terms of density of viable and non-viable lacunas. For this purpose, CBG experiments have been performed at these conditions for comparative analysis of response characteristics obtained during CBG and RUNG. At

each condition, three repetitive trials have been performed and their mean has been considered during examination. It has been revealed that CBG (i.e. 47.5℃) generates more temperature in comparison to RUNG (i.e.38.8℃) experiments (refer to Table 4.3). Histological examination revealed that in the case of CBG the density of viable lacunas is low and empty lacunas is high. However, in the case of RUNG, the density of viable lacunas is high and empty lacunas is low. Similarly, machining conditions with std. order 27 revealed that higher temperature is produced in CBG (i.e. 58.4℃) in comparison to RUNG (i.e. 50.8℃). The comparative results revealed that ultrasonic-assisted bone grinding generates less temperature than conventional bone grinding.

Table 4.3. Comparative analysis of CBG and RUNG with osteocyte conditions.

Process	Rotational speed (rpm)	Feed rate (mm/min)	Frequency (kHz)	Avg. Temp. (℃)	S.D.	Osteocyte condition	
						Viable lacunas	Empty lacunas
CBG	35000	20	−	47.5	1.50	Low	High
RUNG	35000	20	20	38.8	1.93	High	Low
CBG	55000	60	−	58.4	2.60	Low	High
RUNG	55000	60	40	50.8	1.06	Low	High

High temperature observed in the case of CBG has a significant effect on the bone's regeneration ability along with the grinding site. Histopathology of the specimens has revealed that grinding with the assistance of vibrations results in enhanced cell's viability and less thermal damage in comparison to the conventional grinding. The optimum parameters found for minimum temperature generation during bone grinding has been shown in Table 4.4.

Table 4.4: Optimum parameters for RUNG process.

Rotational speed (rpm)	Feed rate (mm/min)	Ultrasonic frequency (kHz)
35000	20	20

4.4 CUTTING FORCES AND TORQUE

Since the neurosurgeons use conventional bone grinding during craniotomy, therefore, the cutting forces produced during the bone grinding have been measured for CBG experiments. The cutting forces and torque developed during the conventional bone grinding experiments have been measured and analysed for determining the parametric effect on the response characteristics. All set of experiments have been performed thrice and their average has been presented. The effect of process parameters have been discussed in terms of tangential force, thrust force, and torque acting on the bone during. The schematic representation of the cutting forces in oblique (angle = 30°) and orthogonal grinding (angle = 90°) has been shown in Figure 4.8. In bone machining, the magnitude of thrust and tangential forces depends upon the input process parameters. The higher cutting forces may induce cracks on the surface of a bone.

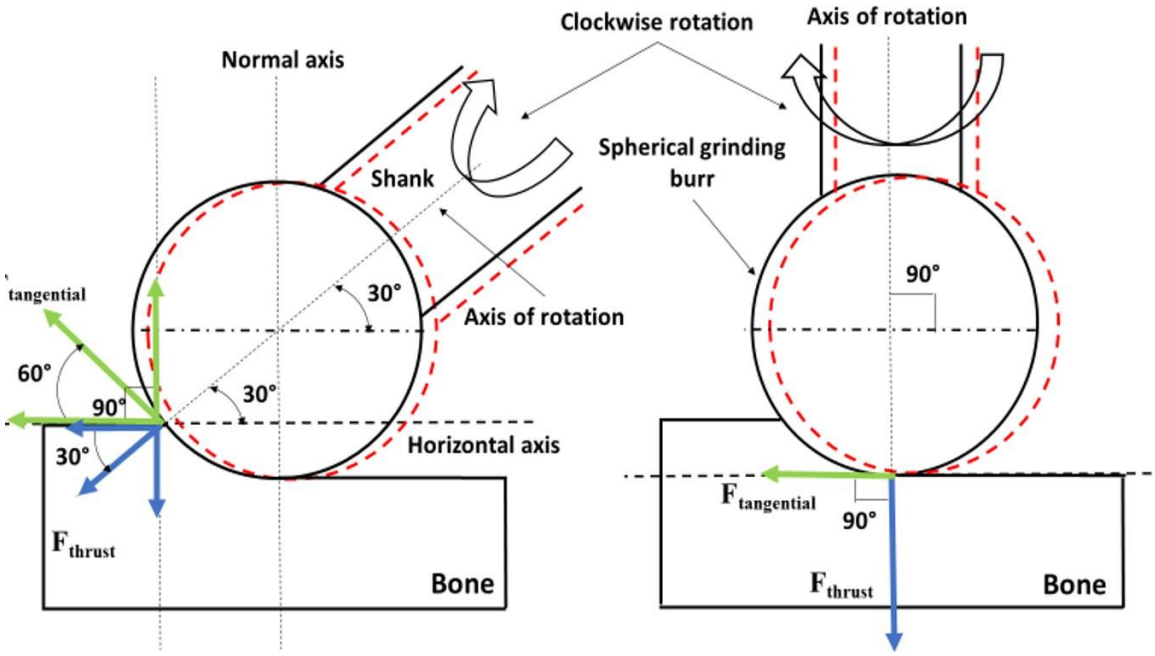

Figure 4.8: Schematic representation of the cutting forces in oblique (angle = 30°) and orthogonal grinding (angle = 90°).

4.4.1 Mechanism of Material Removal

The schematic representation of the bone grinding process has been shown in Figure 4.9(a). Figure 4.9(b) highlights the bone grinding process where the number of abrasives comes in contact with the bone's surface. Figure 4.9(c) shows the three possible stages of chips removal from the bone; (i) elastic-plastic deformation i.e. rubbing (ii) pile upstage in which bone chips start accumulating near the edges of abrasive grits owing to ploughing action (iii) cutting which leads to the removal of chips from the surface of a bone. Three types of grain and bone interactions simultaneously exist in the grinding namely rubbing, ploughing, and cutting.

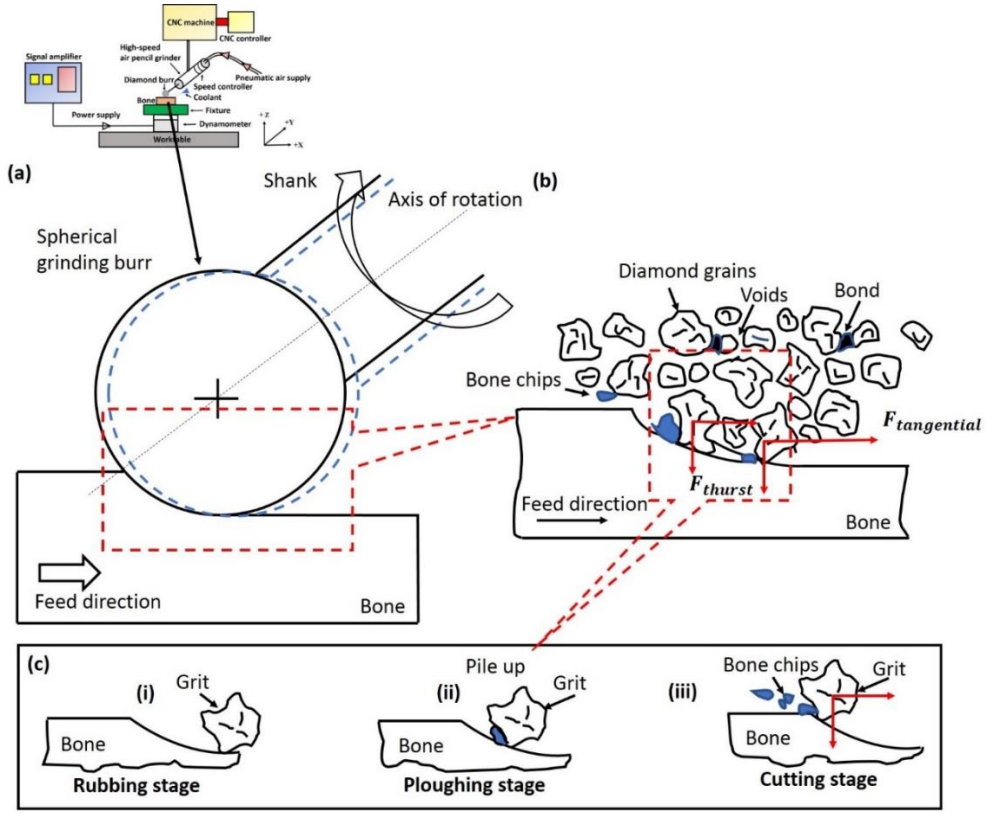

Figure 4.9: Schematic representation of the bone grinding process (a) bone and grinding burr contact (b) different stages of removal of bone chips (c) engagement and disengagement of diamond abrasive grits with bone.

At the rubbing stage, grain shears the bone's surface without permanent plastic deformation. Along with rubbing, other abrasive grains participate in the ploughing in which ridges are generated on either side of grain without actual material removal from the bone. In the cutting

stage, chips of the bone are formed and material is removed from the surface of the bone in terms of microchips of bone. It is expected that the contribution of cutting increased and rubbing contribution decreases with the escalation of the depth of cut, thereby, increase in the shearing and cutting forces. Increase in speed caused a greater number of grains to come in contact with the bone and thus reducing the burden on individual grains.

4.4.2 Effect of Rotational Speed on Tangential Force

The effect of osteotomy parameters on the tangential force has been studied by plotting the histograms shown in Figure 4.10. Figure 4.10(a) demonstrates the reading of cutting force and standard deviation during bone grinding against rotational speed and feed rate (depth of cut of 0.50 mm). It is observed that at 35000 rpm, the tangential force found to be 16.88, 17.78, and 19.48 N at a feed rate of level 1, level 2, and level 3 respectively. At 45000 rpm, tangential force is 15.14, 16.89, and 18.44 N for a feed rate of 20, 40, and 60 mm/min respectively.

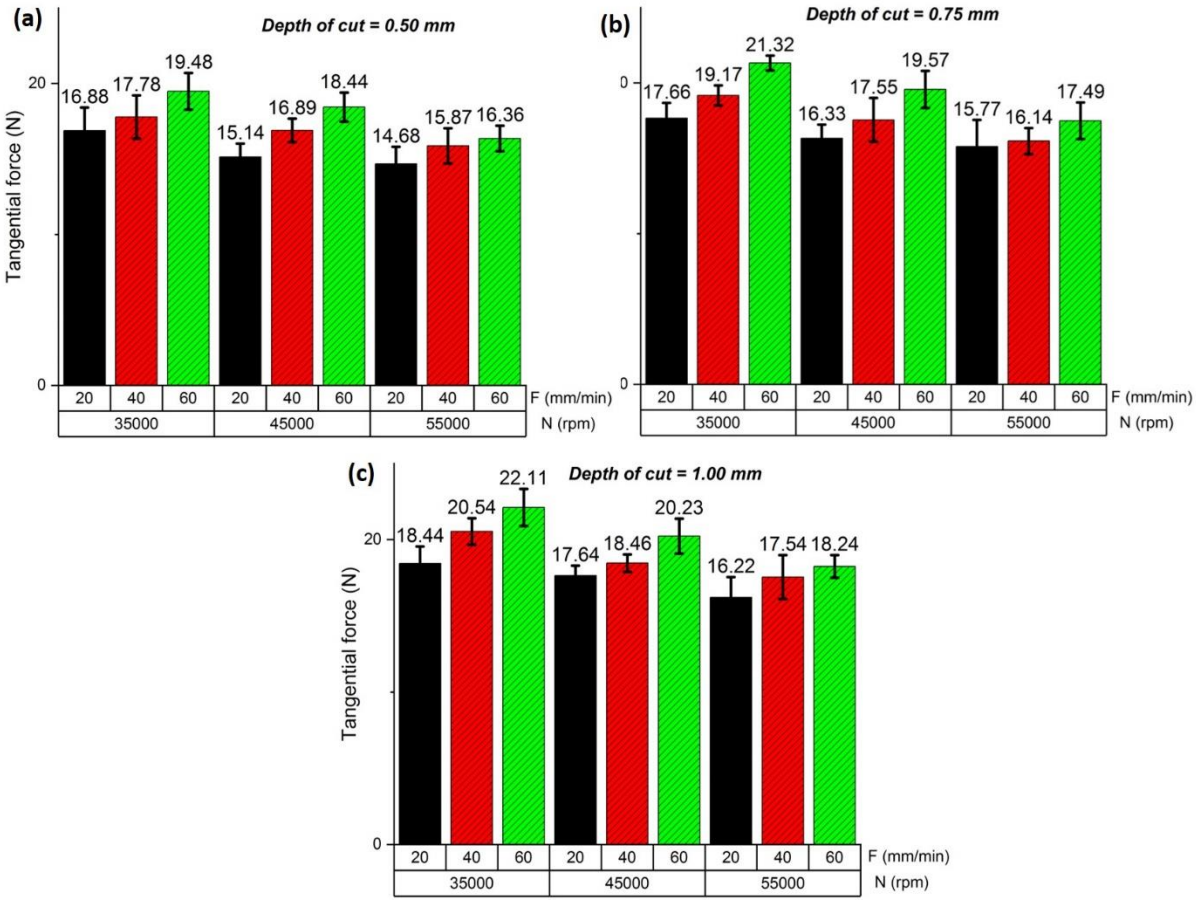

Figure 4.10: Tangential force measured at different rotational speed (rpm) and feed rate (mm/min) at different levels (0.50, 0.75, 1.00 mm) of the depth of cut.

Whereas at 55000 rpm, tangential force is 14.68, 15.87, and 16.36 N for a feed rate of 20, 40, and 60 mm/min respectively. In bone grinding, rotational speed has a significant role in cutting forces. It has been revealed that increase in speed caused a significant decrease in tangential force. Maximum tangential force 19.48 N is noticed at 60 mm/min with 35000 rpm. On another side, the minimum tangential force of 14.68 N is obtained for 20 mm/min and 55000 rpm. The maximum tangential force at 35000, 45000, and 55000 found to be 19.48, 18.44, and 16.36 N which shows that higher rotational speed is preferable for bone grinding. The possible reason could be decreased in the mean friction coefficient at a higher rotational speed.

Alam et al. [158] and Wang et al. [181] outlined that mean friction coefficient is linearly related to the grinding force and decreases at a higher speed. Additionally, at higher rotational speed, thinner cuts are observed which require less deformation energy and results in an exponential decrease in the tangential force.

Furthermore, Shakouri and Mirfallah [139] suggested that at higher rotational speed, the size of bone chips starts decreasing which leads to the reduction in cutting forces. Many other experimental studies have also reported a decrease in cutting forces with the escalation of rotational speed [8,87,107,182]. Recently, Liu et al.[183] outlined that many grits in the grinding zone significantly increases on increasing the rotational speed of the grinding wheel due to which burden on individual grit decrease and volumetric material removal per grit decrease. Subsequently, cutting forces also decreases. Similarly, Figure 4.10(b) and 4.10(c) demonstrate the reading of cutting force and standard deviation during bone grinding against rotational speed and feed rate at 0.75 and 1.00 mm depth respectively. Similarly, it has been observed that the tangential force keeps on decreasing when rotational speed increased from 35000 to 55000 rpm.

4.4.3 Effect of Feed Rate on Tangential Force

The feed rate shows the opposite trend of the rotational speed as the tangential force increase at higher feed rates. At feed rate of 20 mm/min, the tangential force found to be 16.88, 15.14, and 14.68 N at the rotational speed of 35000, 45000, and 55000 rpm respectively. At 40 mm/min, the tangential force found to be 17.78, 16.89, and 15.87 N at 35000, 45000, and 55000 rpm respectively. At 60 mm/min, the tangential force found to be 19.48, 18.44, and 16.36 N at 35000, 45000, and 55000 rpm respectively at depth of cut 0.50 mm (refers to Figure 4.10(a)). Similar kind of trend results is also reported for 0.75 and 1.00 mm of the depth of cut. It is expected that a deeper cut is seen at a higher feed rate which requires more shearing energy which eventually increases the grinding forces. Keeping all parameter

constant, material removal rate significantly affects the material removal rate. At higher feed rate, tool's penetration volume into the bone increase and cause a significant increase in the grinding forces. Liu et al.[183] highlighted that an increase in the feed rate leads to increment in the contact area, thereby increasing the cutting thickness of single grit which eventually increases the grinding forces. Therefore, it is revealed that the lower feed rate is preferable for bone grinding to achieve minimum tangential force during bone grinding.

4.4.4 Effect of Depth of Cut on Tangential Force

The same trend in the results reported where cutting forces increases with increment in the depth of cut. The depth of cut also has a substantial effect on the tangential force acting at the burr-bone interface during bone grinding. Figure 4.10(a) shows that tangential force at 35000 rpm and 20 mm/min is 16.88 N corresponding at 0.50 mm of the depth of cut, 17.66 N corresponding at 0.75 mm, and 18.44 mm at 1.00 mm. Similarly, at 45000 rpm and 20 mm/min, tangential force is 15.14 N, 16.33 N, and 17.64 N at 0.50, 0.75, and 1.00 mm depth respectively. At the third level of rotational speed i.e. at 55000 rpm, tangential force is 14.68 N, 15.87 N, and 16.36 N at 20, 40, and 60 mm/min corresponding to 0.50 mm of the depth of cut respectively. Similarly, it is vivid that tangential force is 15.77 N, 16.14 N, and 17.49 N at 20, 40, and 60 mm/min corresponding to 0.75 mm of the depth of cut respectively. At a higher depth of cut of 1.00 mm, it is observed that tangential force is 16.22 N, 17.54 N, and 18.24 N at 20, 40, and 60 mm/min of feed rate respectively. It is expected that thicker chips are sheared from the surface of the bone at higher depth of cut which causes an increment in cutting forces and shearing energy. Hence, the tangential force increases with the depth of grinding.

4.4.5 Parametric Effect on Thrust Force

Figure 4.11(a) illustrates the reading of thrust force and standard deviation during bone grinding against rotational speed and feed rate at 0.50 mm. It is observed that at 35000 rpm, the thrust force found to be 7.14, 8.05, and 8.68 N for a feed rate of level 1 (20 mm/min), level 2 (40mm/min), and level 3 (60 mm/min) respectively. At 45000 rpm, the corresponding thrust force is 6.23, 7.10, and 7.96 N respectively while at 55000 rpm, the thrust force is 5.26, 5.85, and 6.88 N respectively.

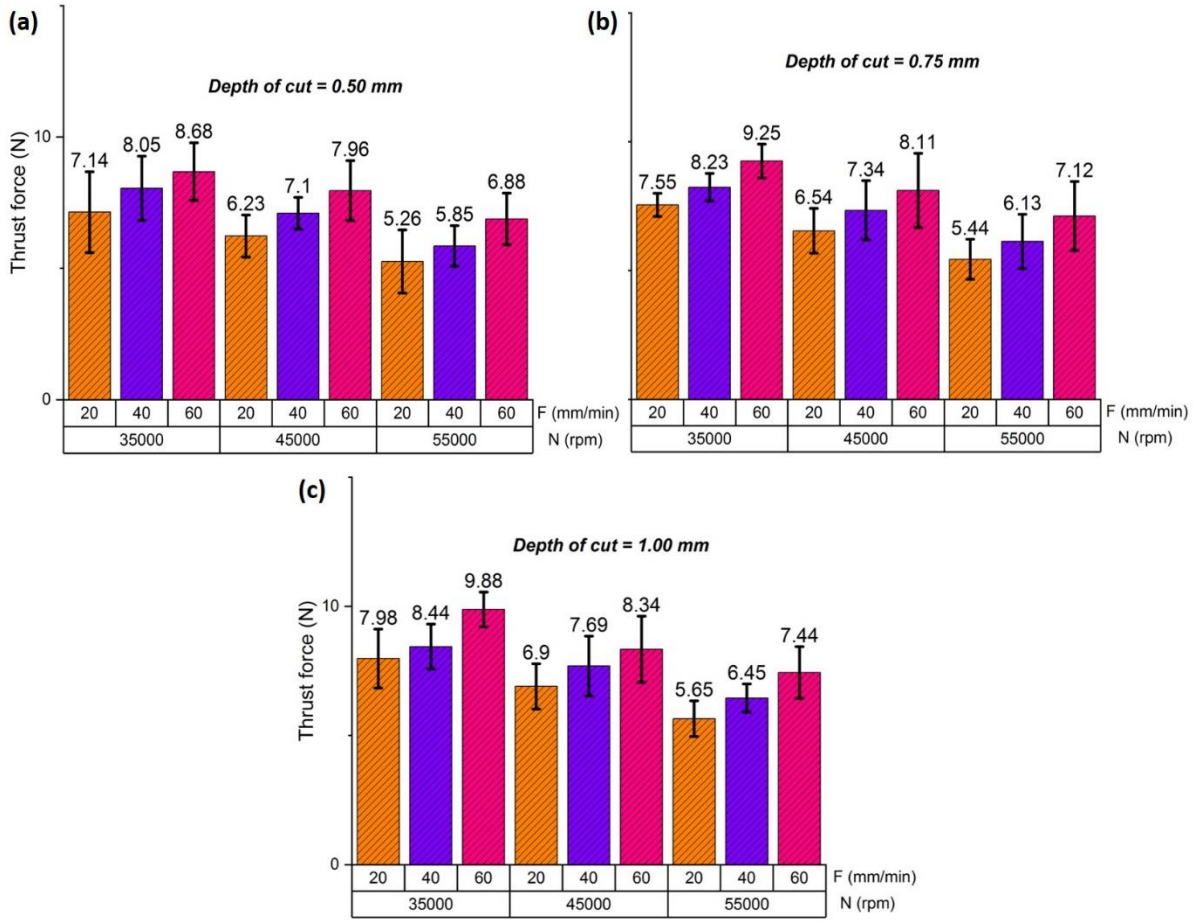

Figure 4.11: Thrust force measured at different rotational speed and feed rate at different levels (0.50, 0.75, 1.00 mm) of the depth of cut.

It was revealed that as the rotational speed is increased, thrust force starts decreasing. This is due to the decrease in mean friction coefficient at a higher rotational speed. Similarly, Figure 4.11(b) and 4.11(c) demonstrate the reading of cutting force and standard deviation during bone grinding against rotational speed and feed rate at 0.75 and 1.00 mm respectively.

At 20 mm/min, the thrust force found to be 7.14, 6.23, and 5.26 N at level 1, level 2, and level 3 respectively. At feed rate of 40 mm/min, the thrust force found to be 8.05, 7.10, and 5.85 N at the rotational speed of 35000, 45000, and 55000 rpm respectively. At 60 mm/min, the thrust force found to be 8.68, 7.96, and 6.88 N at 35000, 45000, and 55000 rpm respectively. It is expected as deeper cuts are observed at higher feed rate and further deeper cut leads to increase ground forces. It was revealed that the magnitude of thrust force is less than the tangential force when grinding is performed at an angle of 30°. Similarly, thrust force increases with an escalation in the depth of cut. The magnitude of the thrust force is higher when grinding burr penetrates the bone to cover 0.50 mm depth of cut.

4.4.6 Parametric Effect on Torque

Figure 4.12(a) illustrates the reading of torque and standard deviation during bone grinding against rotational speed and feed rate at a constant depth of cut of 0.50 mm. It is observed that at 35000 rpm, the torque found to be 2.32, 3.10, and 3.88 N-mm for three different levels of feed rate respectively. At 45000 rpm, torque is 1.33, 1.98, and 3.47 N-mm respectively and at 55000 rpm, torque is 0.70, 1.84, and 2.75 N-mm respectively. In bone grinding, rotational speed has a significant role in torque generated during bone grinding. It has been revealed that as the rotational speed is increased, torque starts decreasing. Mean friction coefficient is approximately linearly proportional to the torque. It has been observed that the mean friction coefficient reduces at a higher rotational speed [184]. Similarly, Figure 4.12(b) and 4.12(c) demonstrate the reading of cutting force and standard deviation during bone grinding against rotational speed and feed rate at 0.75 and 1.00 mm depth respectively.

At feed rate of 20 mm/min, the torque found to be 2.32, 1.33, and 0.70 N-mm at the rotational speed of 35000, 45000, and 55000 rpm respectively. At 40 mm/min, the torque found to be 3.10, 1.98, and 1.84 N-mm at the rotational speed of 35000, 45000, and 55000 rpm respectively. At 60 mm/min, the torque found to be 3.88, 3.47, and 2.75 N-mm at the

rotational speed of 35000, 45000, and 55000 rpm respectively. Therefore, it is revealed that torque increases with an increase in rotational speed from 35000 to 55000 rpm, feed rate from 20 to 60 mm/min, and depth of cut of 0.50 to 1.00 mm. Hence, it is revealed that lower speed, feed rate, and depth of cut preferable for bone grinding to achieve minimum torque during bone grinding.

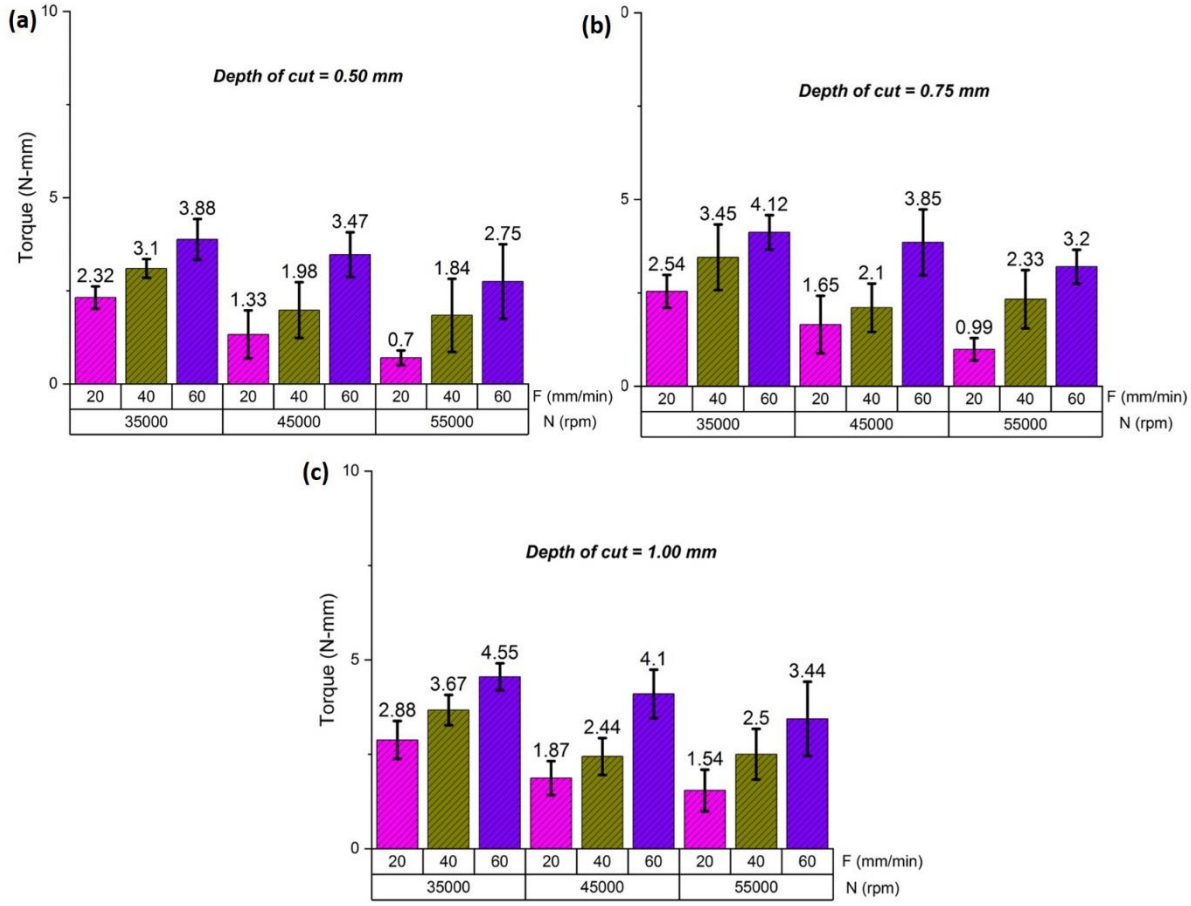

Figure 4.12: Torque measured at different rotational speed and feed rate at different levels (0.50, 0.75, 1.00 mm) of the depth of cut.

4.5 TOOL WEAR & BURR LOADING

For tool wear analysis, digital microscope (44302 deluxe, Celestron, USA) is used for all four tools and its different faces are observed. The tool wear on the lateral face as well as on end face is analyzed while grinding porcine bone in two stages: (a) fresh tool and (b) after grinding. The tool wear is analyzed for grain fracture, grains dislodging and tool loading.

Tool loading refers to the bone particles which are settled in the spaces between two successive grains and called ‘gullet’.

4.5.1 Tool’s Lateral Face

Figure 4.13 and Figure 4.14 shows the lateral faces of the grinding burr before and after grinding respectively with their surface micrographs. Initially, there was no tool wear and tool loading was observed. The abrasives are sharp enough and fixed to their positions. After grinding, fracture and dislodging of abrasives are visible in all the tools.

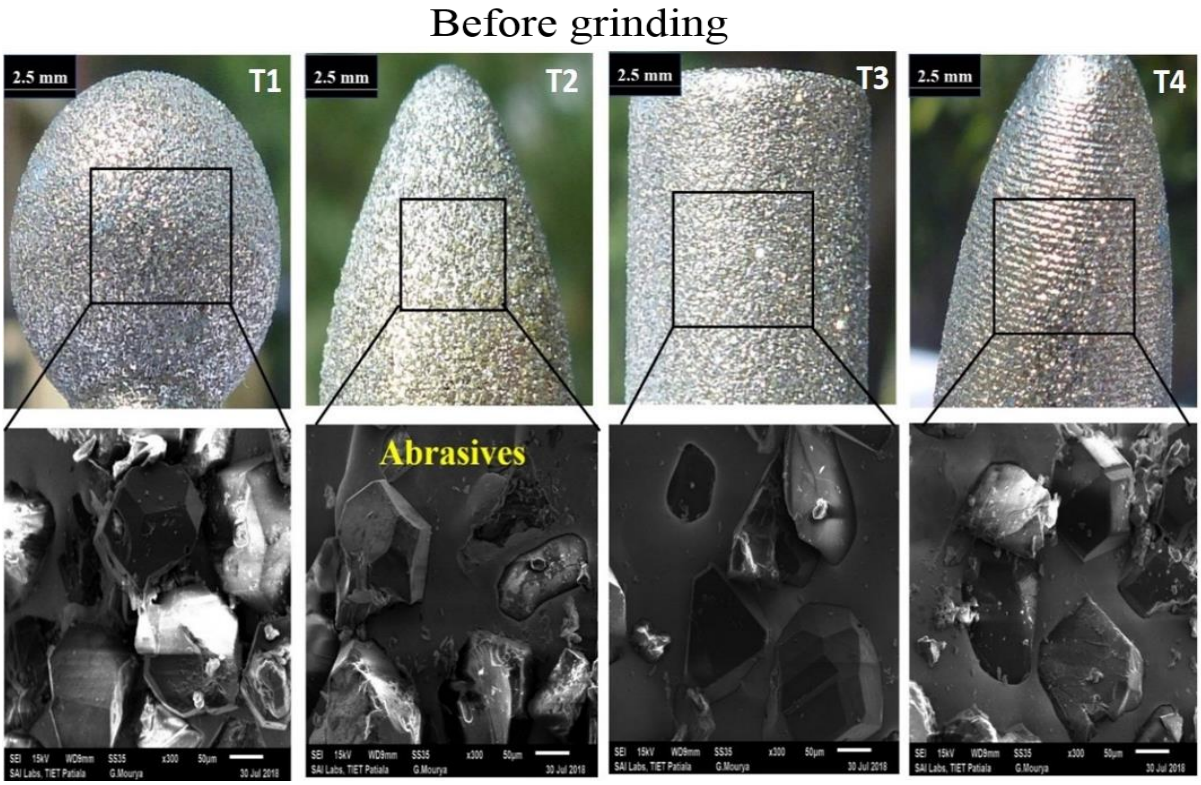

Figure 4.13: Lateral face of different types of fresh tools and corresponding SEM pictures.

The microchips produced during the grinding are adhered in the empty spaces, present between the diamond grains, over the surface of burr and can be seen in Figure 4.14 (tool T1 & T2). The flat land shown in the case of T3 & T4 tool is expected to become attrition wear because the sharp edges gradually become rounded after grinding and have glaze appearance.

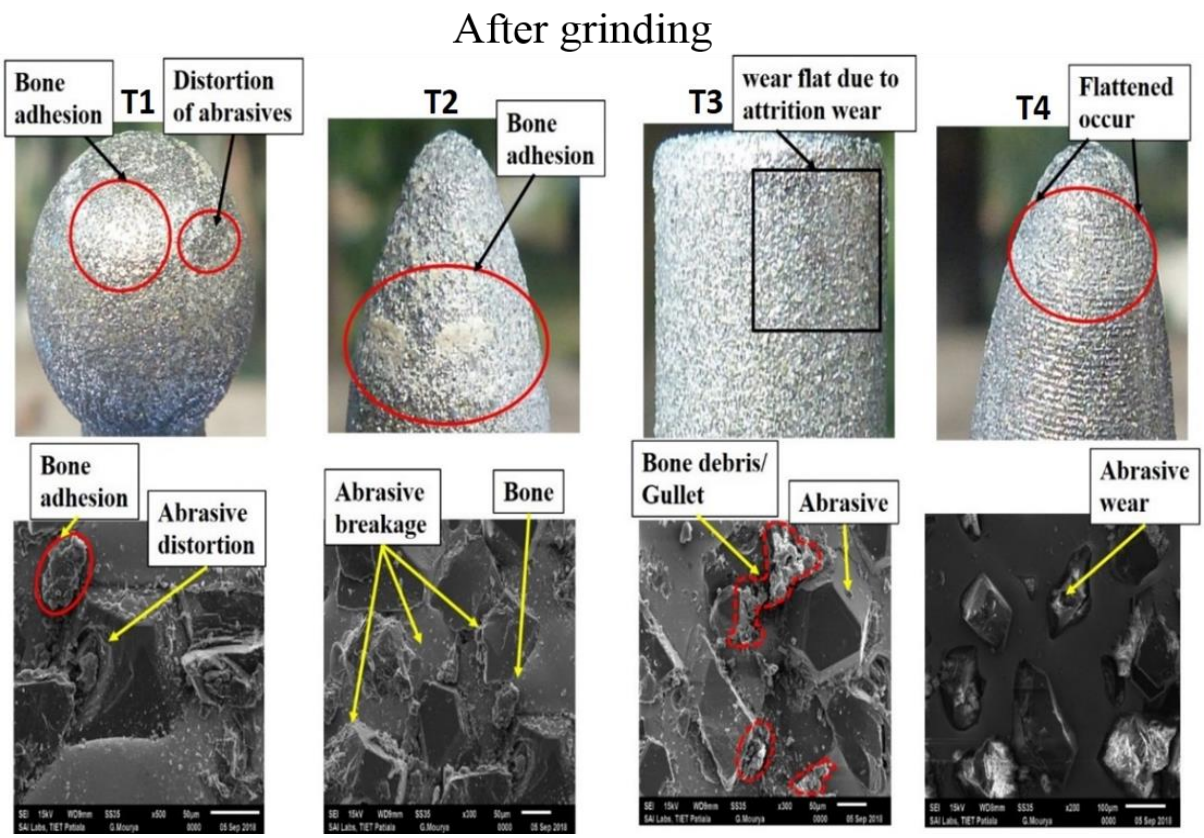

Figure 4.14: Lateral face of different types of used tools and corresponding SEM pictures.

Three combined mechanisms such as attrition wear, grain fracture, and bond fracture are expected to be occurring simultaneously for tool wear. Attrition wear mainly occurs at the contact surface (A) of the grain-workpiece interface as shown in Figure 4.15. It may happen due to the micro-fracture, plastic flow, and crumbling of sharp grit cutting edges which results in wear flats on the grit tips. In attrition wear, an amalgamation of cutting and sliding forces strongly influence the formation of chips and growth of wear flat and attrition wear contributes maximum in the distortion of the tool [126]. Attrition wear is a thermally activated mechanism which occurs due to the high temperature produced during the grinding. On the other side, grain fracture (B) occurs due to the high stresses on the grain which ultimately fractures the grit into small fragments and hence new cutting points are exposed. Bond fracture (C) also significantly contributes to the tool's deformation due to dislodging of abrasives grains over the tool surface which happens because of fracture of bond-post.

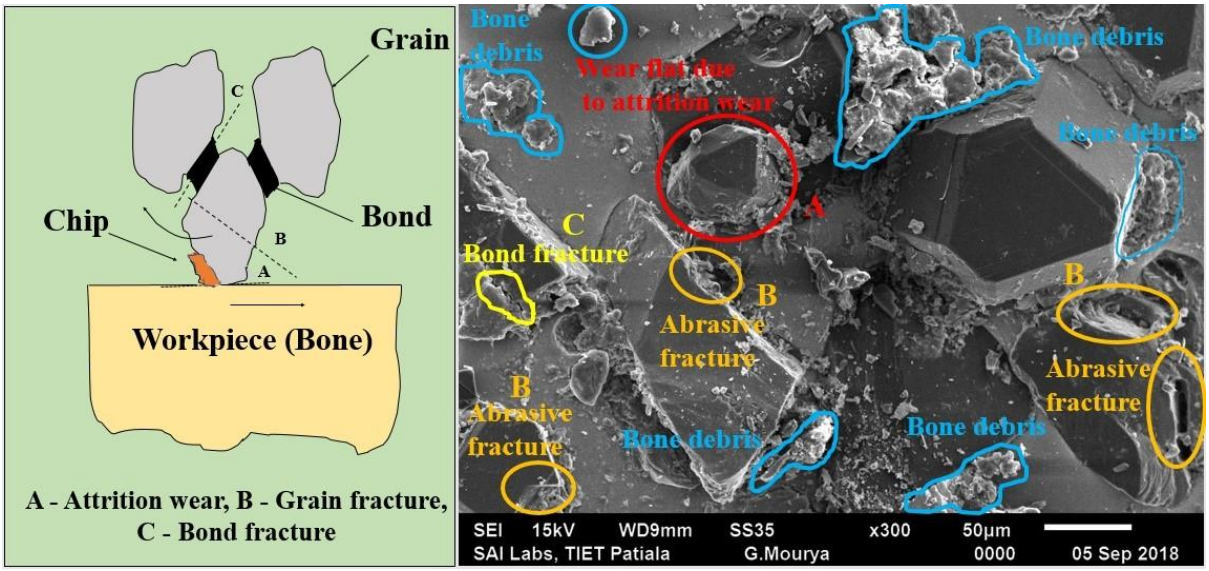

Figure 4.15: Schematic of three types of tool wear: (A) attrition wear, (B) grain fracture, and (C) bond failure.

4.5.2 Tool's End Face

During osteotomy by diamond-impregnated abrasive tools, some of the abrasives over the end face of tool dislodged and flushed away with coolant due to fracture of a bond which holds the diamond grains at their respective locations. Figure 4.16 and Figure 4.17 represents the surface micrographs of the end face of grinding burr before and after grinding respectively. The interface between abrasive grains and base metal bond gets highly deteriorated due to the combined effect of impact force and temperature which even leads to the premature pullout of the diamond abrasives from their bond. The wear at the tool's end face primarily occurs due to the grain fracture. It was noticed in all four cases of different shaped tools, wear on end face is more as compared to a lateral face of the tool. It is expected that the end face makes the first contact with the workpiece and hence wears off gradually. Thus, results in more wear whereas, the lateral face is not in direct contact with the surface of the bone. Therefore, owing to lesser cutting forces at the lateral face of the tool ultimately results in lesser tool wear.

The end face of every tool is continuously in contact with the surface to be machined due to which heavy chipping and dislodging was observed as shown in Figure 4.17. The effective area in contact with the bone surface is more in case of the cylindrical tool due to which a greater number of moving abrasives came in direct contact with the bone surface which ultimately increased the temperature at the burr-bone interface because of high shear and cutting forces. This rise in temperature at interface caused softening of the tool which leads to high wear. The tool wear is very sensitive to temperature variation and even a small change in temperature at the burr-bone interface can have a pronounced effect on the overall life of the tool.

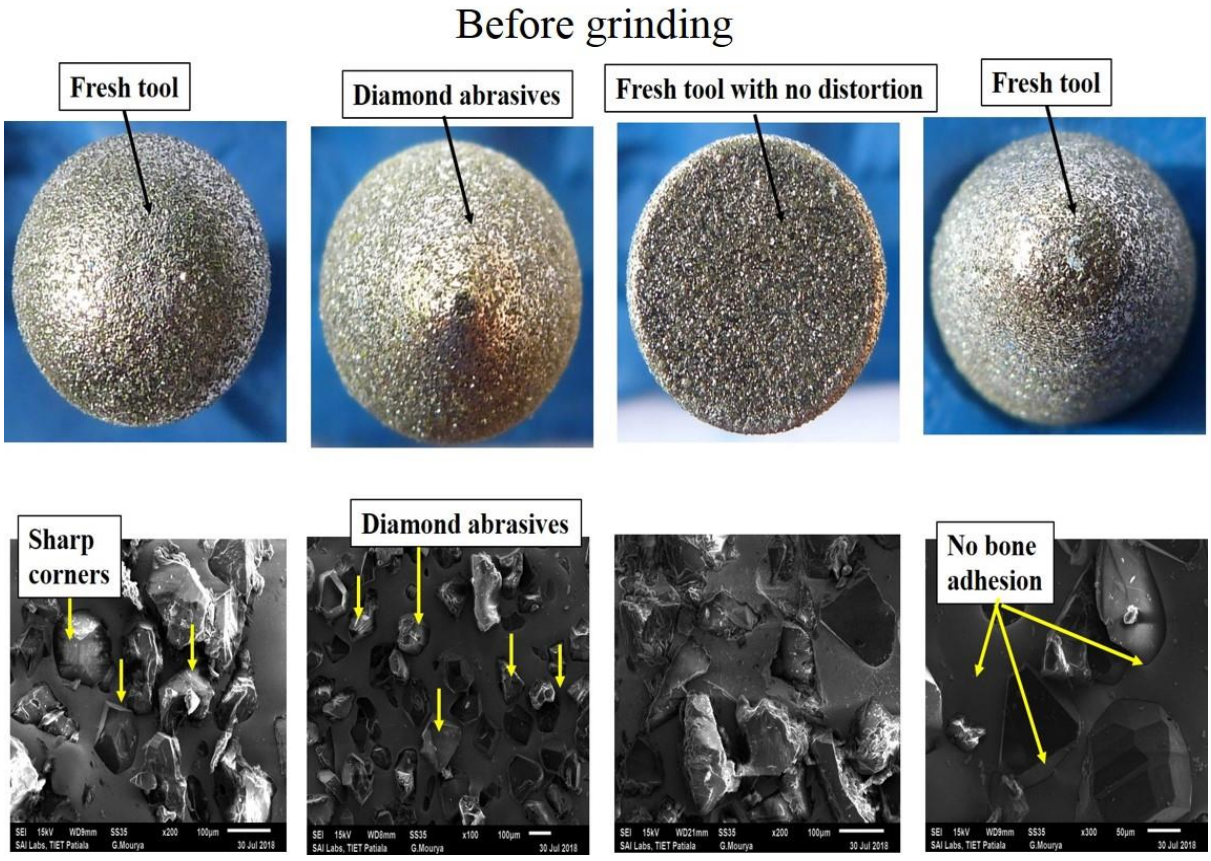

Figure 4.16: End face of different types of fresh tools and corresponding SEM pictures.

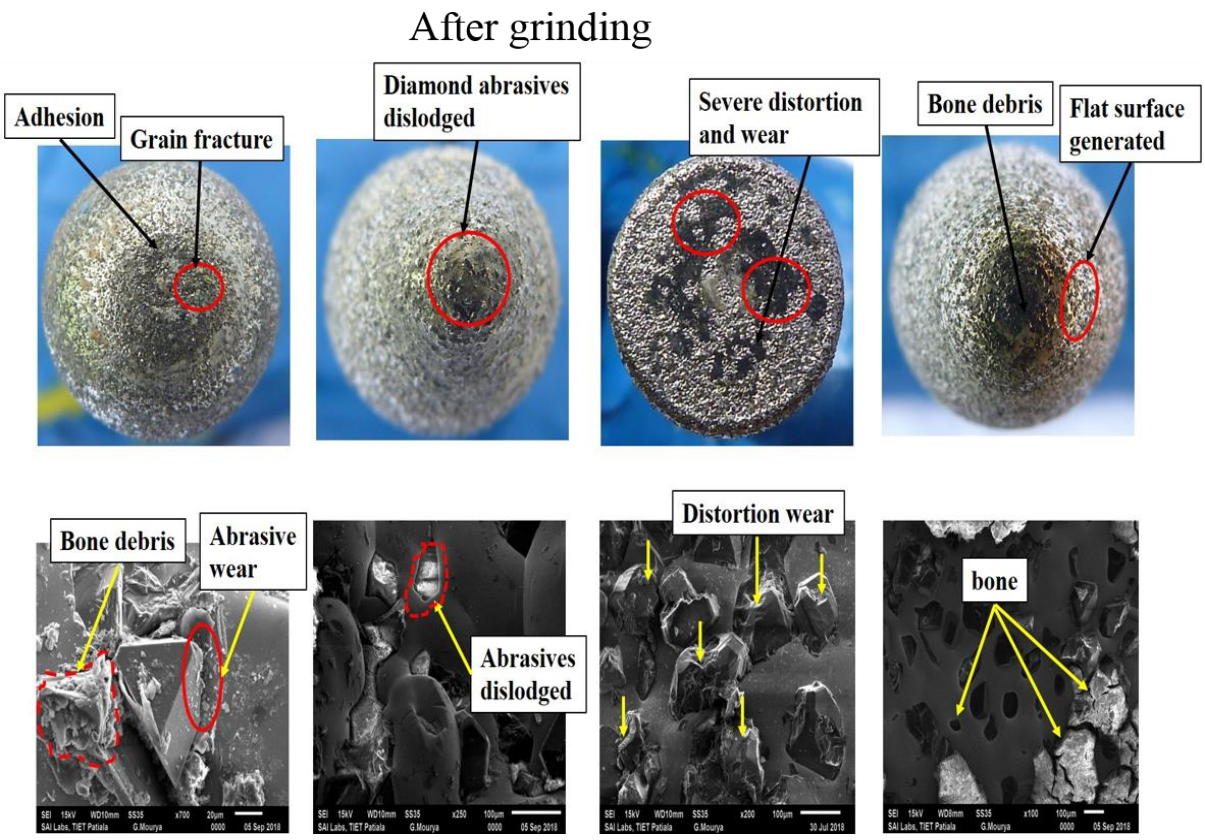

Figure 4.17: End face of different types of used tools and corresponding SEM pictures**.**

4.5.3 Quantification of W_{ab} & W_b

Consecutively, the weight loss (in %) between the fresh tool and used tool after grinding is accentuated in Table 4.5. A novel attempt is being made by the authors to quantify the tool loading by measuring the weight of the bone adhered to the burr during machining along with the weight of abrasives fragmented and removed from the burr.

The maximum 'W_b' observed in case of the spherical tool with weight 0.5907 gram while minimum in case of the convex tool with weight 0.1464 gram. Whereas 'W_b' for the cylindrical and tree-shaped tool is estimated as 0.2391 gram and 0.1964 gram respectively. The variation in the radius of curvature of the burr and stochastic nature leads to the different 'W_b' for each tool. Although the contact area is more in the cylindrical tool but due to the

excessive dislodging of abrasives at the end face the tool, the observed 'W_b' is less in comparison to the spherical tool.

Table 4.5. Quantification of burr loading and tool wear.

Tool no.	Tool type	The initial weight of tool (gram) W_i	The final weight of tool after grinding (gram) W_{f1}	Weight loss (in %) between a fresh tool and after grinding	Weight of tool after sonication (gram) W_{f2}	Weight of bone debris adhered to burr (gram) W_b	Weight of the abrasives removed from the burr (gram) W_{ab}
Tool 1 (T1)	Spherical tool	15.1247	14.7321	2.60	14.1414	0.5907	0.9833
Tool 2 (T2)	Convex tool	16.3312	16.0580	1.68	15.9116	0.1464	0.4196
Tool 3 (T3)	Cylindrical tool	21.8452	20.6988	5.25	20.4597	0.2391	1.3855
Tool 4 (T4)	Tree-shape tool	17.8426	17.4954	1.95	17.2990	0.1964	0.5436

Congruently, the maximum weight loss found for a cylindrical tool with 'W_{ab}' of 1.3855 gram during bone grinding. The convex shape tool has proved its utility with minimum percentage weight loss i.e. 1.68% with 0.1496 gram weight of abrasives dislodged over the burr's face. 'W_{ab}' for the spherical and tree-shape tool came out to be 0.9833 gram and 0.5436 gram respectively. The possible reason for better performance and minimum weight loss of convex tool is that the radius of curvature of the convex tool is comparatively less due to which less cutting and shearing forces exerts over the burr face and leads to lesser W_{ab}. On the other hand, the normal impact exerts over the end face of the cylindrical tool was more because of the more effective surface contact area.

The design of the tool including lateral and the end face of the tool should be optimized to reduce the fabrication cost and tool's wear because with a smaller lateral face, would require a lesser amount of abrasives for the impregnation over the face of the burr. Hence, after

analyzing the outcomes of tool wear in case of all four tools, it is recommended that the convex tool is superior to another shaped surgical grinding tool to achieve minimum tool wear. However, neurosurgeons find spherical diamond burr preferable for bone grinding owing to the fact that the pointed shape of the convex tool would generate more cutting forces which induce cracks in the bone; thereby, affecting the bone's regeneration ability and post-operative healing time.

4.6 SURFACE MORPHOLOGY OF BURR AFTER BONE GRINDING

Figure 4.18 shows the surface micrographs of the burr after grinding. Figure 4.18(a) shows the end face of the cylindrical tool after grinding. Figure 4.18 (b) depicts the micrograph of grain fracture at x500 magnification. Figure 4.18 (c) shows the enlarged image of an end face of tool indicating abrasive pull out (dislodging) after bone grinding at 1000x magnification.

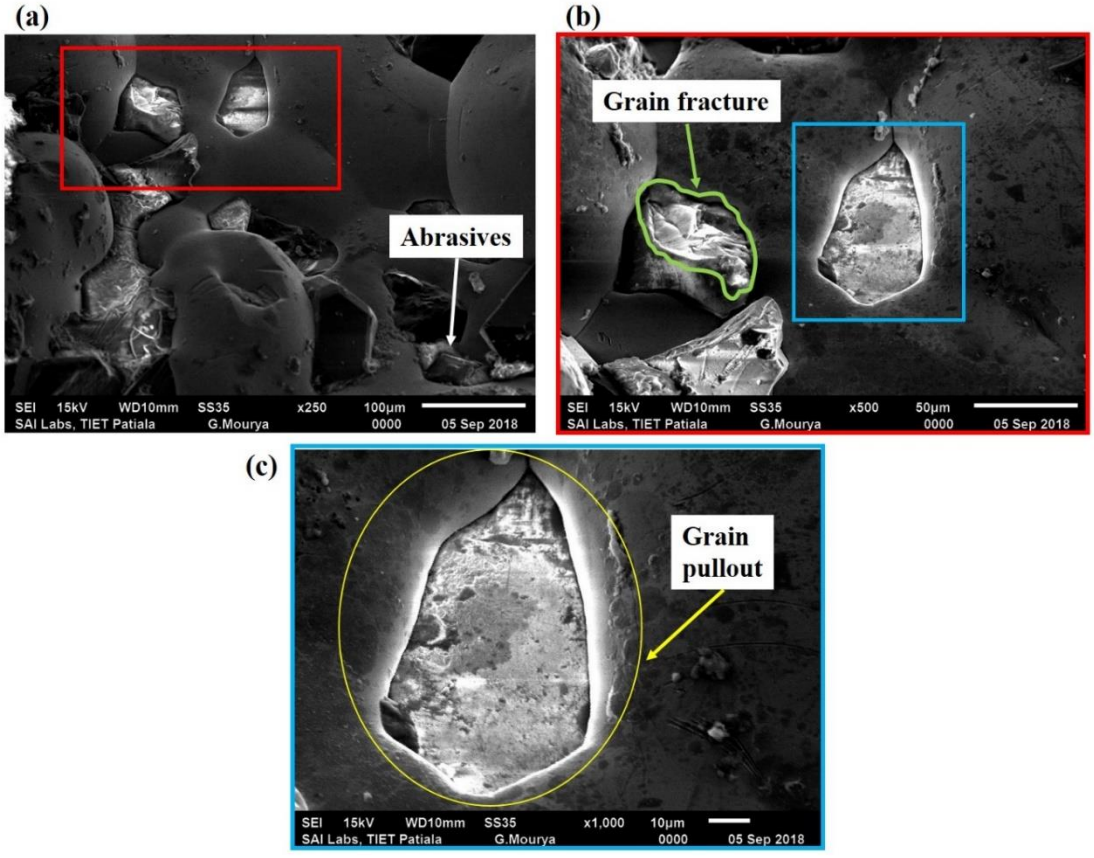

Figure 4.18: SEM micrographs showing tool wear after grinding at different magnifications (x250, x500, x1000): (a) end face of the cylindrical tool, (b) micrograph of Grain fracture at x500 magnification, (c) exaggerated image of an end face of tool indicating abrasive pullout (dislodging).

It was observed that abrasive grain gets flatten off and losses its sharp cutting edges which causes gran to fracture. Ultimately, abrasives were pulled out from their respective positions due to attrition wear and bond matrix failure as evidently in Figure 4.18(b) and enlarged view shown in Figure 4.18(c).

Figure 4.19 shows the micrographs of the burr at different magnifications at 50x and at 100x magnification. It is visible that burr loading occurred during grinding and bone debris gets settled within the diamond abrasives and thus affects the entire bone grinding operation. The bone chips owing to the heat and coolant gets agglomerated i.e. cluster of bone chips formed which adheres over the surface of grinding burr as shown in Figure 4.20. The cluster of bone chips has been shown for spherical grinding burr along with its micrographs and energy dispersive spectroscopy (EDS) which also confirms the presence of bone over the surface of grinding burr.

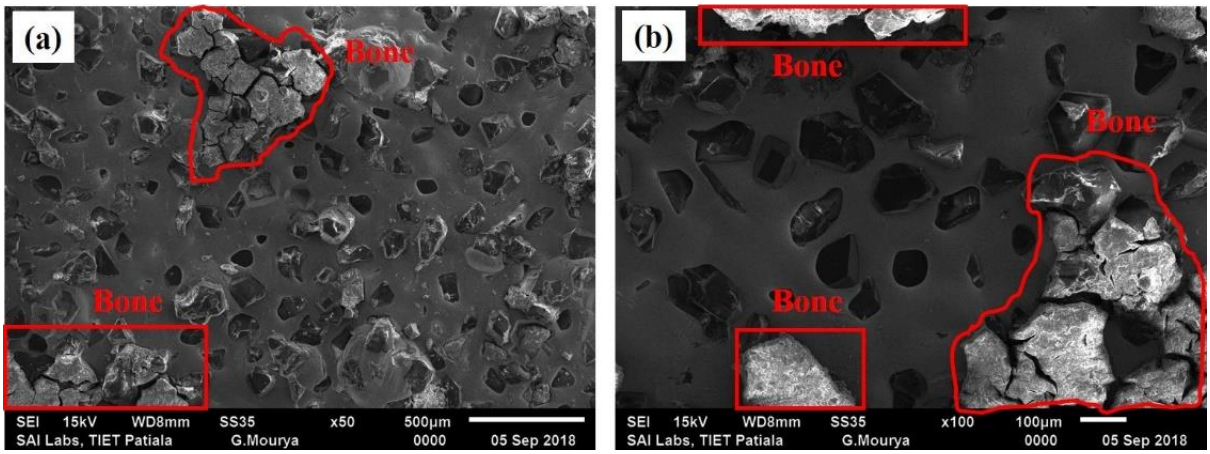

Figure 4.19: SEM images of burr lading at different magnifications: (a) at 50x and (b) at 100x (red colour highlights the bone settled in vacant space between successive abrasives).

EDS revealed that bone chips are settled within the successive grits over the tool's surface. The bone adhered over the surface of the tool might have influenced the cutting forces generated during bone grinding. Elemental mapping has been shown to highlight the major elements on the surface of burr (refer to Figure 4.21). The elements carbon (C), oxygen (O), calcium (Ca), and phosphorus (P) confirms that bone debris gets settled in the adjacent diamond abrasive particles. The nickel (Ni) has also been observed in the EDS since it was used as the base material for electroplating the diamond particles over the surface of the tool.

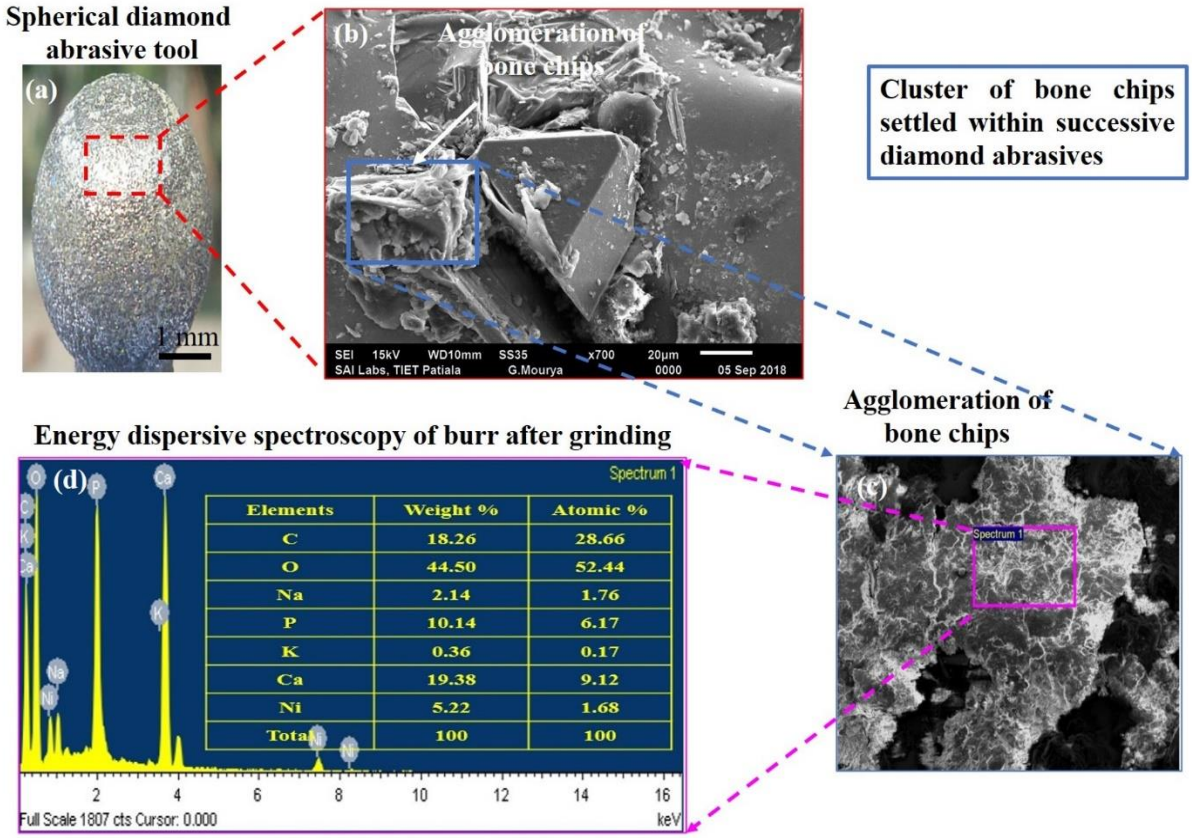

Figure 4.20: (a) Spherical burr, (b) SEM showing agglomeration of bone chips, (c) enlarged view of agglomeration, (d) EDS of the bone chip

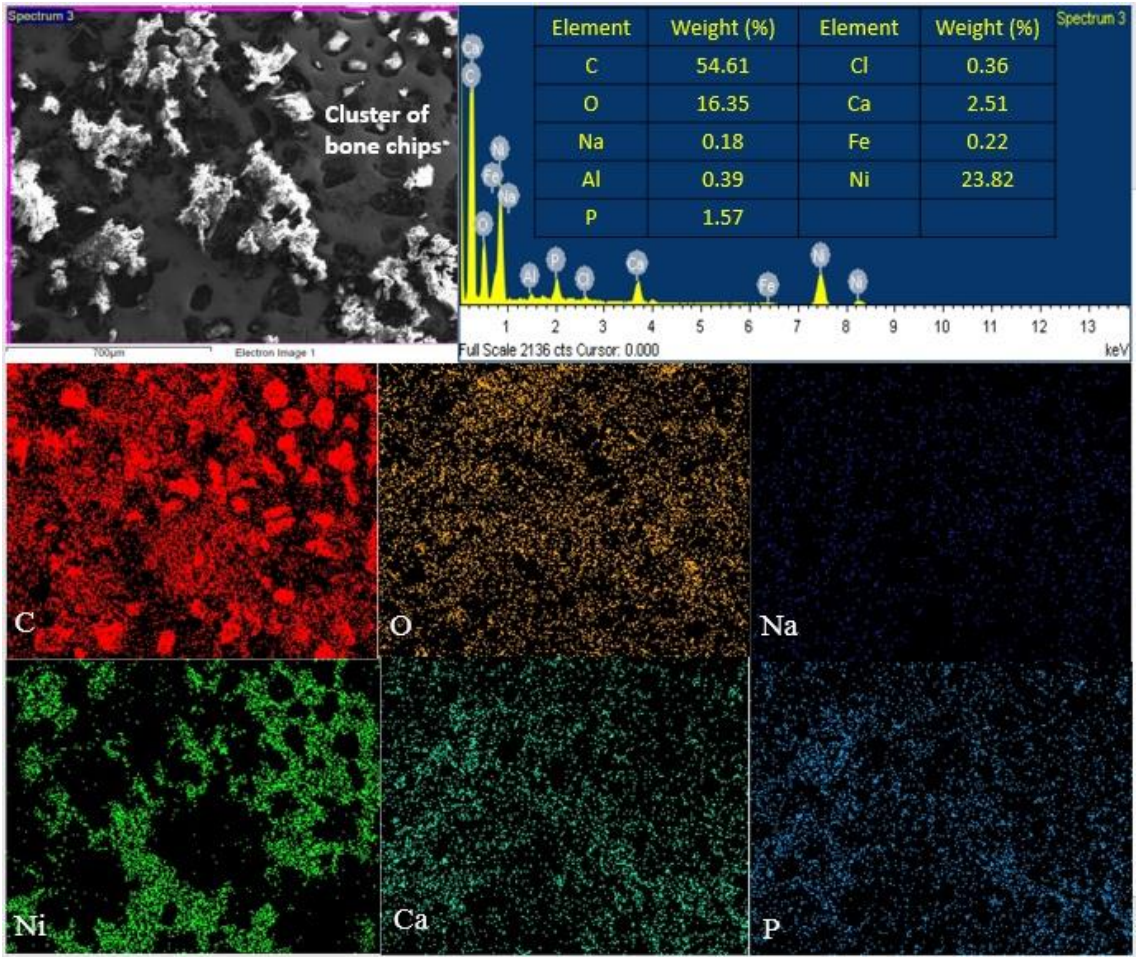

Figure 4.21: EDS spectrum of burr after grinding along with elemental mapping.

The EDS elemental mapping of the fresh tool confirms the absence of any calcium content which is the base element of bone. During an osteotomy, microchips were removed from the surface of the bone, some part of which flushed away with coolant and rest settled in between the adjacent diamond abrasives. The EDS spectrum of used burr after grinding confirms the presence of bone adhered over the surface of burr with the elemental composition C, O, Na, P, K, Ca, and Ni, as evidently in Figure 4.22(c-d), indicating a significant amount of calcium and phosphorous which is 19.38 % and 10.14 % respectively.

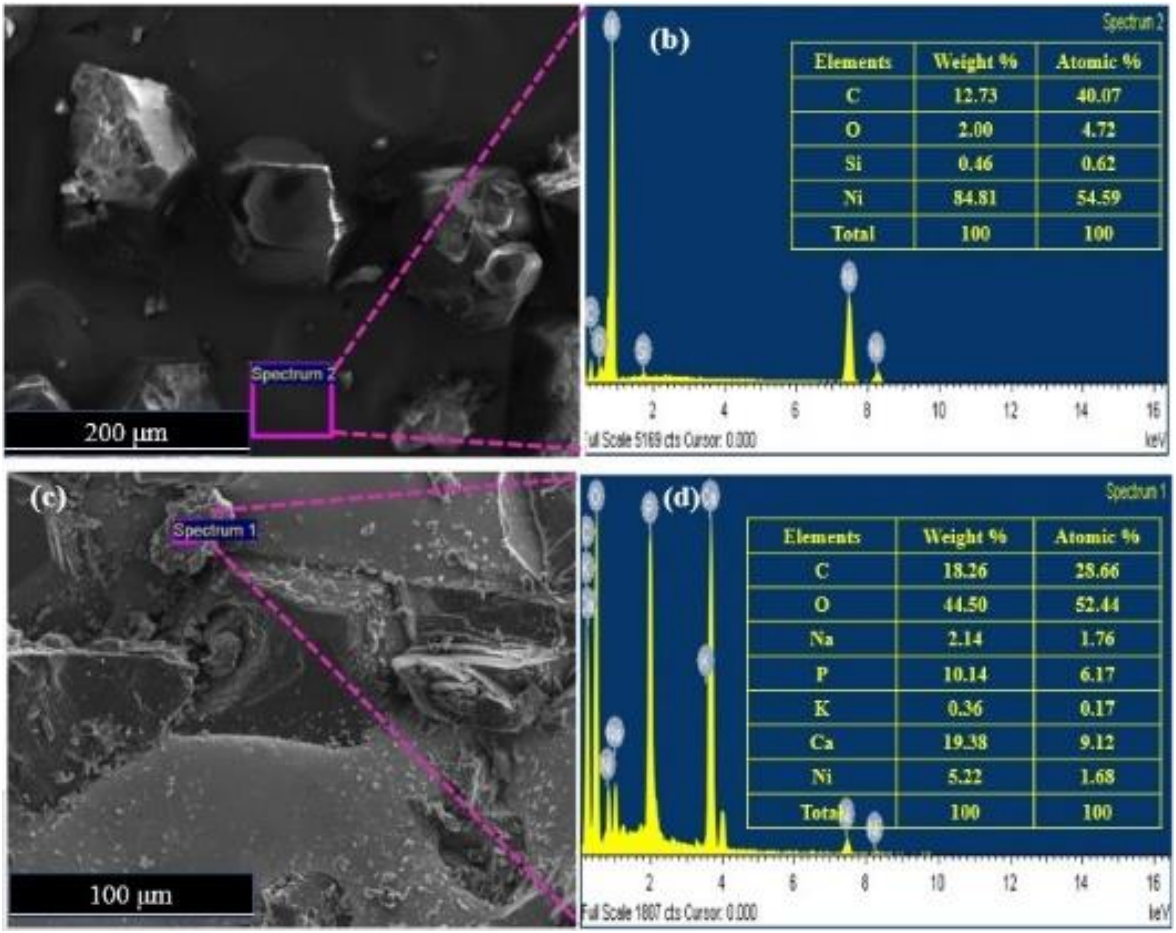

Figure 4.22: Elemental morphology of surgical burr (a-b) unused tool with no wear highlighting the Ni, C, Si, O as base alloy elements of bonding material and (c-d) tool after grinding which confirms the presence of bone debris between adjacent abrasives.

4.7 SURFACE MORPHOLOGY OF BONE AFTER GRINDING

During neurosurgical bone grinding, surgeons often use a variable feed rate in the range of 20-60 mm/min as per their rich clinical experience. To understand, the effect of varying feed rate in specified range on bone's quality after grinding, morphological analysis has been carried out. The surface morphology of the bone specimens after grinding was characterized using surface electron microscopy and micrographs obtained have been presented. Figure 4.23-4.25 illustrates the micrographs of specimens after bone grinding with different levels of feed rate i.e., 20, 40, and 60 mm/min at a constant rotational speed of 35000 rpm and depth of cut of 1.00 mm. Figure 4.23(a) shows the micrograph of a bone's specimen with the

rotational speed of 35000 rpm, a feed rate of 20 mm//min, and depth of cut of 1 mm at 200x magnification. The cutting streaks (highlighted with white arrow line) are seen in the micrograph which is produced on the bone's surface owing to the penetration of the diamond grits into the bone during grinding. Similarly, Figure 4.23(b) shows the cutting streaks as well as the microcracks on the surface of the bone after grinding. The enlarged view of the microcracks has also been shown. This is due to the existence of cutting forces which initiates the formation of the crack of the bone's surface during grinding.

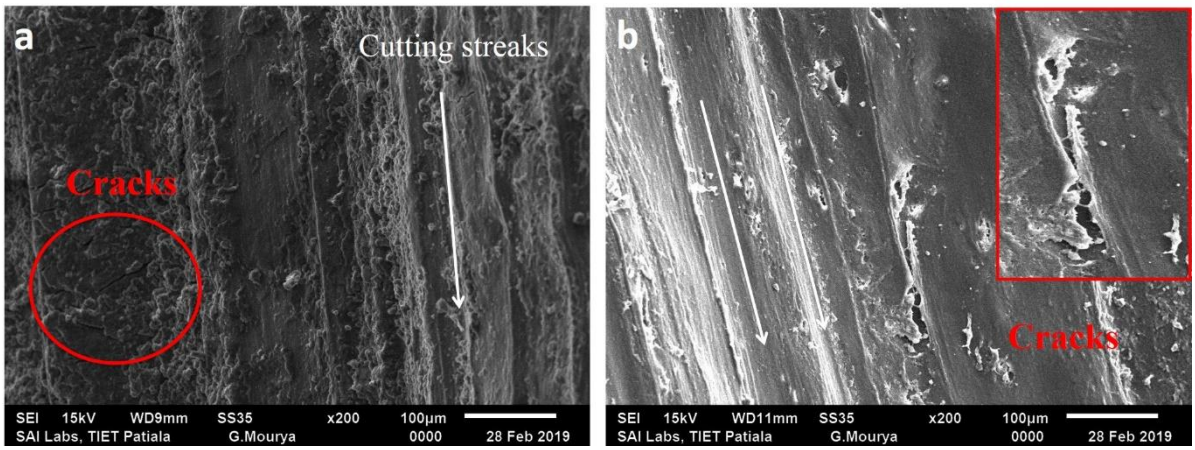

Figure 4.23: Micrographs of the after-bone grinding specimens at a magnification of 200x at 35000 rpm, 20 mm/min, 1.00 mm.

Figure 4.24 shows the micrograph with the rotational speed of 35000 rpm, a feed rate of 40 mm/min, and depth of cut of 1 mm. The delamination around the grinding site at the edge of the grinding zone is shown in Figure 4.24(a). It may be because the contact at the burr-bone interface is continuous during bone grinding which generates continuous chipping with a greater thickness which is not easily removed during drilling owing to lack of space at the burr-bone contact zone. Further, these chips degrade the bone's quality and result in delamination. The cutting streaks and microcracks generated on the bone's surface during skull bone grinding at 35000 rpm, 40 mm/min, and 1 mm. It may be because at higher feed rate, cutting chip thickness per revolution tool increases which cause more shear and frictional forces and leads to damage to the surface of the hole produced during drilling.

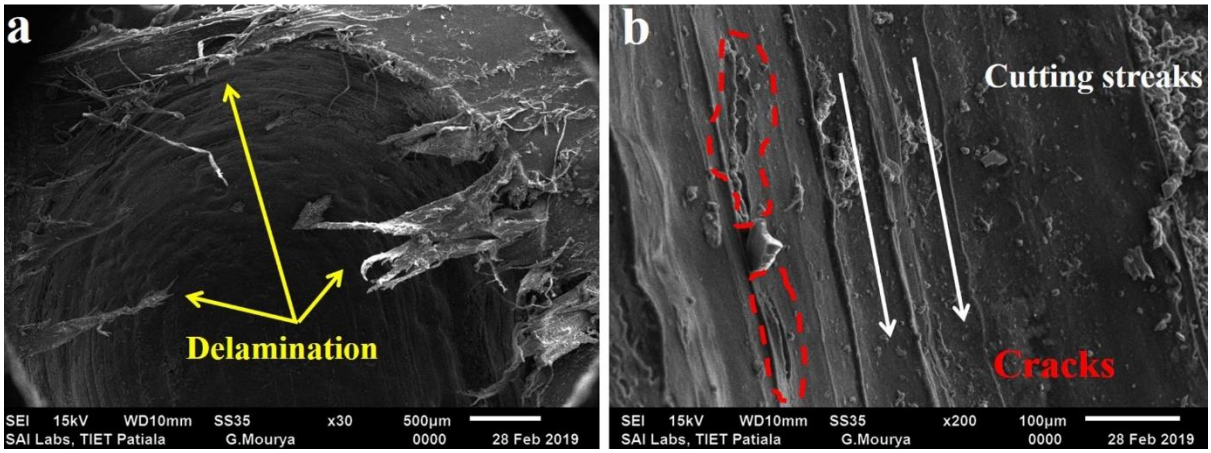

Figure 4.24: Micrographs of the bone specimens after grinding (a) magnification at 30x and (b) magnification at 200x at 35000 rpm, 40 mm/min, and 1 mm (red colour represents cracks on bone's surface and white colour signifies cutting steaks).

Figure 4.25 shows the micrographs for the rotational speed of 35000 rpm, a feed rate of 60 mm//min, and depth of cut of 1 mm at 1000x and 2000x magnification. At the higher level of feed rate i.e. 60 mm/min, severe cracks were reported as highlighted in Figure 4.25(b). The existence of such microcracks can affect the bone's regeneration ability and post-operative recovery time. These cracks are due to the existence of high cutting forces at a higher feed rate. The higher feed rate causes deeper cuts and more material is removed which substantially requires more shearing energy and cutting forces. Owing to this reason, the lower feed rate is recommended to perform neurosurgical bone grinding.

Figure 4.26 shows the micrographs of the bone specimens after grinding with RUNG process. It is visible that no surface cracks appeared on the bone during rotary ultrasonic neurosurgical grinding. It is expected that owing to intermittent contact of RUNG process no microcracks observed on the bone's surface at grinding site as well as on the adjacent region of the grinding path.

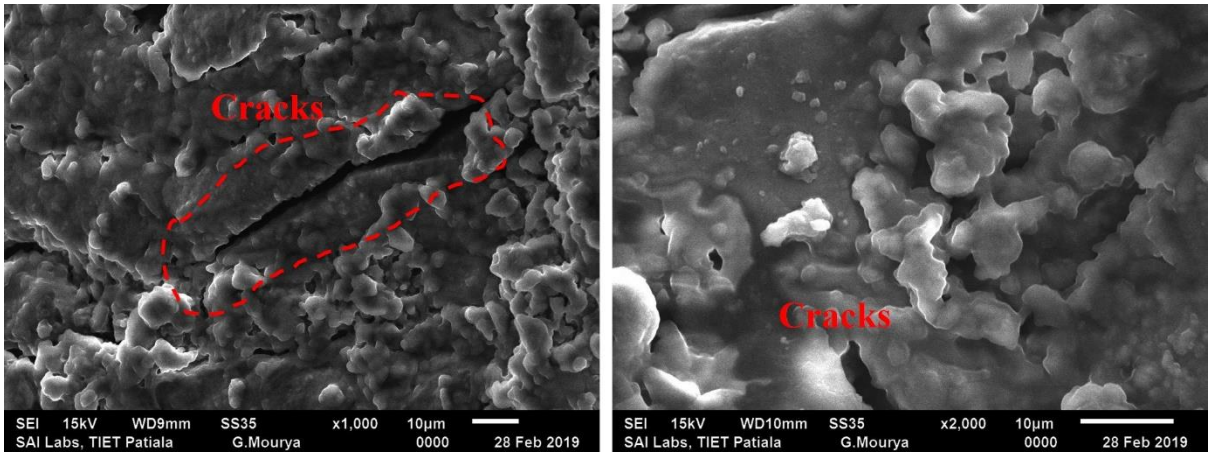

Figure 4.25: Micrographs of the bone specimens after grinding (a) at 1000x magnification (b) at 2000x magnification with at 35000 rpm, 60 mm/min, and 1.00 mm.

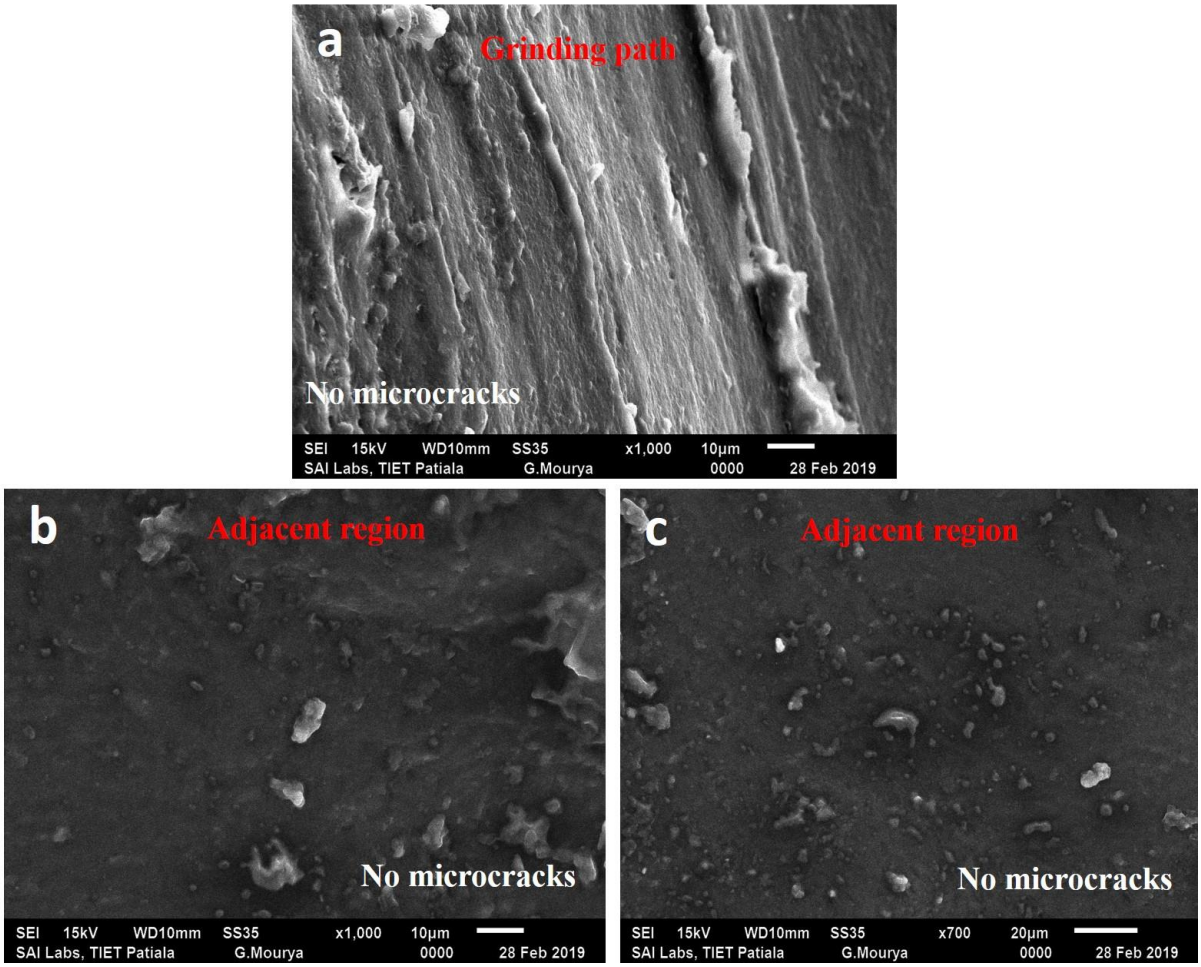

Figure 4.26: Micrographs of the bone specimens after RUNG grinding (a) at 1000x magnification of grinding path (b) at 1000x magnification of adjacent region (c) at 700x magnification of adjacent region with 35000 rpm, 20 mm/min, and 20 kHz.

4.8 SUMMARY

In this chapter, firstly the preliminary results reported for lower rotational speed based on CNC based experimental setup has been discussed. The temperature readings observed for the range of process parameters have been given along with the infrared thermograms. Furthermore, regression models have been developed and its precision and adequacy have also been evaluated. The effect of individual and interaction terms has been discussed duly supported with main effect plots and 3D interaction plots. Subsequently, the results reported for the higher rotational speed (up to 55k rpm) is provided for in-house developed pneumatic based ultrasonic bone grinding experimental setup. The results of the comparative study between CBG and RUNG has also been provided. The statistical analysis has been carried out to determine the significant process parameters and their relative percentage contribution. The individual and interactions parametric effect has been explained with suitable graphical plots. Then the results reported for the histopathology has been given duly supported with the histograms during CBG and RUNG.

Furthermore, the wear occurred on the lateral and end face of the tool has been discussed for different shape of the grinding burrs. The bone debris settled within the successive diamond abrasive grits have been discussed and corresponding surface micrographs have been presented. Furthermore, the abrasive wear and burr loading have been quantified for different shapes of the tools and consecutively the shape of the tool with maximum and minimum wear and loading have been decided. The cutting forces during the conventional bone grinding have been measured and further used to detail the effect of changing process parameters on the response characteristics. the temperature results observed during the conventional bone grinding has also been provided. The surface micrographs highlighting the impact of cutting force on cracks generation and propagation has been discussed along with the material removal mechanism.

CHAPTER 5: THERMAL DOSE MODEL AND SIMULATION

5.1. HYBRID THERMAL DOSE MODEL

The thermal tissue injury was evaluated using a hybrid thermal dose model based upon the CEM 43℃ and Arrhenius model. The extent of cell survival, coagulation necrosis, and thermal damage to the tissues is dependent upon the number of factors. For example, temperature elevation and duration of thermal exposure are two factors which determine the thermogenesis for a particular tissue. These factors can be merged into a single metric known as thermal dose. Thermal dose integrates the temperature over time to quantify the thermal effect on bone tissues in terms of cumulative equivalent minutes at 43°C i.e., CEM43°C. It is a normalizing method which generally refers to the minutes required to cause the same effect under constant heating at 43°C. The cell killing rate is always dependent on exposure time and temperature. It has been observed that sub-lethal damage is reported at a temperature of less than 43°C and with shorter exposure time. The rate of cell death at temperature <43°C is very low owing to the development of thermal tolerance. However, no thermal tolerance is noted when the temperature reaches above a threshold temperature of 43°C [78]. It has been reported that cell killing rate doubles for every degree rise in temperature above 43°C [77]. On another side, it reduces by a factor of four on every degree below 43°C [78]. Henriques F.C [85] formulated the Arrhenius model in 1947 to predict the extent of thermal damage using transient temperature solution for epithelial tissues. The same model was used to evaluate the time-temperature dependence on thermal damage with the following relations. Sapareto and Dewey [82] in 1984 proposed a model to convert a time-temperature relationship into an equivalent number of minutes. The integrated thermal dose model based on CEM43℃ and Arrhenius model has been shown in Figure 5.1.

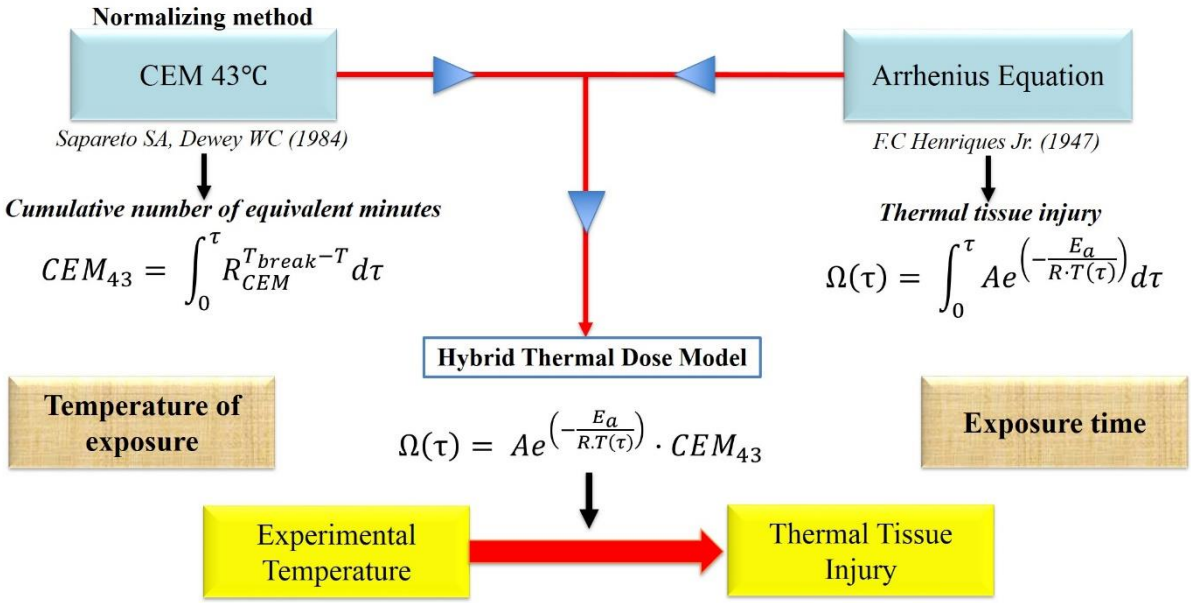

Figure 5.1: Hybrid thermal dose model for calculating thermal tissue injury.

CEM43℃ model:

$CEM_{43} = \int_0^\tau R_{CEM}^{T_{break}-T} d\tau$ ..... *eq. 5.1*

Arrhenius model:

$\Omega(\tau) = \int_0^\tau Ae^{\left(-\frac{E_a}{R \cdot T(t)}\right)} d\tau$..... *eq. 5.2*

and

$k = Ae^{\left(-\frac{E_a}{R \cdot T(\tau)}\right)}$ ..... *eq. 5.3*

Where,

R_{CEM} = Rate of cell death which is dependent upon temperature

If T ≤ 43°C, $R_{CEM} = 0.25$ i.e. equivalent time decreases by factor 4 per degree decrease in temperature.

If T > 43°C, $R_{CEM} = 0.50$ i.e. equivalent time doubles per degree rise in temperature.

Arrhenius constant A = 3.1×10^{98} s^{-1}

Activation energy E_a = 6.27×10^5 J/mol.

CEM 43℃ - Cumulative number of equivalent minutes at 43 ℃

Ω – Tissue damage function

τ – Time (seconds)

R – Universal gas constant (J/mol.k)

T_{break}– Breaking point temperature = 43 ℃

T – Exposure temperature

Taking natural logarithm on both sides of Eq. 5.3,

$$lnk = \ln Ae^{\left(-\frac{E_a}{R \cdot T(\tau)}\right)}$$

$$lnk = lnA + lne^{\left(-\frac{E_a}{R \cdot T(\tau)}\right)}$$

$$lnk = lnA - \frac{E_a}{RT}$$

$$lnk = -\frac{E_a}{R}\left(\frac{1}{T}\right) + lnA \quad \text{.....eq. 5.4}$$

Comparing with y = mx + c

$$y = lnk, \quad x = \frac{1}{T}, \quad m = -\frac{E_a}{R}$$

Algebraically, the activation energy can also be calculated by knowing the value of the rate constant (k) at two different temperatures can be calculated by the following equation.

$$\ln\left(\frac{k_1}{k_2}\right) = \frac{E_a}{R}\left(\frac{1}{T_2} - \frac{1}{T_1}\right) \quad \text{..... eq. 5.5}$$

Owing to the similar thermal response of the bone and epithelial tissues, the Arrhenius constants considered as A = 3.1×10^{98} s^{-1} and activation energy as E_a = 6.27×10^5 J/mol [80]. Here, A and E_a are constant parameters considered during estimation of thermal damage of epithelial tissues. Where, A is pre-exponential/frequency factor or Arrhenius constant for kinetic expression (s^{-1}) and is determined using a total number of collisions per second and E_a

is the activation energy for irreversible damage reaction (J/mol). This is determined during exothermic or endothermic chemical reactions and is the minimum energy that must be input to a chemical system with potential reactants to cause a chemical reaction. During each time-step of one second, the change in the 'Ω' has been considered as constant [79,84,85].

Using Eq. (5.1) and Eq. (5.2), we get

$$\Omega(\tau) = Ae^{\left(-\frac{E_a}{R.T(\tau)}\right)} \cdot CEM_{43} \quad \text{----------eq. 5.6}$$

The Equation (5.6), is further used to predict the tissue damage during conventional and ultrasonic-assisted bone grinding for the different set of parametric conditions.

5.2 BIOLOGICAL EFFECT EVALUATION

In this section, the biological effect of rising temperature on the bone tissues has been determined in terms of tissue damage function which is an integration of CEM43℃ into Arrhenius model. The decision, whether the tissue damage has occurred or not is made based on the value of tissue damage function for a particular set of parametric combination. Table 5.1 shows the threshold values of tissue damage function for different types of thermal injuries to the bone tissues which refers to the cell's killing and thermal damage to the osteons, viable and non-viable osteocytes. The corresponding biological condition based upon regarding the threshold levels has been tabulated in Table 5.2. A sample calculation can be seen in Appendix I.

Table 5.1. The biological condition of the bone cells at different tissue damage function.

Tissue damage function Ω	Threshold temperature (℃)	Biological condition
$\Omega < 0.00047$	Corresponding to 43℃	No tissue injury
$\Omega \geq 0.00047$	Corresponding to 43℃	Thermogenesis initiates
$\Omega \geq 0.00752$	Corresponding to 47℃	Osteonecrosis

Table 5.2: Cumulative equivalent minutes, thermal tissue injury, and biological effect valuation.

Run order	Temperature (℃)	Machining time (sec)	Machining time (mins)	CEM 43 (mins)	Thermal tissue damage Ω	Biological effect valuation
1	42.3	30	0.50	0.18946	8.90483E-05	No tissue damage
2	46.5	30	0.50	5.65685	0.002658721	Thermogenesis
3	47.5	30	0.50	11.31371	0.005317443	Thermogenesis
4	44.7	20	0.33	1.08300	0.000509012	Thermogenesis
5	44.3	30	0.50	1.23114	0.000578638	Thermogenesis
6	46.7	30	0.50	6.49802	0.003054069	Thermogenesis
7	41.5	60	1.00	0.12500	0.00005875	No tissue damage
8	42.6	60	1.00	0.57435	0.000269944	No tissue damage
9	44.6	60	1.00	3.03143	0.001424774	Thermogenesis
10	41.5	60	1.00	0.12500	0.00005875	No tissue damage
11	42.3	60	1.00	0.37893	0.000178097	No tissue damage
12	43.0	60	1.00	1.00000	0.00047	Thermogenesis
13	45.2	30	0.50	2.29739	0.001079776	Thermogenesis
14	42.3	60	1.00	0.37893	0.000178097	No tissue damage
15	45.2	20	0.33	1.53159	0.000719851	Thermogenesis
16	47.3	20	0.33	6.56610	0.003086069	Thermogenesis
17	45.7	60	1.00	6.49802	0.003054069	Thermogenesis
18	43.8	30	0.50	0.87055	0.000409159	No tissue damage
19	50.8	20	0.33	74.2869	0.034914881	Osteonecrosis
20	43.2	30	0.50	0.57435	0.000269944	No tissue damage
21	45.2	20	0.33	1.53159	0.000719851	Thermogenesis
22	47.3	20	0.33	6.56610	0.003086069	Thermogenesis
23	43.2	20	0.33	0.38289	0.000179963	No tissue damage
24	48.3	20	0.33	13.1322	0.006172137	Thermogenesis
25	49.5	20	0.33	30.16989	0.014179848	Osteonecrosis
26	44.8	30	0.50	1.74110	0.000818318	Thermogenesis
27	**38.8**	**60**	**1.00**	**0.00296**	**1.39138E-06**	**No tissue damage**

It has been revealed that no tissue damage has been reported for Experiment No. 1, 7, 8, 10, 11, 14, 18, 20, 23, and 27 since their tissue damage function value is less than 0.00047. However, thermal tissue injury in the form of thermogenesis and osteonecrosis has been reported for other sets of parametric combinations. Osteonecrosis has been observed for

Experiment No. 19 and 25 since the value of tissue damage function is greater than 0.00752. The optimum set of parameters for no thermal tissue injury and minimum temperature during bone grinding is 35000 rpm, 20 mm/min, and 20 kHz.

5.3 SIMULATION

The finite element 3D model of the bone was constructed in design modular of ANSYS software. The proposed simulation consists of three phases. In the first phase, a model of bone is constructed and suitable thermo-elastic properties are provided to the bone as shown in Table 5.3. The second phase involves simulating the temperature fields over the surface of the bone to visualize the spatial and temporal distribution of temperature. In the third phase, thermogenesis and osteonecrosis depth has been measured with the Axio Vision Rel. 4.8 software. The region considered for the simulation of the bone for predicting the depth of thermal necrosis has been shown in Figure 5.2. The primary objective of a finite element model is to measure the sub-surface temperature and thus the depth of thermogenesis and osteonecrosis. The limitation of using IR thermography is that it can only measure the surface's temperature and cannot measure the sub-surface temperature. Therefore, authors have used finite element model for the bone to measure the sub-surface temperature and depth of thermal trauma. If the surface is temperature is known then the sub-surface temperature can be determined using a finite element model. The bone has been considered as isotropic for simulation purpose instead of its anisotropic and heterogeneous nature. Since a rotating grinding burr can cut the fibres in all direction during its complete one revolution due to which anisotropic effect may not obvious to resultant characteristics. Numerous models in the past have also considered bone as the isotropic material for a reasonable estimation of the results [4,180,185–192].

Table 5.3. Thermo-elastic properties for the bone [14,162,193–199].

Thermal and elastic properties		
Thermal conductivity	W/mk	0.54
Elastic modulus	GPa	20
Poisson's ratio	–	0.36
Density	Kg/m^3	2260
Emissivity	–	0.96
Specific heat	J/KgK	1260
Heat capacity	J/m^3K	2.86×10^6

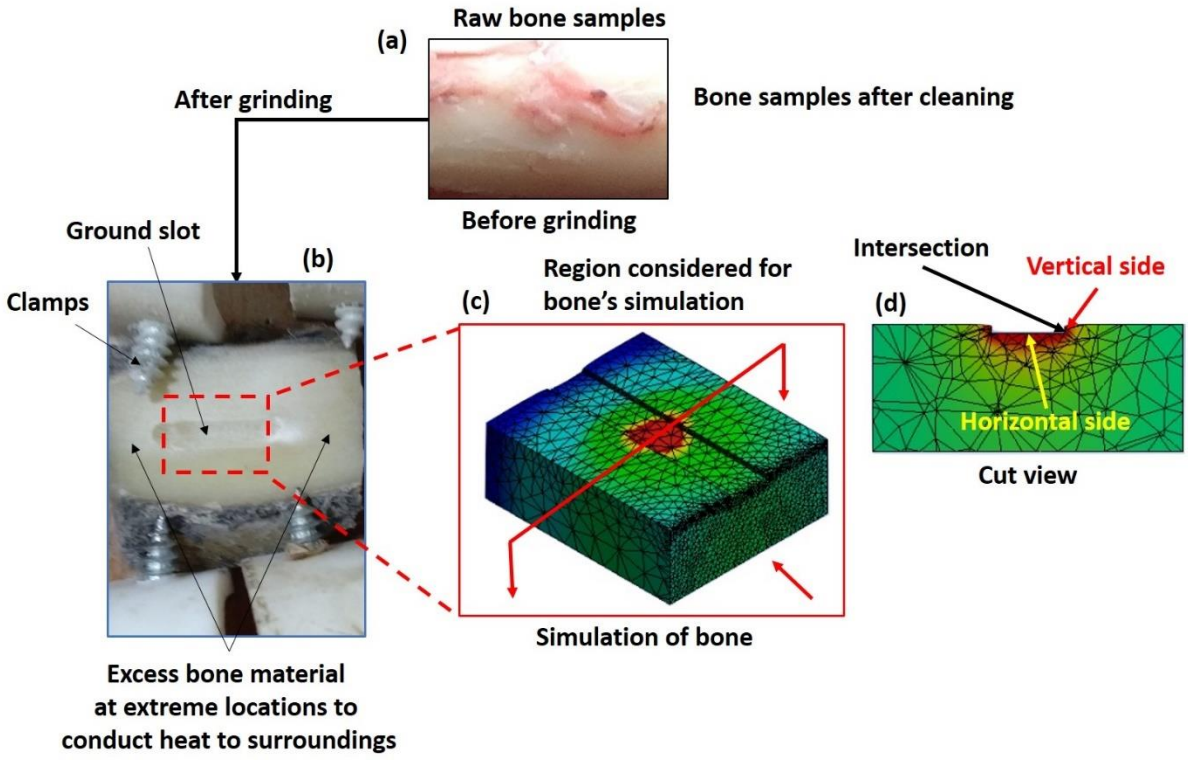

Figure 5.2: Real ground bone specimen: Inset (a) raw bone specimen; (b) actual bone sample after grinding; (c) region considered for simulation; (d) cut view of the simulated bone.

The simulation has been carried out under three dimensional steady-state thermal conditions in ANSYS 19.2 using available commercial code. The ambient temperature was approx. 37℃ and same has been considered as initial temperature of the bone specimen. The bottom surface of the bone was fixed. The "default" meshing was selected and radiation heat transfer

neglected since generated temperature levels were not too high. The temperature has been inserted over the surface of a bone at a particular instant what was observed during real experimental measurement. This thermal boundary condition acts as a heat source with a known temperature. Therefore, for a particular instant, the transfer of heat into the bone will be considered as constant (heat flow = constant) and this state will be considered as "Quasi steady-state". Hence, in the present study, temperature and thermal conductivity of the bone has been considered independent of the time.

The experimental temperature measured using infrared thermography for a different set of parametric combinations were applied over the surface of the bone to simulate the actual experimental temperature distribution. The spatial and temporal distribution of temperature for 5, 12, 19, 25 and 33 seconds have been demonstrated. As the grinding burr moves forward on the grinding path, the temperature also increases owing to the contact between burr and bone during experimentation. At 5 seconds, the temperature measured is 43.13℃ which rises to 59.35℃ at 33 seconds as shown in Figure 5.3.

The cross-section (cut) view of the corresponding grinding positions has been shown, as evidently in Figure 5.4. It shows that the region of thermal damage increases as the grinding continues. However, Figures 5.5-5.7 shows the cross-sectional cut view of the bone specimens along with a depth of thermal trauma during experiments 1 to 9, 10 to 18, and 19 to 27 respectively. The depth of thermogenesis corresponding to 43℃ and depth of osteonecrosis corresponding to 47℃ has been highlighted.

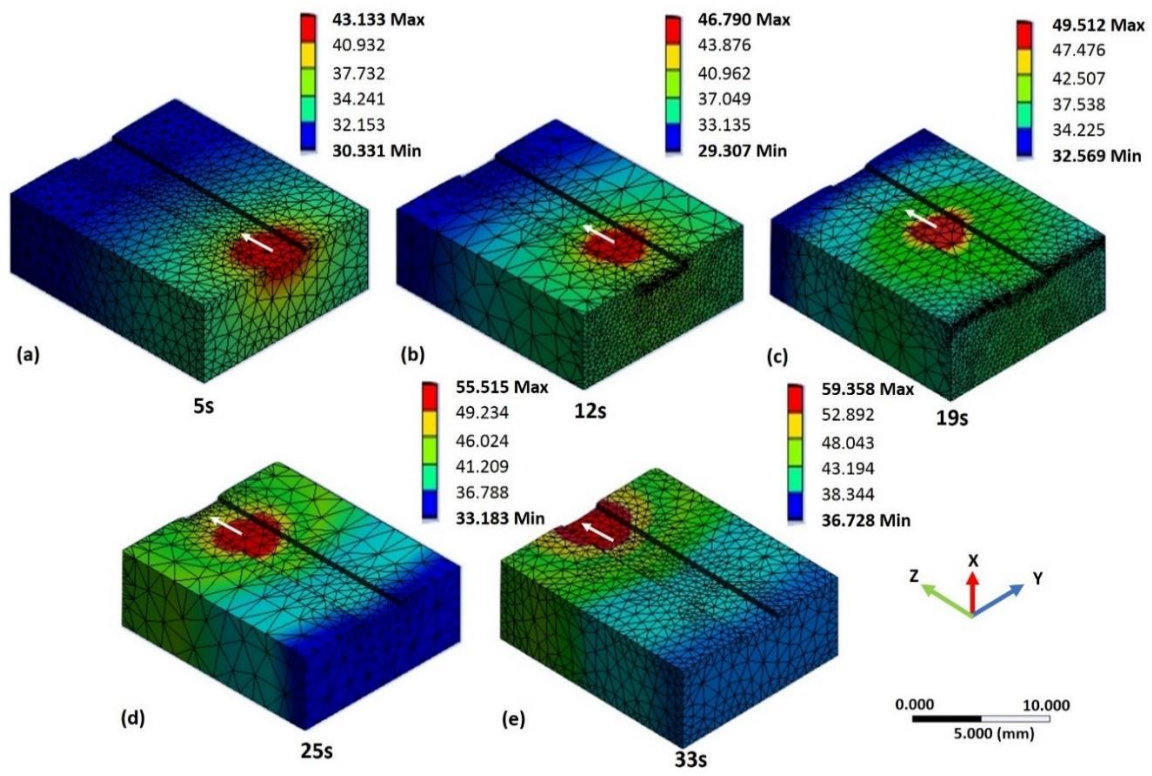

Figure 5.3: Spatial and temporal distribution of temperature on the bone at different grinding positions.

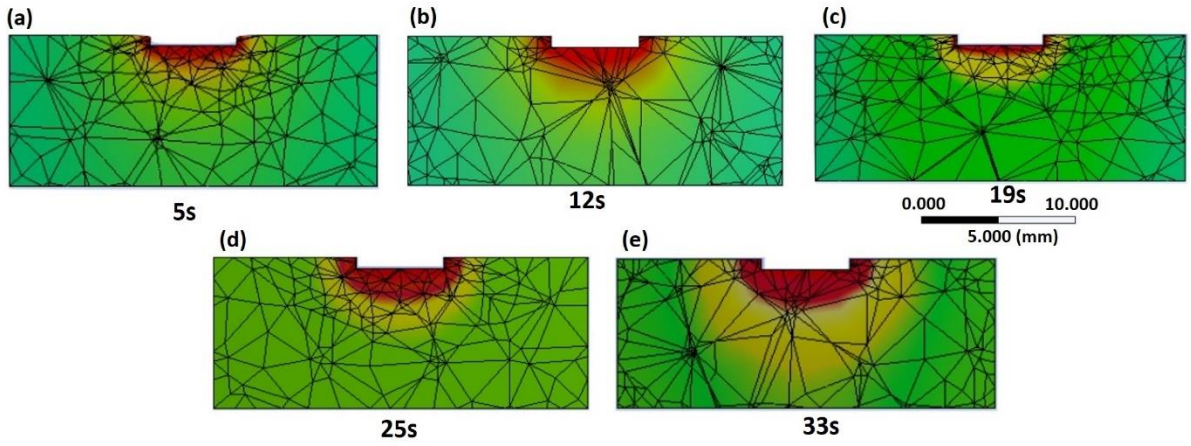

Figure 5.4: Cross-sectional cut view of the bone specimens at different grinding positions.

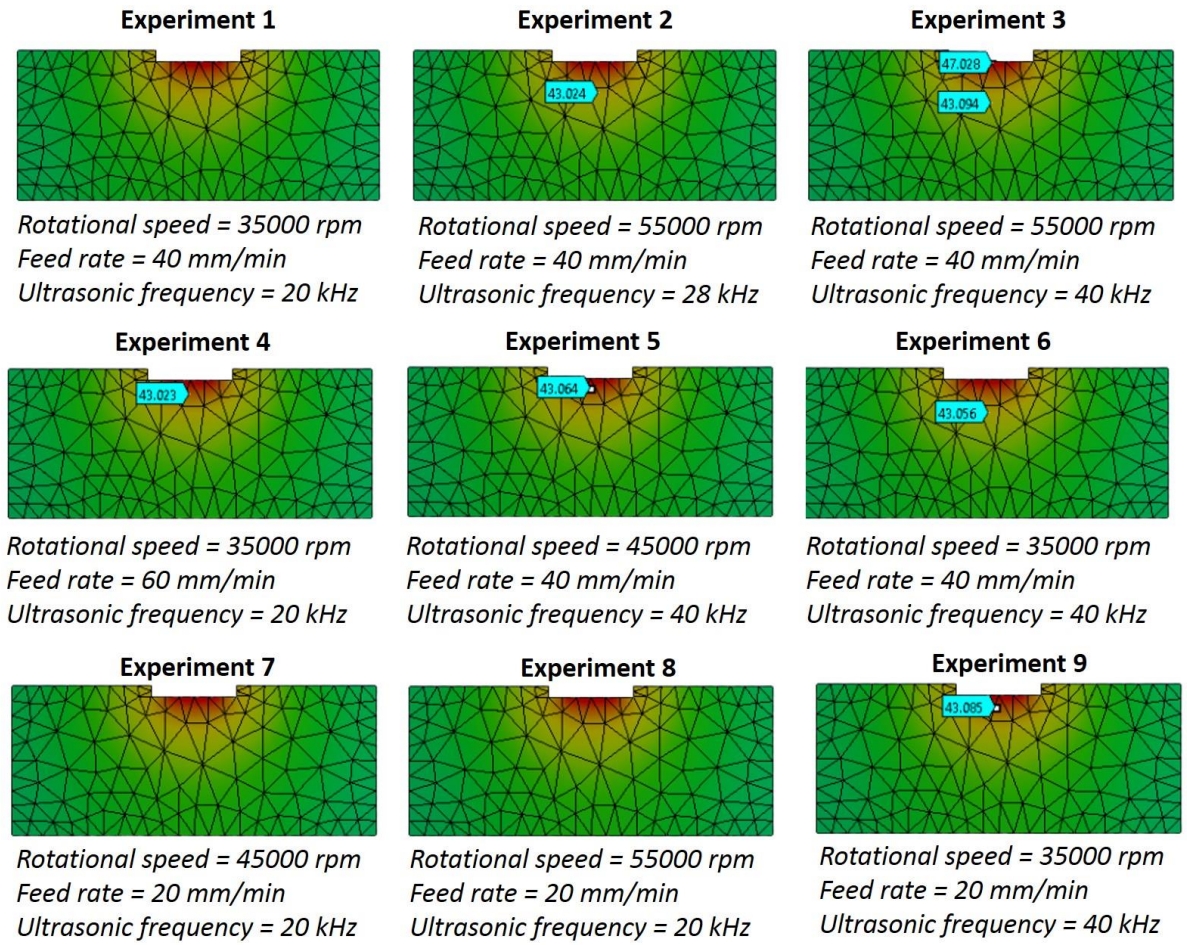

Figure 5.5: Cross-sectional cut view of the bone specimens during experiments 1 to 9.

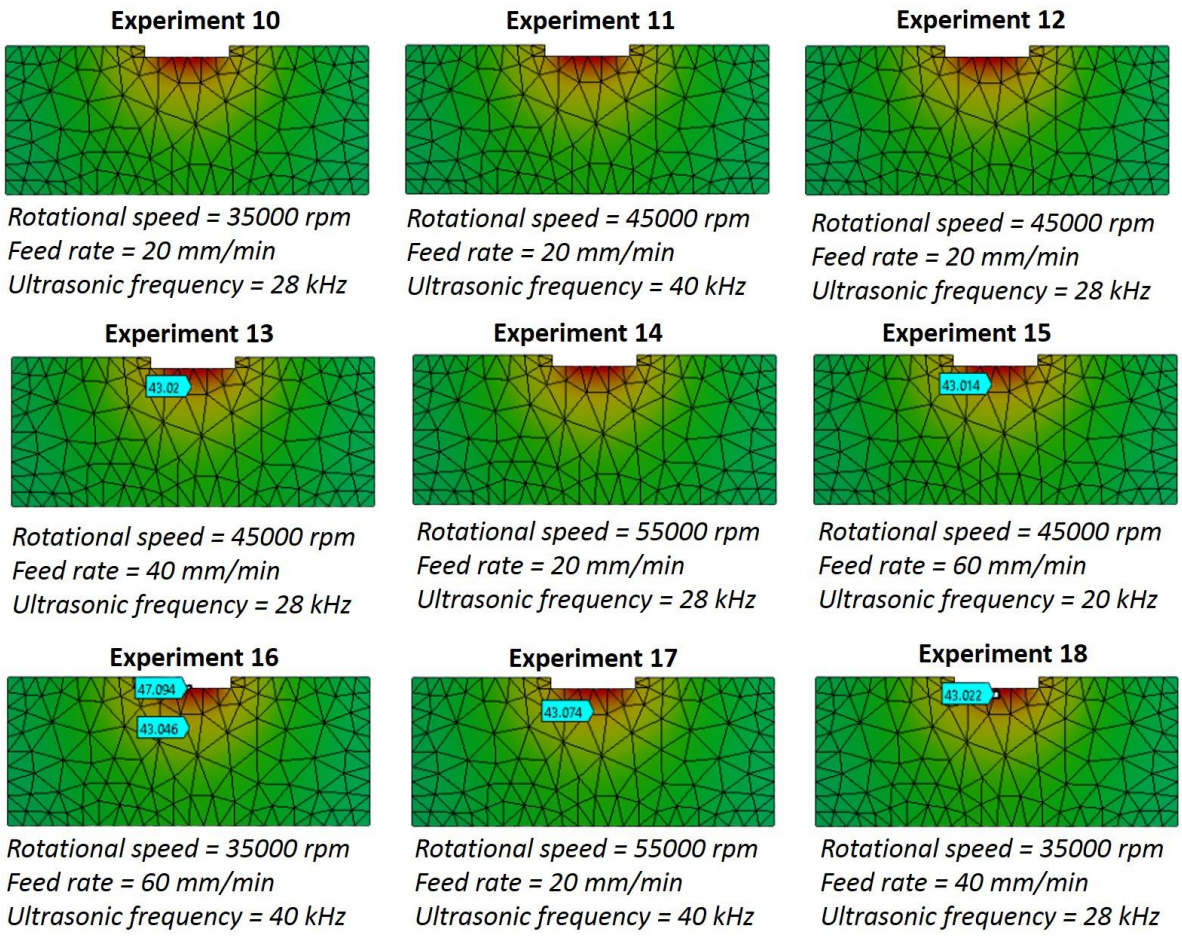

Figure 5.6: Cross-sectional cut view of the bone specimens during experiments 10 to 18.

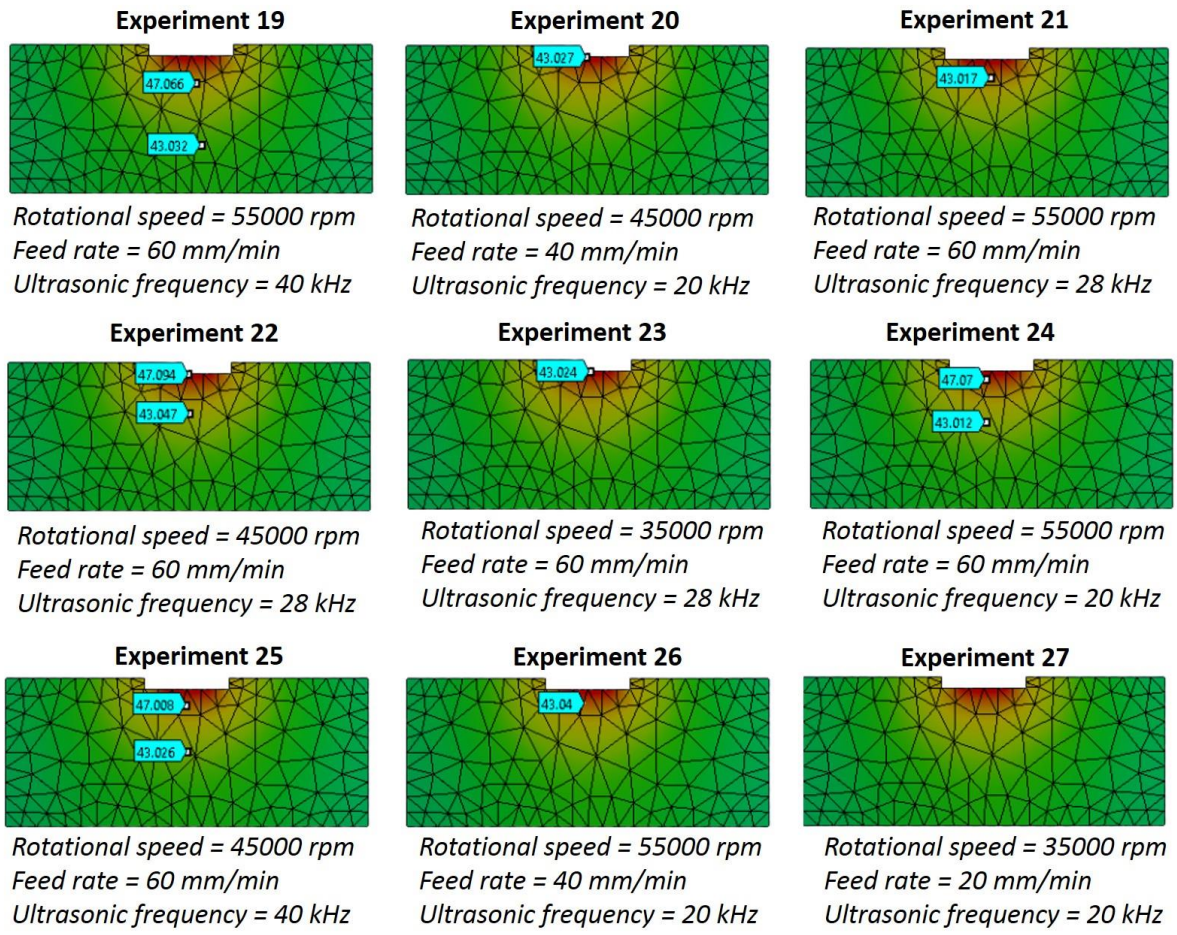

Figure 5.7: Cross-sectional cut view of the bone specimens during experiments 19 to 27.

5.4 MEASUREMENT OF THERMOGENESIS AND OSTEONECROSIS DEPTH

The estimation of the thermogenesis and osteonecrosis depth is important to determine the bone's quality and extent of thermal damage incurred in the bone owing to the heat generation during bone grinding. It was reported that thermogenesis tissue damage (heat-related injuries) initiates at the temperature of 43℃ [37,78,200]. However, osteonecrosis (irreversible damage to the bone/bone death) occurs at temperature ≥47℃ [16,19,201].

Figure 5.8 depicts the measurement of thermogenesis and osteonecrosis depth. The simulated results revealed that the parametric combination with a rotational speed of 55000 rpm, a feed rate of 60 mm/min, and the ultrasonic frequency of 40 kHz caused the maximum rise in temperature during bone grinding. Subsequently, the depth of thermogenesis and

osteonecrosis found to be 4.26 mm and 1.28 mm respectively for Experiment No. 19 with a temperature of 50.8℃. therefore, as the temperature is increased during bone grinding, the corresponding osteonecrosis and thermogenesis depth also increases and adversely affects the bone's regeneration ability. Similarly, the depth of thermogenesis and osteonecrosis was evaluated for other sets of parametric combinations which has been tabulated in Table 5.4

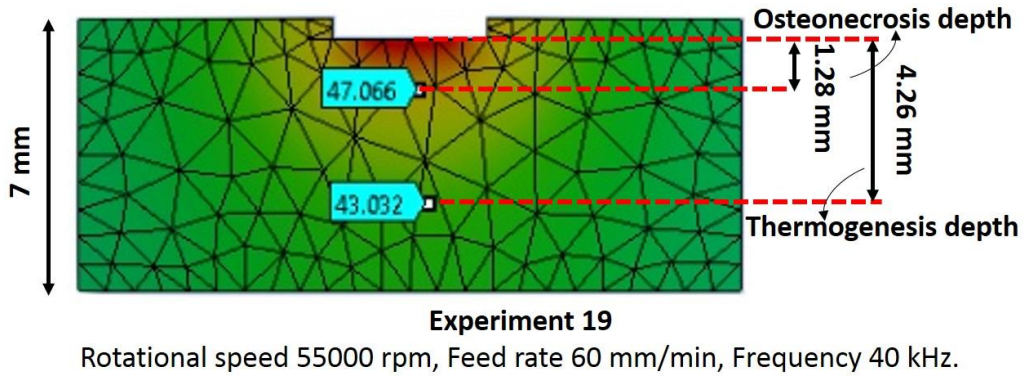

Figure 5.8: Illustration of osteonecrosis and thermogenesis depth.

Table 5.4. The measurements of the response characteristics temperature, CEM43℃, tissue damage function, and depth of thermal trauma.

Run order	Temperature (℃)	Change in temperature (ΔT)	Temperature (T) kelvin	Osteonecrosis depth (T≥47℃) mm	Thermogenesis Depth (T≥43℃) mm
1	42.3	5.3	315.45	–	–
2	46.5	9.5	319.65	–	1.44
3	47.5	10.5	320.65	0.16	1.97
4	44.7	7.7	317.85	–	0.64
5	44.3	7.3	317.45	–	0.43
6	46.7	9.7	319.85	–	1.54
7	41.5	4.5	314.65	–	–
8	42.6	5.6	315.75	–	–
9	44.6	7.6	317.75	–	0.59
10	41.5	4.5	314.65	–	–
11	42.3	5.3	315.45	–	–
12	43.0	6	316.15	–	–
13	45.2	8.2	318.35	–	0.85

14	42.3	5.3	315.45	–	–
15	45.2	8.2	318.35	–	0.85
16	47.3	10.3	320.45	0.11	1.86
17	45.7	8.7	318.85	–	1.06
18	43.8	6.8	316.95	–	0.27
19	50.8	13.8	323.95	1.28	4.26
20	43.2	6.2	316.35	–	0.11
21	45.2	8.2	318.35	–	0.80
22	47.3	10.3	320.45	0.11	2.02
23	43.2	6.2	316.35	–	0.11
24	48.3	11.3	321.45	0.43	2.50
25	49.5	12.5	322.65	0.74	2.93
26	44.8	7.8	317.95	–	0.64
27	38.8	1.8	311.95	–	–

Figure 5.9 shows bar plots for osteonecrosis and thermogenesis depth measured for a different set of parametric combinations. The results revealed that osteonecrosis occurs for Experiment No. 3, 16, 19, 22, 24, 25 and corresponding osteonecrosis depth is 0.16, 0.11, 1.28, 0.11, 0.43, and 0.74 mm respectively and corresponding readings of thermogenesis depth has been shown in Table 5.4.

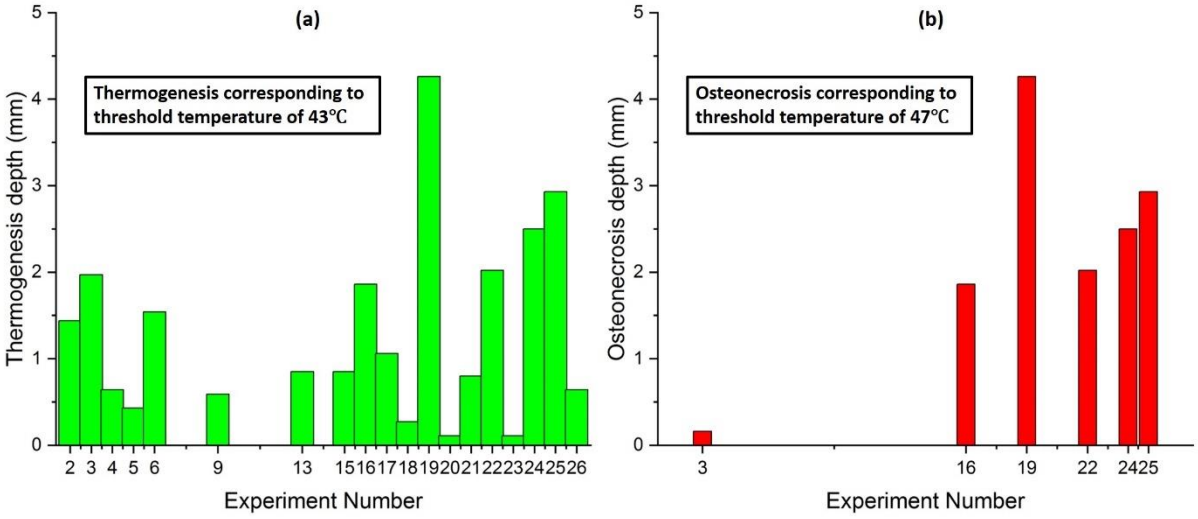

Figure 5.9: Measurements of thermogenesis and osteonecrosis depth for different grinding temperatures.

The maximum depth of thermogenesis and osteonecrosis was found at Experiment No. 19. However, no tissue damage and therefore, zero-depth of thermal trauma was reported for Experiment No. 27 with rotational speed 35000 rpm, feed rate 20 mm/min, and ultrasonic frequency of 20 kHz. The results produced by simulation, thermal dose model, and histopathology has been verified with each other and has been shown in Table 5.5.

Table 5.5. Verification of results during rotary ultrasonic neurosurgical bone grinding.

Exp. No.	Rotational speed (rpm)	Feed rate (mm/min)	Ultrasonic frequency (kHz)	Temperature (℃)	The density of viable lacunas using histopathology	Thermal tissue injury using a hybrid thermal dose model Ω	Simulation	
							Depth of osteonecrosis (mm)	Depth of thermogenesis (mm)
19	55000	60	40	50.8	Low	Osteonecrosis	1.28	4.26
27	35000	20	20	38.8	High	No tissue damage	–	–

5.5 SUMMARY

This chapter discusses the use of thermal dose model for predicting the tissue damage and cell necrosis. A thermal dose model has been developed by integrating the CEM43℃ and Arrhenius model. The temperature elevation and duration of thermal exposure are two factors which determine the thermogenesis for a particular tissue. These factors can be merged into a single metric known as thermal dose. Furthermore, the finite element model has been developed in ANSYS software and analysis has been used to determine the sub-surface temperature of the bone, provided the surface temperature is known. Subsequently, the sub-surface temperature is used to measure the depth of thermogenesis and osteonecrosis during bone grinding. Furthermore, the results have been verified with thermal dose model and histopathological analysis.

CHAPTER 6: CONCLUSIONS & FUTURE SCOPE

6.1 CONCLUSIONS

In this study, efforts have been made to address the problems and their potential solution related to the thermogenesis and osteonecrosis during neurosurgical bone grinding. The burr loading and tool wear was analysed for multi-shape tools during bone grinding. The influence of numerous input parameters on the response characteristics has been presented during the conventional and rotary ultrasonic grinding of bone. Subsequently, the optimum parameters were withdrawn to cause a minimum rise in the temperature during bone grinding to avoid thermal necrosis in bone and tissues as well. The results reported during RUNG were also compared with that of conventional bone grinding.

The histopathological analysis was carried out to evaluate the tissue damage reported in the bone during bone grinding with different parametric combinations. The thermal dose model based on a hybrid approach of CEM43℃ and Arrhenius model presented for predicting the degree of tissue damage during bone grinding owing to the rise in temperature. Subsequently, the model was experimentally validated and can be used by the other researchers for predicting the tissue damage in human beings during skull base grinding. The present strategy enables surgeons to treat tumors within less operative time and without thermal trauma. Furthermore, the sub-surface temperature during bone grinding was evaluated using the finite element model analysis. Subsequently, the depth of thermogenesis and osteonecrosis have been reported using the FE model.

The following results as evidence showed that the present strategies would be competent and capable to resolve the challenges like osteonecrosis and thermogenesis during bone grinding. Furthermore, the results reported have been substantially supported with the surface micrographs, histograms, and thermograms. Based on the results of the present findings, the following conclusion has been made.

- The optimum parametric condition for minimum temperature and to avoid thermal necrosis reported as

Rotational speed (rpm)	Feed rate (mm/min)	Ultrasonic frequency (kHz)
35000	20	20

- Experimental and statistical analysis showed that the rotational speed, feed rate, and ultrasonic frequency are significant parameters and caused an increase in the temperature, thereby, affecting the cell's viability at the grinding site.
- Statistical analysis revealed that feed rate (45.43%) has the highest influence on temperature rise during bone grinding followed by ultrasonic frequency (23.87%) and rotational speed with (12.85%) contribution towards response variable.
- Histopathological results indicate that the occurrence of bone damage was significantly influenced by the grinding temperature. The histogram obtained for the lower levels is better than the histogram which had a higher grinding temperature, in terms of the viable osteocytes (filled lacunas) which signifies a sign of reduced bone damage.
- Morphological analysis of the bone revealed that the higher feed rate leads to the initiation and propagation of the microcracks over the surface of the bone. Morphological analysis of the tool showed grain pullout, abrasive fracture, and adhesion of bone debris within the successive diamond abrasives.
- It has been revealed that the higher levels of input parameters can adversely affect bone's quality and its post-operative regeneration ability owing to increased temperature. Experimental data revealed that less temperature is generated in RUNG in comparison to the CBG.

- It has been observed that the convex-shaped tool possessed lesser tool to wear in comparison to all other tools and cylindrical tool caused a higher amount of tool wear among all tools. The maximum weight of bone debris adhered over spherical burr i.e. 0.5907 gram and weight of bone adhered over convex, cylindrical, and tree-shape tool is 0.1464 gram (minimum), 0.2391 gram, and 0.1964 gram respectively.
- The maximum increase in the tangential force is observed as 22.11 N for rotational speed 35000 rpm, a feed rate of 60 mm/min, and depth of cut of 1.00 mm. However, the minimum tangential force found to be 14.68 N for 55000 rpm, 20 mm/min, and 0.50 mm depth of grinding.
- The maximum increase in the thrust force is observed as 9.88 N for 35000 rpm, 60 mm/min, and 1.00 mm. On another side, minimum thrust force found to be 5.26 N for 55000 rpm, 20 mm/min, and 0.50 mm.
- The maximum increase in the torque is observed as 4.55 N-mm for 35000 rpm, 60 mm/min, and 1.00 mm. Whereas, minimum torque found to be 0.70 N-mm for 55000 rpm, 20 mm/min, and 0.50 mm. Therefore, it has been found that cutting forces decrease by increasing the rotational speed and increases on increasing the feed rate.
- Hybrid thermal dose model based upon CEM43℃ and Arrhenius model has successfully estimated the thermal tissue injury for a different set of unique parametric combinations which have been found in line with histopathological and simulation results.
- It has been revealed that No tissue damage has been reported for Experiment No. 1, 7, 8, 10, 11, 14, 18, 20, 23, and 27. However, thermal tissue injury has been reported for other sets of parametric combinations.

- The sub-surface temperature at the grinding site during the bone grinding has been successfully determined using the simulation method; thereby, the depth of thermogenesis and osteonecrosis in the bone.
- The maximum depth of thermogenesis and osteonecrosis found to be 1.28 and 4.26 mm respectively for the rotational speed of 55000 rpm, a feed rate of 60 mm/min, and frequency of 40 kHz. However, zero-depth of thermal trauma is reported for the rotational speed of 35000 rpm, a feed rate of 20 mm/min, and a frequency of 20 kHz.

6.2 FUTURE SCOPE

The following are the scopes of future work which could be deployed in the future endeavor:

- Using rotary ultrasonic neurosurgical bone grinding setup of human skull instead of animal skull to achieve more reliable results.
- In future work, tool with some other specification could be used which have different abrasive type, abrasive structure, bond, shape of abrasives such as conical, rectangular,

  spherical etc.
- A video study using very high frame rate (10^5 frame/s) camera can be done. This will help to further improve the ultrasonic assisted drilling process and help to develop a FE model based on the segmented chip formation.
- The effect of different cooling techniques such as mist cooling and nanoparticle jet mist cooling can be explored for temperature rise during bone grinding.
- In present study, In-vitro experimentation was carried out. However, real time experimental conditions can be generated and check the behavior of grinding technique and parameters directly to the In-vivo conditions.

- Mathematical modeling to predict the thermal and mechanical damage in case of rotary ultrasonic neurosurgical bone grinding can be the topic of further study in this field.

REFERENCES

[1] Kumar A, Shitole P, Ghosh R, Kumar R, Gupta A. Experimental and numerical comparisons between finite element method, element-free Galerkin method, and extended finite element method predicted stress intensity factor and energy release rate of cortical bone considering anisotropic bone modelling. Proc Inst Mech Eng Part H J Eng Med 2019. https://doi.org/10.1177/0954411919853918.

[2] Wang W, Shi Y, Yang N, Yuan X. Experimental analysis of drilling process in cortical bone. Med Eng Phys 2014;36:261–6. https://doi.org/10.1016/j.medengphy.2013.08.006.

[3] Gao C, Peng S, Feng P, Shuai C. Bone biomaterials and interactions with stem cells. Bone Res 2017;5:17059. https://doi.org/10.1038/boneres.2017.59.

[4] Marco M, Rodríguez-Millán M, Santiuste C, Giner E, Henar Miguélez M. A review on recent advances in numerical modelling of bone cutting. J Mech Behav Biomed Mater 2015;44:179–201. https://doi.org/10.1016/j.jmbbm.2014.12.006.

[5] Shitole P, Gupta A, Ghosh R. Fracture mechanism and fracture toughness at the interface between cortical and cancellous bone. J Biomech Eng 2019. https://doi.org/10.1115/1.4044093.

[6] Olson EJ, Carlson CS. Bones, Joints, Tendons, and Ligaments. Pathol. Basis Vet. Dis., Elsevier; 2017, p. 954-1008.e2. https://doi.org/10.1016/B978-0-323-35775-3.00016-3.

[7] Singh G, Jain V, Gupta D, Sharma A. Parametric effect of vibrational drilling on osteonecrosis and comparative histopathology study with conventional drilling of cortical bone. Proc Inst Mech Eng Part H J Eng Med 2018;232:975–86. https://doi.org/10.1177/0954411918794983.

[8] Singh G, Jain V, Gupta D, Ghai A. Optimization of process parameters for drilled hole quality characteristics during cortical bone drilling using Taguchi method. J Mech Behav Biomed Mater 2016;62:355–65. https://doi.org/10.1016/j.jmbbm.2016.05.015.

[9] Feldmann A, Wili P, Maquer G, Zysset P. The thermal conductivity of cortical and cancellous bone. Eur Cells Mater 2018;35:25–33. https://doi.org/10.22203/eCM.v035a03.

[10] Poumarat G, Squire P. Comparison of mechanical properties of human, bovine bone and a new processed bone xenograft. Biomaterials 1993;14:337–40.

https://doi.org/10.1016/0142-9612(93)90051-3.

[11] Yang M, Li C, Zhang Y, Jia D, Zhang X, Hou Y, et al. Microscale bone grinding temperature by dynamic heat flux in nanoparticle jet mist cooling with different particle sizes. Mater Manuf Process 2018;33:58–68. https://doi.org/10.1080/10426914.2016.1244846.

[12] Reilly DT, Burstein AH, Frankel VH. The elastic modulus for bone. J Biomech 1974;7:271–5. https://doi.org/10.1016/0021-9290(74)90018-9.

[13] Rho JY, Ashman RB, Turner CH. Young's modulus of trabecular and cortical bone material: Ultrasonic and microtensile measurements. J Biomech 1993;26:111–9. https://doi.org/10.1016/0021-9290(93)90042-D.

[14] Feldmann A, Zysset P. Experimental determination of the emissivity of bone. Med Eng Phys 2016;38:1136–8. https://doi.org/10.1016/j.medengphy.2016.06.019.

[15] Biyikli S, Modest MF, Tarr R. Measurements of thermal properties for human femora. J Biomed Mater Res 1986;20:1335–45. https://doi.org/10.1002/jbm.820200908.

[16] Tai BL, Zhang L, Wang AC, Sullivan S, Wang G, Shih AJ. Temperature prediction in high speed bone grinding using motor PWM signal. Med Eng Phys 2013;35:1545–9. https://doi.org/10.1016/j.medengphy.2013.05.011.

[17] Babbar A, Jain V, Gupta D. Preliminary investigations of rotary ultrasonic neurosurgical bone grinding using Grey-Taguchi optimization methodology. Grey Syst Theory Appl 2020;10:479–93. https://doi.org/10.1108/GS-11-2019-0054.

[18] Nogueira JF, Stamm A, Vellutini E. Evolution of Endoscopic Skull Base Surgery, Current Concepts, and Future Perspectives. Otolaryngol Clin North Am 2010;43:639–52. https://doi.org/10.1016/j.otc.2010.02.017.

[19] Zhang L, Tai BL, Wang G, Zhang K, Sullivan S, Shih AJ. Thermal model to investigate the temperature in bone grinding for skull base neurosurgery. Med Eng Phys 2013;35:1391–8. https://doi.org/10.1016/j.medengphy.2013.03.023.

[20] Cappabianca P, Cavallo LM, de Divitiis E. Endoscopic Endonasal Transsphenoidal Surgery. Neurosurgery 2004;55:933–41. https://doi.org/10.1227/01.NEU.0000137330.02549.0D.

[21] Call WH. Thermal injury from mastoid bone burrs. Ann Otol Rhinol Laryngol 1978;87:43–9. https://doi.org/10.1177/000348947808700109.

[22] Aslan A, Vatansever HS, Aslan GG, Eskiizmir G, Giray G. Effect of thermal energy produced by drilling on the facial nerve: Histopathologic evaluation in guinea pigs. J Laryngol Otol 2005;119:600–5. https://doi.org/10.1258/0022215054516250.

[23] Jimenez Hamann MC, Sacks MS, Malinin TI. Quantification of the collagen fibre architecture of human cranial dura mater. J Anat 1998. https://doi.org/10.1017/S0021878297003063.

[24] Dujovny M, Agner C. The use of high power drills for laminectomy in spinal stenosis: Technical report. Neurol Res 1997;19:219–21. https://doi.org/10.1080/01616412.1997.11740799.

[25] Hosono N, Miwa T, Mukai Y, Takenaka S, Makino T. Potential risk of thermal

damage to cervical nerve roots by a high-speed drill 2009;91:1541–4. https://doi.org/10.1302/0301-620X.91B11.22196.

[26] Voormolen EHJ, Diederen S, van Stralen M, Woerdeman PA, Noordmans HJ, Viergever MA, et al. Benchmarking Distance Control and Virtual Drilling for Lateral Skull Base Surgery. World Neurosurg 2018;109:e217–28. https://doi.org/10.1016/j.wneu.2017.09.142.

[27] Tahmasbi V, Ghoreishi M, Zolfaghari M. Sensitivity analysis of temperature and force in robotic bone drilling process using Sobol statistical method. Biotechnol Biotechnol Equip 2018;32:130–41. https://doi.org/10.1080/13102818.2017.1403863.

[28] Zhang Y, Xu L, Wang C, Chen Z, Han S, Chen B, et al. Mechanical and thermal damage in cortical bone drilling in vivo. Proc Inst Mech Eng Part H J Eng Med 2019;233:621–35. https://doi.org/10.1177/0954411919840194.

[29] Danda A, Kao YT, Kuttolamadom MA, Tai BL. Characterization of forces in high-speed bone cutting and grinding for haptics rendering. ASME 2016 11th Int Manuf Sci Eng Conf MSEC 2016 2016;2:1–8. https://doi.org/10.1115/MSEC2016-8794.

[30] Siljander BR, Wang AC, Zhang L, Shih AJ, Sullivan SE, Tai BL. Cool mist irrigation improves heat dissipation during surgical bone drilling. J Neurol Surgery, Part B Skull Base 2014;75:243–6. https://doi.org/10.1055/s-0034-1368098.

[31] Shih AJ, Tai BL, Zhang L, Sullivan S, Malkin S. Prediction of bone grinding temperature in skull base neurosurgery. CIRP Ann - Manuf Technol 2012;61:307–10. https://doi.org/10.1016/j.cirp.2012.03.078.

[32] Shaw M Le, Kelley B, Camarata P, Sokol JA. Collateral Damage : Heat Transfer as a Possible Mechanism of Optic Nerve Injury During Neurosurgical Intervention. Ophthalmic Plast Reconstr Surg 2012;28:328–30. https://doi.org/10.1097/IOP.0b013e31825ca5b2.

[33] Augustin G, Davila S, Udiljak T, Vedrina DS, Bagatin D. Determination of spatial distribution of increase in bone temperature during drilling by infrared thermography: Preliminary report. Arch Orthop Trauma Surg 2009;129:703–9. https://doi.org/10.1007/s00402-008-0630-x.

[34] Gupta V, Pandey PM, Gupta RK, Mridha AR. Rotary ultrasonic drilling on bone: A novel technique to put an end to thermal injury to bone. Proc Inst Mech Eng Part H J Eng Med 2017;231:189–96. https://doi.org/10.1177/0954411916688500.

[35] Wang G, Zhang L, Wang X, Tai BL. An inverse method to reconstruct the heat flux produced by bone grinding tools. Int J Therm Sci 2016;101:85–92. https://doi.org/10.1016/j.ijthermalsci.2015.10.021.

[36] Sasaki M, Morris S, Goto T, Iwatsuki K, Yoshimine T. Spray-Irrigation System Attached to High-Speed Drills for Simultaneous Prevention of Local Heating and Preservation of a Clear Operative Field in Spinal Surgery. Neurol Med Chir (Tokyo) 2010;50:900–4. https://doi.org/10.2176/nmc.50.900.

[37] Babbar A, Jain V, Gupta D. Thermogenesis mitigation using ultrasonic actuation during bone grinding: a hybrid approach using CEM43°C and Arrhenius model. J Brazilian Soc Mech Sci Eng 2019;41:401. https://doi.org/10.1007/s40430-019-1913-6.

[38] Singh J, Satsangi PS, Walia RS, Singh VP. Micro-Hardness and Machined Surface

Damage Study for Continuous and Discontinuous Ultrasonic Vibration Assisted Electrical Discharge Machining. Mater Manuf Process 2011. https://doi.org/10.1080/10426914.2011.585502.

[39] Venkatesh G, Sharma AK, Kumar P. On ultrasonic assisted abrasive flow finishing of bevel gears. Int J Mach Tools Manuf 2015. https://doi.org/10.1016/j.ijmachtools.2014.10.014.

[40] Churi NJ, Pei ZJ, Shorter DC, Treadwell C. Rotary ultrasonic machining of silicon carbide: designed experiments. Int J Manuf Technol Manag 2007;12:284. https://doi.org/10.1504/IJMTM.2007.014154.

[41] Kumar S, Grover S, Walia RS. Analyzing and modeling the performance index of ultrasonic vibration assisted EDM using graph theory and matrix approach. Int J Interact Des Manuf 2018. https://doi.org/10.1007/s12008-016-0355-y.

[42] Tartibu Kwanda L. Multi-objective optimization of a rectangular micro-channel heat sink using the augmented ε-constraint method. Eng Optim 2020. https://doi.org/10.1080/0305215X.2019.1574346.

[43] Tartibu LK. Numerical analysis on thermal performance of a trapezoidal micro-channel heat sink using an improved version of the augmented ε-constraint method. Int J Math Model Numer Optim 2020. https://doi.org/10.1504/ijmmno.2020.10026038.

[44] Singh RP, Singhal S. Rotary Ultrasonic Machining: A Review. Mater Manuf Process 2016;31:1795–824. https://doi.org/10.1080/10426914.2016.1140188.

[45] Li Z, Yang D, Hao W, Wu S, Ye Y, Chen Z, et al. Ultrasonic vibration-assisted micro-hole forming on skull. Proc Inst Mech Eng Part B J Eng Manuf 2015;231:2447–57. https://doi.org/10.1177/0954405415611363.

[46] Cong WL, Pei ZJ, Treadwell C. Preliminary study on rotary ultrasonic machining of CFRP/Ti stacks. Ultrasonics 2014;54:1594–602. https://doi.org/10.1016/j.ultras.2014.03.012.

[47] Sablotzki A, Ebel H, Mühling J, Dehne MG, Nopens H, Giesselmann H, et al. Dysregulation of immune response following neurosurgical operations. Acta Anaesthesiol Scand 2000;44:82–7. https://doi.org/10.1016/j.icarus.2016.11.017.

[48] Halpern CH, Grady MS. Neurosurgery. Schwartz's Princ. Surgery, 10e, 2014.

[49] Tai BL, Zhang L, Wang A, Sullivan S, Shih AJ. Neurosurgical Bone Grinding Temperature Monitoring. Procedia CIRP 2013;5:226–30. https://doi.org/10.1016/j.procir.2013.01.045.

[50] De Vrind HH, Wondergem J, Haveman J. Hyperthermia-induced damage to rat sciatic nerve assessed in vivo with functional methods and with electrophysiology. J Neurosci Methods 1992;45:165–74. https://doi.org/10.1016/0165-0270(92)90073-M.

[51] Xu D, Pollock M. Experimental nerve thermal injury. Brain 1994;117:375–84. https://doi.org/10.1093/brain/117.2.375.

[52] Tamai K, Suzuki A, Takahashi S, Akhgar J, Rahmani MS, Hayashi K, et al. The incidence of nerve root injury by highspeed drill can be reduced by chilled saline irrigation in a rabbit model. Bone Jt J 2017;99B:554–60. https://doi.org/10.1302/0301-620X.99B4.BJJ-2016-0841.R1.

[53] McDannold N, Vykhodtseva N, Jolesz FA, Hynynen K. MRI Investigation of the Threshold for Thermally Induced Blood-Brain Barrier Disruption and Brain Tissue Damage in the Rabbit Brain. Magn Reson Med 2004;51:913–23. https://doi.org/10.1002/mrm.20060.

[54] Robinson L. Traumatic Injury to Peripheral Nerves. Nerves Nerve Inj., vol. 2, Elsevier; 2015, p. 611–28. https://doi.org/10.1016/B978-0-12-802653-3.00088-9.

[55] van Rhoon GC, Samaras T, Yarmolenko PS, Dewhirst MW, Neufeld E, Kuster N. CEM43°C thermal dose thresholds: a potential guide for magnetic resonance radiofrequency exposure levels? Eur Radiol 2013;23:2215–27. https://doi.org/10.1007/s00330-013-2825-y.

[56] Monafo WW, Eliasson SG. Sciatic nerve function following hindlimb thermal injury. J Surg Res 1987;43:344–50. https://doi.org/10.1016/0022-4804(87)90091-6.

[57] Augustin G, Davila S, Mihoci K, Udiljak T, Vedrina DS, Antabak A. Thermal osteonecrosis and bone drilling parameters revisited. Arch Orthop Trauma Surg 2008;128:71–7. https://doi.org/10.1007/s00402-007-0427-3.

[58] Aslan A, Vatansever HS, Aslan GG, Eskiizmir G, Giray G. Effect of thermal energy produced by drilling on the facial nerve: Histopathologic evaluation in guinea pigs. J Laryngol Otol 2005;119:600–5. https://doi.org/10.1258/0022215054516250.

[59] Gupta S, Sharma AK. Sintering of Biomaterials for Arthroplasty: A Comparative Study of Microwave and Conventional Sintering Techniques. Appl Mech Mater 2019. https://doi.org/10.4028/www.scientific.net/amm.895.83.

[60] Xi X, Yu T, Ding W, Xu J. Grinding of Ti2AlNb intermetallics using silicon carbide and alumina abrasive wheels: Tool surface topology effect on grinding force and ground surface quality. Precis Eng 2018;53:134–45. https://doi.org/10.1016/j.precisioneng.2018.03.007.

[61] Santolaria J, Guillomía D, Cajal C, Albajez JA, Aguilar JJ. Modelling and calibration technique of laser triangulation sensors for integration in robot arms and articulated arm coordinate measuring machines. Sensors 2009;9:7374–96. https://doi.org/10.3390/s90907374.

[62] Malkin S, Cook NH. The Wear of Grinding Wheels: Part 1—Attritious Wear. J Eng Ind 1971;93:1120. https://doi.org/10.1115/1.3428051.

[63] Nayak A, Jain PK, Kankar P, Jain N. Computer-aided design–based guided endodontic: A novel approach for root canal access cavity preparation. Proc Inst Mech Eng Part H J Eng Med 2018;232:787–95. https://doi.org/10.1177/0954411918788104.

[64] Nayak A, Kankar PK, Jain PK, Jain N. Force and vibration generated in apical direction by three endodontic files of different kinematics during simulated canal preparation: An in vitro analytical study. Proc Inst Mech Eng Part H J Eng Med 2019. https://doi.org/10.1177/0954411919854574.

[65] Alauddin M, Mazid MA, El Baradi MA, Hashmi MSJ. Cutting forces in the end milling of Inconel 718. J Mater Process Technol 1998. https://doi.org/10.1016/s0924-0136(97)00412-3.

[66] Hwang J, Kompella S, Chandrasekar S, Farris TN. Measurement of Temperature Field in Surface Grinding Using Infra-Red (IR) Imaging System. J Tribol 2002;125:377–83.

https://doi.org/10.1115/1.1537748.

[67] Augustin G, Zigman T, Davila S, Udilljak T, Staroveski T, Brezak D, et al. Cortical bone drilling and thermal osteonecrosis. Clin Biomech 2012;27:313–25. https://doi.org/10.1016/j.clinbiomech.2011.10.010.

[68] Tai BL, Palmisano AC, Belmont B, Irwin TA, Holmes J, Shih AJ. Numerical evaluation of sequential bone drilling strategies based on thermal damage. Med Eng Phys 2015;37:855–61. https://doi.org/10.1016/j.medengphy.2015.06.002.

[69] Feldmann A, Wandel J, Zysset P. Reducing temperature elevation of robotic bone drilling. Med Eng Phys 2016;38:1495–504. https://doi.org/10.1016/j.medengphy.2016.10.001.

[70] Chang IA. Considerations for Thermal Injury Analysis for RF Ablation Devices~!2009-09-09~!2009-12-19~!2010-02-04~! Open Biomed Eng J 2010;4:3–12. https://doi.org/10.2174/1874120701004020003.

[71] Stauffer PR. Physics of Thermal Therapy: Fundamentals and Clinical Applications. Med Phys 2013;40:067302. https://doi.org/10.1118/1.4804052.

[72] Yarmolenko PS, Moon EJ, Landon C, Manzoor A, Hochman DW, Viglianti BL, et al. Thresholds for thermal damage to normal tissues: An update. Int J Hyperth 2011;27:320–43. https://doi.org/10.3109/02656736.2010.534527.

[73] Dewey WC. Arrhenius relationships from the molecule and cell to the clinic. Int J Hyperth 2009;25:3–20. https://doi.org/10.1080/02656730902747919.

[74] Dewhirst MW, Viglianti BL, Lora-Michiels M, Hanson M, Hoopes PJ. Basic principles of thermal dosimetry and thermal thresholds for tissue damage from hyperthermia. Int J Hyperth 2003;19:267–94. https://doi.org/10.1080/0265673031000119006.

[75] Feldmann A, Gavaghan K, Stebinger M, Williamson T, Weber S, Zysset P. Real-Time Prediction of Temperature Elevation During Robotic Bone Drilling Using the Torque Signal. Ann Biomed Eng 2017;45:2088–97. https://doi.org/10.1007/s10439-017-1845-1.

[76] Feldmann A, Anso J, Bell B, Williamson T, Gavaghan K, Gerber N, et al. Temperature Prediction Model for Bone Drilling Based on Density Distribution and In Vivo Experiments for Minimally Invasive Robotic Cochlear Implantation. Ann Biomed Eng 2016;44:1576–86. https://doi.org/10.1007/s10439-015-1450-0.

[77] Dewhirst MW, Viglianti LB, Lora-Michiels M, Hoopes PJ, Hanson M. Thermal Dose Requirement for Tissue Effect. Proc SPIE Int Soc Opt Eng 2003;37:338–48. https://doi.org/10.1037/emo0000122.Do.

[78] Van Rhoon GC. Is CEM43 still a relevant thermal dose parameter for hyperthermia treatment monitoring? Int J Hyperth 2016;32:50–62. https://doi.org/10.3109/02656736.2015.1114153.

[79] Borrelli M., Thompson L., Cain C., Dewey W. Time-temperature analysis of cell killing of BHK cells heated at temperatures in the range of 43.5°C to 57.0°C. Int J Radiat Oncol 1990;19:389–99. https://doi.org/10.1016/0360-3016(90)90548-X.

[80] Shakouri E, Sadeghi MH, Karafi MR, Maerefat M, Farzin M. An in vitro study of

thermal necrosis in ultrasonic-assisted drilling of bone. Proc Inst Mech Eng Part H J Eng Med 2015;229:137–49. https://doi.org/10.1177/0954411915573064.

[81] Pearce JA. Relationship between Arrhenius models of thermal damage and the CEM 43 thermal dose. In: Ryan TP, editor. Energy-based Treat. Tissue Assess., vol. 7181, 2009, p. 718104. https://doi.org/10.1117/12.807999.

[82] Sapareto SA, Dewey WC. Thermal dose determination in cancer therapy. Int J Radiat Oncol 1984;10:787–800. https://doi.org/10.1016/0360-3016(84)90379-1.

[83] Moritz AR, Henriques FC. Studies of thermal injury: the relative importance of time and surface temperature in the causation of cutaneous burns. Am J Pathol 1947;23:695–720. https://doi.org/10.1097/DAD.0b013e31820d15f0.

[84] Martin NA, Falder S. A review of the evidence for threshold of burn injury. Burns 2017;43:1624–39. https://doi.org/10.1016/j.burns.2017.04.003.

[85] Jr. HF. Studies of thermal injury; the predictability and the significance of thermally induced rate processes leading to irreversible epidermal injury. Arch Pathol 1947;43:489–502.

[86] Sapareto SA, Hopwood LE, Dewey WC. Combined Effects of X Irradiation and Hyperthermia on CHO Cells for Various Temperatures and Orders of Application. Radiat Res 1978. https://doi.org/10.2307/3574816.

[87] Kumar R, Panda SS. Drilling of bone : A comprehensive review. J Clin Orthop Trauma 2013;4:15–30. https://doi.org/10.1016/j.jcot.2013.01.002.

[88] James TP, Chang G, Micucci S, Sagar A, Smith EL, Cassidy C. Effect of applied force and blade speed on histopathology of bone during resection by sagittal saw. Med Eng Phys 2014;36:364–70. https://doi.org/10.1016/j.medengphy.2013.12.002.

[89] Beaulé PE, Amstutz HC. Management of Ficat stage III and IV osteonecrosis of the hip. J Am Acad Orthop Surg 2004;12:96–105. https://doi.org/10.5435/00124635-200403000-00005.

[90] Freist W, Gauss DH. Lysyl-tRNA Synthetase. Biol Chem Hoppe Seyler 1995;376:451–72. https://doi.org/10.1515/bchm3.1995.376.8.451.

[91] Eriksson A, Albrektsson T, Grane B, McQueen D. Thermal injury to bone. A vital-microscopic description of heat effects. Int J Oral Surg 1982;11:115–21.

[92] Pandey RK, Panda SS. Optimization of multiple quality characteristics in bone drilling using grey relational analysis. J Orthop 2014;6122552037:1–7. https://doi.org/10.1016/j.jor.2014.06.003.

[93] Singh G, Jain V, Gupta D. Comparative study for surface topography of bone drilling using conventional drilling and loose abrasive machining. Proc Inst Mech Eng Part H J Eng Med 2015;229:225–31. https://doi.org/10.1177/0954411915576945.

[94] Bonfield W, Li CH. The temperature dependence of the deformation of bone. J Biomech 1968;1:323–9. https://doi.org/10.1016/0021-9290(68)90026-2.

[95] Lundskog J. Heat and bone tissue. An experimental investigation of the thermal properties of bone and threshold levels for thermal injury. Scand J Plast Reconstr Surg 1972.

[96] Eriksson AR, Albrektsson T, Albrektsson B. Heat caused by drilling cortical bone: Temperature measured in vivo in patients and animals. Acta Orthop 1984;55:629–31. https://doi.org/10.3109/17453678408992410.

[97] Berman AT, Reid JS, Yanicko DR, Sih GC, Zimmerman MR. Thermally induced bone necrosis in rabbits. Relation to implant failure in humans. Clin Orthop Relat Res 1984:284–92.

[98] Uchiyama S, Yashiro K, Takahashi H, Homma T. An Experimental Study of Spinal Cord Evoked Potentials and Histologic Changes following Spinal Cord Heating. Spine (Phila Pa 1976) 1989;14:1215–9. https://doi.org/10.1097/00007632-198911000-00014.

[99] Hoogeveen JF, Troost D, Wondergem J, van der Kracht AHW, Haveman J. Hyperthermic injury versus crush injury in the rat sciatic nerve: A comparative functional, histopathological and morphometrical study. J Neurol Sci 1992;108:55–64. https://doi.org/10.1016/0022-510X(92)90188-Q.

[100] Konno S, Olmarker K, Byröd G, Nordborg C, Strömqvist B, Rydevik B. Acute thermal nerve root injury. Eur Spine J 1994;3:299–302. https://doi.org/10.1007/BF02200140.

[101] Olson S, Clinton JM, Working Z, Lynch JR, Warme WJ, Womack W, et al. Thermal effects of glenoid reaming during shoulder arthroplasty in vivo. J Bone Jt Surg - Ser A 2011;93:11–9. https://doi.org/10.2106/JBJS.I.01227.

[102] Kießling TR, Stange R, Käs JA, Fritsch AW. Thermorheology of living cells—impact of temperature variations on cell mechanics. New J Phys 2013;15:045026. https://doi.org/10.1088/1367-2630/15/4/045026.

[103] Gupta V, Pandey PM, Silberschmidt V V. Rotary ultrasonic bone drilling: Improved pullout strength and reduced damage. Med Eng Phys 2017;41:1–8. https://doi.org/10.1016/j.medengphy.2016.11.004.

[104] Gupta V, Pandey PM. In-situ tool wear monitoring and its effects on the performance of porcine cortical bone drilling: a comparative in-vitro investigation. Mech Adv Mater Mod Process 2017;3:2. https://doi.org/10.1186/s40759-017-0019-z.

[105] Gupta V, Pandey PM, Mridha AR, Gupta RK. Effect of Various Parameters on the Temperature Distribution in Conventional and Diamond Coated Hollow Tool Bone Drilling: A Comparative Study. Procedia Eng 2017;184:90–8. https://doi.org/10.1016/j.proeng.2017.04.074.

[106] Gupta V, Pandey PM. An in-vitro study of cutting force and torque during rotary ultrasonic bone drilling. Proc Inst Mech Eng Part B J Eng Manuf 2018;232:1549–60. https://doi.org/10.1177/0954405416673115.

[107] Pandey RK, Panda SS. Optimization of bone drilling parameters using grey-based fuzzy algorithm. Measurement 2014;47:386–92. https://doi.org/10.1016/j.measurement.2013.09.007.

[108] Singh G, Jindal R, Jain V, Gupta D. Effect of tool and drilling parameters on surface topography of bone drilled holes: An in vitro study. 2016 Int. Conf. Students Appl. Eng. ICSAE 2016, 2017, p. 196–200. https://doi.org/10.1109/ICSAE.2016.7810187.

[109] Draenert FG, Mathys R, Ehrenfeld M, Draenert Y, Draenert K. Histological examination of drill sites in bovine rib bone after grinding in vitro with eight different devices. Br J Oral Maxillofac Surg 2007;45:548–52.

https://doi.org/10.1016/j.bjoms.2006.12.007.

[110] Pandey RK, Panda SS. A feasibility investigation for modeling and optimization of temperature in bone drilling using fuzzy logic and Taguchi optimization methodology 2014;228:1135–45. https://doi.org/10.1177/0954411914559738.

[111] Singh G, Jain V, Gupta D. Multi-objective performance investigation of orthopaedic bone drilling using Taguchi membership function. Proc Inst Mech Eng Part H J Eng Med 2017;231:1133–9. https://doi.org/10.1177/0954411917735129.

[112] Lee JE, Ozdoganlar OB, Rabin Y. An experimental investigation on thermal exposure during bone drilling. Med Eng Phys 2012;34:1510–20. https://doi.org/10.1016/j.medengphy.2012.03.002.

[113] Augustin G, Zigman T, Davila S, Udilljak T, Staroveski T, Brezak D, et al. Cortical bone drilling and thermal osteonecrosis. Clin Biomech 2012;27:313–25. https://doi.org/10.1016/j.clinbiomech.2011.10.010.

[114] Pandey RK, Panda SS. Multi-performance optimization of bone drilling using Taguchi method based on membership function. Measurement 2015;59:9–13. https://doi.org/10.1016/j.measurement.2014.09.038.

[115] Schaller BJ, Gruber R, Merten HA, Kruschat T, Schliephake H, Buchfelder M, et al. Piezoelectric Bone Surgery: A Revolutionary Technique for Minimally Invasive Surgery in Cranial Base and Spinal Surgery? Technical Note. Oper Neurosurg 2005;57:E410. https://doi.org/10.1227/01.NEU.0000176700.77461.C9.

[116] Yamamoto S, Kim P, Abe Y, Itoki K, Shingo T, Kurokawa R, et al. Bone temperature elevation by drilling friction and neurological outcome in the cervical spino-laminoplasty. Acta Neurochir (Wien) 2013;155:2321–5. https://doi.org/10.1007/s00701-013-1867-x.

[117] Birch J, BrâRnemark PI, Nilsson K, Lundskog J. Vascular Reactions in an Experimental Burn Studied with Infrared Thermography and Microangiography. Scand J Plast Reconstr Surg 1968;2:97–103. https://doi.org/10.3109/02844316809010490.

[118] Eriksson AR, Albrektsson T. Temperature threshold levels for heat-induced bone tissue injury: A vital-microscopic study in the rabbit. J Prosthet Dent 1983;50:101–7. https://doi.org/10.1016/0022-3913(83)90174-9.

[119] Clarkin C, Olsen BR. On bone-forming cells and blood vessels in bone development. Cell Metab 2010;12:314–6. https://doi.org/10.1016/j.cmet.2010.09.009.

[120] Matthes M, Pillich DT, El Refaee E, Schroeder HWS, Müller J-U. Heat Generation During Bony Decompression of Lumbar Spinal Stenosis Using a High-Speed Diamond Drill with or without Automated Irrigation and an Ultrasonic Bone-Cutting Knife: A Single-Blinded Prospective Randomized Controlled Study. World Neurosurg 2018;111:e72–81. https://doi.org/10.1016/j.wneu.2017.11.172.

[121] Kapłonek W, Nadolny K. Assessment of the grinding wheel active surface condition using SEM and image analysis techniques. J Brazilian Soc Mech Sci Eng 2013;35:207–15. https://doi.org/10.1007/s40430-013-0018-x.

[122] Yang YX, Wang CY, Qin Z, Xu LL, Song YX, Chen HY. Drilling Force and Temperature of Bone by Surgical Drill. Adv Mater Res 2010;126:779–84.

https://doi.org/10.4028/www.scientific.net/AMR.126-128.779.

[123] O'Daly BJ, Morris E, Gavin GP, O'Byrne JM, McGuinness GB. High-power low-frequency ultrasound: A review of tissue dissection and ablation in medicine and surgery. J Mater Process Technol 2008;200:38–58. https://doi.org/10.1016/j.jmatprotec.2007.11.041.

[124] Akhbar MFA, Yusoff AR. Optimization of drilling parameters for thermal bone necrosis prevention. Technol Heal Care 2018;26:621–35. https://doi.org/10.3233/THC-181221.

[125] Cseke A, Heinemann R. The effects of cutting parameters on cutting forces and heat generation when drilling animal bone and biomechanical test materials. Med Eng Phys 2018;51:24–30. https://doi.org/10.1016/j.medengphy.2017.10.009.

[126] Sharma A, Jain V, Gupta D. Multi-shaped tool wear study during rotary ultrasonic drilling and conventional drilling for amorphous solid. Proc Inst Mech Eng Part E J Process Mech Eng 2019;233:551–60. https://doi.org/10.1177/0954408918776724.

[127] Tai BL, Stephenson DA, Shih AJ. An inverse heat transfer method for determining workpiece temperature in minimum quantity lubrication deep hole drilling. J Manuf Sci Eng Trans ASME 2012;134. https://doi.org/10.1115/1.4005794.

[128] Ruder JA, Turvey B, Hsu JR, Scannell BP. Effectiveness of a Low-Cost Drilling Module in Orthopaedic Surgical Simulation. J Surg Educ 2017;74:471–6. https://doi.org/10.1016/j.jsurg.2016.10.010.

[129] Yao C, Wang T, Xiao W, Huang X, Ren J. Experimental study on grinding force and grinding temperature of Aermet 100 steel in surface grinding. J Mater Process Technol 2014;214:2191–9. https://doi.org/10.1016/j.jmatprotec.2014.04.013.

[130] Al-abdullah KIA, Abdi H, Peng C, Yassin WA. Force and temperature modelling of bone milling using arti fi cial neural networks. Measurement 2018;116:25–37. https://doi.org/10.1016/j.measurement.2017.10.051.

[131] Tang J, Du J, Chen Y. Modeling and experimental study of grinding forces in surface grinding. J Mater Process Technol 2009;209:2847–54. https://doi.org/10.1016/j.jmatprotec.2008.06.036.

[132] Bagci E, Ozcelik B. Effects of different cooling conditions on twist drill temperature. Int J Adv Manuf Technol 2007;34:867–77. https://doi.org/10.1007/s00170-006-0668-2.

[133] Bertollo N, Robert W. Drilling of Bone: Practicality, Limitations and Complications Associated with Surgical Drill-Bits. Biomech. Appl., InTech; 2011. https://doi.org/10.5772/20931.

[134] Harder S, Egert C, Freitag-Wolf S, Mehl C, Kern M. Intraosseous Temperature Changes During Implant Site Preparation: In Vitro Comparison of Thermocouples and Infrared Thermography. Int J Oral Maxillofac Implants 2018;33:72–8. https://doi.org/10.11607/jomi.6222.

[135] Giansanti D. Improving spatial resolution in skin-contact thermography: Comparison between a spline based and linear interpolation. Med Eng Phys 2008;30:733–8. https://doi.org/10.1016/j.medengphy.2007.08.002.

[136] Cheng VS, Bai J, Chen Y. A high-resolution three-dimensional far-infrared thermal and true-color imaging system for medical applications. Med Eng Phys 2009;31:1173–81. https://doi.org/10.1016/j.medengphy.2009.07.016.

[137] Xu L, Wang C, Jiang M, He H, Song Y, Chen H, et al. Drilling force and temperature of bone under dry and physiological drilling conditions. Chinese J Mech Eng 2014;27:1240–8. https://doi.org/10.3901/CJME.2014.0912.151.

[138] Zhang L, Tai BL, Wang AC, Shih AJ. Mist cooling in neurosurgical bone grinding. CIRP Ann 2013;62:367–70. https://doi.org/10.1016/j.cirp.2013.03.125.

[139] Shakouri E, Mirfallah P. Infrared thermography of high-speed grinding of bone in skull base neurosurgery. Proc Inst Mech Eng Part H J Eng Med 2019;233:648–56. https://doi.org/10.1177/0954411919845730.

[140] Domitran Z, Brezak D, Staroveski T, Klaic M, Bruketa T. Experimental and finite element analysis of surgical drill bits with and without irrigation channel – A case study approach. Med Eng Phys 2018;62:29–35. https://doi.org/10.1016/j.medengphy.2018.10.004.

[141] Dambatta YS, Sarhan AAD, Sayuti M, Hamdi M. Ultrasonic assisted grinding of advanced materials for biomedical and aerospace applications—a review. Int J Adv Manuf Technol 2017;92:3825–58. https://doi.org/10.1007/s00170-017-0316-z.

[142] Alam K, Hassan E, Bahadur I. Experimental measurements of temperatures in ultrasonically assisted drilling of cortical bone. Biotechnol Biotechnol Equip 2015;29:753–7. https://doi.org/10.1080/13102818.2015.1034176.

[143] Nakagawa T. Endoscopic skull base surgery. Otolaryngol - Head Neck Surg 2014;86:40–4. https://doi.org/10.3342/ceo.2008.1.2.53.

[144] Yang M, Li C, Zhang Y, Wang Y, Li B, Jia D, et al. Research on microscale skull grinding temperature field under different cooling conditions. Appl Therm Eng 2017;126:525–37. https://doi.org/10.1016/j.applthermaleng.2017.07.183.

[145] Kondo S, Okada Y, Iseki H, Hori T, Takakura K, Nagata H. Thermological Study of Drilling Bone Tissue with a High-speed Drill 2000:1162–8. https://doi.org/10.1097/00006123-200005000-00029.

[146] Enomoto T, Shigeta H, Sugihara T, Satake U. A new surgical grinding wheel for suppressing grinding heat generation in bone resection. CIRP Ann 2014;63:305–8. https://doi.org/10.1016/j.cirp.2014.03.026.

[147] Yang M, Li C, Zhang Y, Wang Y, Li B, Hou Y. Experimental research on microscale grinding temperature under different nanoparticle jet minimum quantity cooling. Mater Manuf Process 2017;32:589–97. https://doi.org/10.1080/10426914.2016.1176198.

[148] Mizutani T, Satake U, Enomoto T. Surgical diamond wheels for minimally invasive surgery in bone resection under small quantity of coolant supply. Precis Eng 2019;56:80–6. https://doi.org/10.1016/j.precisioneng.2018.09.015.

[149] Li ZC, Jiao Y, Deines TW, Pei ZJ, Treadwell C. Rotary ultrasonic machining of ceramic matrix composites: feasibility study and designed experiments. Int J Mach Tools Manuf 2005;45:1402–11. https://doi.org/10.1016/j.ijmachtools.2005.01.034.

[150] Churi NJ, Pei ZJ, Treadwell C. Rotary ultrasonic machining of titanium alloy: effects

of machining variables. Mach Sci Technol 2006;10:301–21. https://doi.org/10.1080/10910340600902124.

[151] Feng Q, Cong WL, Pei ZJ, Ren CZ. Rotary ultrasonic machining of carbon fiber-reinforced polymer: Feasibilty study. Mach Sci Technol 2012;16:380–98. https://doi.org/10.1080/10910344.2012.698962.

[152] Chai J. Rotary Ultrasonic-assisted Grinding of Ceramic Material 2012;219:1705–8. https://doi.org/10.4028/www.scientific.net/AMM.217-219.1705.

[153] Geng D, Zhang D, Xu Y, He F, Liu F. Comparison of drill wear mechanism between rotary ultrasonic elliptical machining and conventional drilling of CFRP. J Reinf Plast Compos 2014;33:797–809. https://doi.org/10.1177/0731684413518619.

[154] Ning FD, Cong WL, Pei ZJ, Treadwell C. Rotary ultrasonic machining of CFRP: A comparison with grinding. Ultrasonics 2016;66:125–32. https://doi.org/10.1016/j.ultras.2015.11.002.

[155] Hu Y, Wang H. Surface Grinding of Optical BK7/K9 Glass Using Rotary Ultrasonic Machining: An Experimental Study. ASME 2017 12th Int Manuf Sci Eng Conf Collocated with JSME/ASME 2017 6th Int Conf Mater Process 2017;1:1–7.

[156] Alam K, Khan M, Silberschmidt V V. Analysis of forces in conventional and ultrasonically assisted plane cutting of cortical bone. Proc Inst Mech Eng Part H J Eng Med 2013;227:636–42. https://doi.org/10.1177/0954411913485042.

[157] Karaca F, Aksakal B, Kom M. Influence of orthopaedic drilling parameters on temperature and histopathology of bovine tibia: An in vitro study. Med Eng Phys 2011;33:1221–7. https://doi.org/10.1016/j.medengphy.2011.05.013.

[158] Alam K, Mitrofanov AV, Silberschmidt VV. Experimental investigations of forces and torque in conventional and ultrasonically-assisted drilling of cortical bone. Med Eng Phys 2011;33:234–9. https://doi.org/10.1016/j.medengphy.2010.10.003.

[159] Alam K, Silberschmidt V V. Analysis of temperature in conventional and ultrasonically-assisted drilling of cortical bone with infrared thermography. Technol Heal Care 2014;22:243–52. https://doi.org/10.3233/THC-140813.

[160] Alam K, Al-Ghaithi A, Piya S, Saleem A. In-vitro experimental study of histopathology of bone in vibrational drilling. Med Eng Phys 2019;67:78–87. https://doi.org/10.1016/j.medengphy.2019.03.013.

[161] Kanaya H, Enokida M, Uehara K, Ueki M, Nagashima H. Thermal damage of osteocytes during pig bone drilling: an in vivo comparative study of currently available and modified drills. Arch Orthop Trauma Surg 2019. https://doi.org/10.1007/s00402-019-03239-y.

[162] Davidson SR, James DF. Measurement of thermal conductivity of bovine cortical bone. Med Eng Phys 2000;22:741–7.

[163] F Karaca BA. Effects of various drilling parameters on bone during implantology : An in vitro experimental study. Acta Bioeng Biomech 2013;15. https://doi.org/10.5277/abb130404.

[164] Pandey RK, Panda SS. Evaluation of delamination in drilling of bone. Med Eng Phys 2015;37:657–64. https://doi.org/10.1016/j.medengphy.2015.04.008.

[165] G. Fernandes M, M. Fonseca E, N. Jorge R, C. Manzanares M, I. Dias M. Effect of drill speed on the strain distribution during drilling of bovine and human bones. J Mech Eng Biomech 2018;2:69–74. https://doi.org/10.24243/JMEB/2.5.170.

[166] Alam K, Ghodsi M, Al-Shabibi A, Silberschmidt V. Experimental Study on the Effect of Point Angle on Force and Temperature in Ultrasonically Assisted Bone Drilling. J Med Biol Eng 2018;38:236–43. https://doi.org/10.1007/s40846-017-0291-8.

[167] Kato N, Koshino T, Saito T, Takeuchi R. Estimation of Young's modulus in swine cortical bone using quantitative computed tomography. Bull Hosp Jt Dis 1998;57:183–6.

[168] Ying Z, Shu L, Sugita N. Experimental and Finite Element Analysis of Force and Temperature in Ultrasonic Vibration Assisted Bone Cutting. Ann Biomed Eng 2020;in press. https://doi.org/10.1007/s10439-020-02452-w.

[169] Lughmani WA, Bouazza-Marouf K, Ashcroft I. Drilling in cortical bone: a finite element model and experimental investigations. J Mech Behav Biomed Mater 2015;42:32–42. https://doi.org/10.1016/j.jmbbm.2014.10.017.

[170] Gupta V, Pandey PM. Experimental investigation and statistical modeling of temperature rise in rotary ultrasonic bone drilling. Med Eng Phys 2016;38:1330–8. https://doi.org/10.1016/j.medengphy.2016.08.012.

[171] Sharma A, Babbar A, Jain V, Gupta D. Enhancement of surface roughness for brittle material during rotary ultrasonic machining. MATEC Web Conf 2018;249:01006. https://doi.org/10.1051/matecconf/201824901006.

[172] Singh D, Babbar A, Jain V, Gupta D, Saxena S, Dwibedi V. Synthesis, characterization, and bioactivity investigation of biomimetic biodegradable PLA scaffold fabricated by fused filament fabrication process. J Brazilian Soc Mech Sci Eng 2019;41:121. https://doi.org/10.1007/s40430-019-1625-y.

[173] Babbar A, Singh P, Farwaha HS. Regression Model and Optimization of Magnetic Abrasive Finishing of Flat Brass Plate. Indian J Sci Technol 2017;10:1–7. https://doi.org/10.17485/ijst/2017/v10i31/113860.

[174] Babbar A, Jain V, Gupta D. Neurosurgical Bone Grinding. Biomanufacturing, Cham: Springer International Publishing; 2019, p. 137–55. https://doi.org/10.1007/978-3-030-13951-3_7.

[175] Babbar A, Sharma A, Jain V, Jain AK. Rotary ultrasonic milling of C/SiC composites fabricated using chemical vapor infiltration and needling technique. Mater Res Express 2019;6:085607. https://doi.org/10.1088/2053-1591/ab1bf7.

[176] Bogovič V, Svete A, Rupnik K, Bajsić I. Experimental analysis of the temperature rise during the simulation of an implant drilling process using experimental designs. Measurement 2015;63:221–31. https://doi.org/10.1016/j.measurement.2014.11.036.

[177] Alam K, Hassan E, Bahadur I. Experimental measurements of temperatures in ultrasonically assisted drilling of cortical bone. Biotechnol Biotechnol Equip 2015;29:753–7. https://doi.org/10.1080/13102818.2015.1034176.

[178] Hillery MT, Shuaib I. Temperature effects in the drilling of human and bovine bone. J Mater Process Technol 1999;92–93:302–8. https://doi.org/10.1016/S0924-0136(99)00155-7.

[179] Bachus KN, Rondina MT, Hutchinson DT. The effects of drilling force on cortical temperatures and their duration: An in vitro study. Med Eng Phys 2000;22:685–91. https://doi.org/10.1016/S1350-4533(01)00016-9.

[180] Danda A, Kuttolamadom MA, Tai BL. A mechanistic force model for simulating haptics of hand-held bone burring operations. Med Eng Phys 2017;49:7–13. https://doi.org/10.1016/j.medengphy.2017.06.041.

[181] Wang Y, Cao M, Zhao Y, Zhou G, Liu W, Li D. Experimental Investigations on Microcracks in Vibrational and Conventional Drilling of Cortical Bone. J Nanomater 2013;2013:1–5. https://doi.org/10.1155/2013/845205.

[182] Alam K, Ghafoor A, Silberschmidt V V. Analysis of Forces and Temperatures in Conventional and Ultrasonically-Assisted Cutting of Bone. Adv Mater Res 2011;223:247–54. https://doi.org/10.4028/www.scientific.net/AMR.223.247.

[183] Liu Q, Huang G, Fang C, Cui C, Xu X. Experimental investigations on grinding characteristics and removal mechanisms of 2D–C f /C-SiC composites based on reinforced fiber orientations. Ceram Int 2017;43:15266–74. https://doi.org/10.1016/j.ceramint.2017.08.064.

[184] Lee JE, Chavez CL, Park J. Parameters affecting mechanical and thermal responses in bone drilling: A review. J Biomech 2018;71:4–21. https://doi.org/10.1016/j.jbiomech.2018.02.025.

[185] Wang D, Zhang Y, Wang Y, Lee YS, Lu P, Wang Y. Cutting on triangle mesh: Local model-based haptic display for dental preparation surgery simulation. IEEE Trans Vis Comput Graph 2005. https://doi.org/10.1109/TVCG.2005.97.

[186] Wang Q, Chen H, Wu W, Qin J, Heng PA. Impulse-based rendering methods for haptic simulation of bone-burring. IEEE Trans Haptics 2012. https://doi.org/10.1109/TOH.2011.69.

[187] Lin Y, Wang X, Wu F, Chen X, Wang C, Shen G. Development and validation of a surgical training simulator with haptic feedback for learning bone-sawing skill. J Biomed Inform 2014. https://doi.org/10.1016/j.jbi.2013.12.010.

[188] Morris D, Sewell C, Barbagli F, Salisbury K, Blevins NH, Girod S. Visuohaptic simulation of bone surgery for training and evaluation. IEEE Comput Graph Appl 2006. https://doi.org/10.1109/MCG.2006.140.

[189] Moghaddam M, Nahvi A, Arbabtafti M, Mahvash M. A physically realistic voxel-based method for Haptic simulation of bone machining. Lect. Notes Comput. Sci. (including Subser. Lect. Notes Artif. Intell. Lect. Notes Bioinformatics), 2008. https://doi.org/10.1007/978-3-540-69057-3_82.

[190] Arbabtafti M, Moghaddam M, Nahvi A, Mahvash M, Richardson B, Shirinzadeh B. Physics-based haptic simulation of bone machining. IEEE Trans Haptics 2011. https://doi.org/10.1109/TOH.2010.5.

[191] Arbabtafti M, Moghaddam M, Nahvi A, Mahvash M, Rahimi A. Haptic and visual rendering of virtual bone surgery: A physically realistic voxel-based approach. HAVE 2008 - IEEE Int. Work. Haptic Audio Vis. Environ. Games Proc., 2008. https://doi.org/10.1109/HAVE.2008.4685294.

[192] Chan S, Li P, Locketz G, Salisbury K, Blevins NH. High-fidelity haptic and visual

rendering for patient-specific simulation of temporal bone surgery. Comput Assist Surg 2016. https://doi.org/10.1080/24699322.2016.1189966.

[193] Davidson SRH, James DF. Drilling in bone: Modeling heat generation and temperature distribution. J Biomech Eng 2003;125:305–14. https://doi.org/10.1115/1.1535190.

[194] Alam K. 3D finite-element modelling of drilling cortical bone: Temperature analysis. J Med Biol Eng 2013;34:618–23. https://doi.org/10.5405/jmbe.1585.

[195] Alam K, Mitrofanov AV, Silberschmidt VV. Thermal analysis of orthogonal cutting of cortical bone using finite element simulations. Int J Exp Comput Biomech 2010;1:236. https://doi.org/10.1504/IJECB.2010.035259.

[196] Alam K, Mitrofanov A V., Bäker M, Silberschmidt V V. Temperature Calculations in Orthogonal Cutting of Cortical Bone Using Finite Element Analysis. IFMBE Proc., vol. 24, 2009, p. 151–2. https://doi.org/10.1007/978-3-642-01697-4_55.

[197] Alam K, Mitrofanov AV, Silberschmidt VV. Finite element analysis of forces of plane cutting of cortical bone. Comput Mater Sci 2009;46:738–43. https://doi.org/10.1016/j.commatsci.2009.04.035.

[198] Santiuste C, Rodríguez-Millán M, Giner E, Miguélez H. The influence of anisotropy in numerical modeling of orthogonal cutting of cortical bone. Compos Struct 2014;116:423–31. https://doi.org/10.1016/j.compstruct.2014.05.031.

[199] Huiskes R. Some Fundamental Aspects of Human Joint Replacement: Analyses of Stresses and Heat Conduction in Bone-Prosthesis Structures. Acta Orthop Scand 1980;51:3–208. https://doi.org/10.3109/ort.1980.51.suppl-185.01.

[200] Feldmann A, Wandel J, Zysset P. Reducing temperature elevation of robotic bone drilling. Med Eng Phys 2016;38:1495–504. https://doi.org/10.1016/j.medengphy.2016.10.001.

[201] Tahmasbi V, Ghoreishi M, Zolfaghari M. Sensitivity analysis of temperature and force in robotic bone drilling process using Sobol statistical method. Biotechnol Biotechnol Equip 2018;32:130–41. https://doi.org/10.1080/13102818.2017.1403863.

VISIBLE OUTPUT

JOURNALS:

1. **Babbar A**, Jain V, Gupta D. Preliminary investigations of rotary ultrasonic neurosurgical bone grinding using Grey-Taguchi optimization methodology. Grey Systems: Theory and Application. 2020 Jun 23. *Status: **Published Online**, Publisher: Emerald, (**Impact Factor: 2.268**, Category: SCI).*
2. **Babbar A**, Jain V, Gupta D. In vivo evaluation of machining forces, torque, and bone quality during skull bone grinding. Proceedings of the Institution of Mechanical Engineers, Part H: Journal of Engineering in Medicine. 2020 Mar 17:0954411920911499. *Status: **Published Online**, Publisher: Sage Part H (**Impact Factor: 1.282**, Category: SCI)*.
3. **Babbar A**, Jain V, Gupta D. Thermogenesis mitigation using ultrasonic actuation during bone grinding: a hybrid approach using CEM43° C and Arrhenius model. Journal of the Brazilian Society of Mechanical Sciences and Engineering. 2019 Oct 1;41(10):401. *Status: **Published Online**, Publisher: Springer (**Impact Factor: 1.755**, Category: SCI).*
4. **Babbar A**, Jain V, Gupta D, Agrawal D. In-Vivo Histological Evaluation of Thermal Damage to Osteocytes: A Comparative Study of Conventional and Ultrasonic-Assisted Skull Bone Grinding. Medical Engineering & Physics. *Status: **Provisionally Accepted**, Publisher: Elsevier (**Impact Factor: 1.737**, Category: SCI).*
5. **Babbar A**, Jain V, Gupta D, Agrawal D. Finite Element Simulation and Integration of CEM43℃ into Arrhenius Model for Ultrasonic-Assisted Skull Bone Grinding: A

Thermal Dose Model. *Status:* Medical Engineering & Physics. *Status:* ***Provisionally Accepted****, Publisher: Elsevier (****Impact Factor: 1.737****, Category: SCI).*

6. **Babbar A**, Jain V, Gupta D. Thermo-mechanical aspects and temperature measurement techniques of bone grinding. Materials Today: Proceedings. 2020 Feb 21. *Status:* ***Published Online****, Publisher: Elsevier, Category: Scopus*

BOOK CHAPTERS:

1. **Babbar A**., Jain V., Gupta D. (2019) Neurosurgical Bone Grinding. In: Prakash C. et al. (eds) Biomanufacturing. Springer, Cham. *Status:* ***Published Online****, Publisher: Springer, Category:* ***Scopus***
2. **Babbar A**, Jain V, Gupta D, Sharma A. (2020) Effect of process parameters on cutting forces and osteonecrosis for orthopaedic bone drilling applications. *Status:* ***Published Online****, Publisher: Springer, Category:* ***Scopus***
3. **Babbar A**., Jain V., Gupta D. (2020) Potential Application of CEM43℃ and Arrhenius model in neurosurgical bone grinding. *Status:* ***Published Online****, Publisher: Springer, Category:* ***Scopus***

INTERNATIONAL CONFERENCE:

1. Symposium on Synthesis, Characterization & Processing of Inorganic, Bio and Nano Materials. 2020. Chandigarh, India

APPENDIX I

HYBRID THERMAL DOSE MODEL SAMPLE CALCULATIONS

The following calculations used for finding out the value of tissue damage function (Ω).

For Experiment number 19

Rotational speed = 55000 rpm

Feed rate = 60 mm/min

Ultrasonic frequency = 40 kHz

Temperature = 50.8℃

Machining time = 20 seconds = 0.333 minutes

Now,

Cumulative equivalent minutes has been calculated using the following equation

$$CEM_{43} = \int_0^{\tau} R_{CEM}^{T_{break}-T} d\tau \quad \text{.....eq. (i)}$$

T_{break} = 43℃

Therefore,

$$CEM_{43} = \left(0.5^{(43-50.8)}\right) \times 0.333$$

CEM_{43} = 74.2869

Till now we have converted the combined effect of temperature and machining time into a single equivalent number.

Now the value of CEM_{43} is further used to predict the thermal tissue injury.

Thermal tissue injury is calculated using the following equation.

$$\Omega(\tau) = A e^{\left(-\frac{E_a}{R.T(\tau)}\right)} \cdot \mathrm{CEM}_{43} \quad \text{.....eq. (ii)}$$

$A = 3.1\times10^{98}\ s^{-1} = 186\times10^{98}\ min^{-1}$

$E_a = 6.27\times10^{5}$ J/mol

R = 8.314 J/mol/k

T = 43+273.15 316.15 K

Now

$$e^{\left(-\frac{E_a}{R.T(\tau)}\right)} = e^{\frac{-6.27\times10^{5}}{8.314\times316.15}} = 2.531595\times10^{-104}$$

$$\Omega(\tau) = 186\times10^{98}\times2.531595\times10^{-104}\times\mathrm{CEM}_{43}$$

$$\Omega(\tau) = 0.00047\times\mathrm{CEM}_{43}$$

$$\Omega(\tau) = 0.00047\times74.2869$$

$$\Omega(\tau) = 0.034914881$$

In this way, the value of tissue damage function has been calculated for different sets of parametric combination.